



TEL AVIV UNIVERSITY

THE IBY AND ALADAR FLEISCHMAN FACULTY OF ENGINEERING

Characterization of Quasi-optical mm-wave FEL Resonator

By

O. Faingersh

THESIS SUBMITTED FOR THE DEGREE OF "MASTER OF SCIENCE"
SUBMITTED TO THE SENATE OF TEL-AVIV UNIVERSITY

October 2005

TEL AVIV UNIVERSITY

THE IBY AND ALADAR FLEISCHMAN FACULTY OF ENGINEERING

**Characterization of Quasi-optical
mm-wave FEL Resonator**

By

O. Faingersh

THESIS SUBMITTED FOR THE DEGREE OF “MASTER OF SCIENCE”

SUBMITTED TO THE SENATE OF TEL-AVIV UNIVERSITY

This research work was carried out under the supervision of

Prof. Abraham Gover

October 2005

Acknowledgments

I had the privilege to carry out this research on free electron lasers under the guidance of Prof. Avraham Gover - the winner of the 2005 FEL prize. Prof. Avraham Gover leads several unique research projects at two research institutes in Israel. His scientific vision and his theoretical investigations were the basis of my experimental investigation.

A number of people have contributed in many ways and it is a pleasure to acknowledge them. I sincerely appreciate the significant contribution of Dr. Ioseph Yakover who supervised and taught me at the beginning of my investigation work. I am extremely grateful to the FEL research groups at Tel Aviv University. I would like to thank Mr. Kleinman, our microwave electronics devices and high voltage systems expert, for his immediate knowledge, experience and technical help. Many thanks to Joshua Wolowelsky for his CAD support at workplace and discussions at our regular lunches. I thank Dr. Meir Arbel for his experience sharing and support.

I am very much indebted to all my colleagues at the College of Judea and Samaria mm-wave research center for help during the years while this work was been finished. My special thanks to Dr. Boris Kapilevich. His knowledge and experience helped me to understand better various microwave phenomena.

I would like to acknowledge the invaluable help of the reviewers. I greatly appreciate the help of Eng. Arie Eichenbaum who have provided continual encouragement and technical comments on the various chapters. Dr. Khona Garb carefully read and criticized the various chapters. Their many helpful comments made this manuscript a much better product. I also greatly appreciated help and support of Dr. Albert Chack, great teacher and physicist, whose knowledge, clarifications, textbooks and countenance was immeasurable.

Finally, I wish to express my heartfelt thanks and deepest appreciation to my wife Anya for her constant encouragement and support, and my parents for their patience during the writing of this book.

Abstract

In this work we investigated a novel resonator for the Israeli 100 GHz electrostatic accelerator Free Electron Laser (FEL). Generally, the laser resonator has to be of high quality (have low total internal losses) to ensure attainment of lasing threshold and thus laser operation. In order to allow e-beam entrance, exit and propagation on the axis of the resonator and still maintain a high Q factor in the W-band operation range (around 100 GHz), the resonator contains several unique wave-guiding sections. Characterization of such a resonator and estimation of its parameters (its round-trip reflectivity, losses) are important for achievement of laser operation.

Our FEL resonator is investigated in this work analytically, numerically and experimentally. Field distribution inside the Curved Parallel Plates (CPP) waveguide and the Talbot effect reflectors (components that enable transmission of electron beam through entrance and exit holes without degrading the Q factor) are described analytically. Mode matching between waveguides with different cross sections, ohmic, and diffraction losses in the resonators waveguides are studied numerically using Matlab simulation. An optical model of the FEL resonator as a non-symmetrical Fabri-Perot interferometer with possibly high losses is presented. An experimental method for determination of the internal round-trip reflectivity of the FEL resonator by direct measurement of the reflected wave resonant spectral peaks was developed and utilized. A special 3-grid variable out-coupling element was developed, fabricated, investigated and reported [6].

Among the results of the present investigation: the round-trip loss in the present version of the resonator (including all coupling elements) was approximately 50 %. Modification of the resonator structure was made in order to decrease this high loss. Based on our model calculations and measurements, this modification decreased the total internal losses to 35 %. This allowed achievement of first lasing operation of the FEL in the new configuration (with radiation out-coupling resonator) in September 2003 [11].

Contents

Chapter 1	Introduction	1
Chapter 2	Calculation of resonator losses using Matlab simulation	12
2.1	Introduction	12
2.2	Problem definition	13
2.3	The Talbot imaging and splitting effects	16
2.4	Curved Parallel Plates waveguide. Ohmic and diffraction losses	22
2.5	Transition from CPP to rectangular waveguides	32
2.6	Propagation in an overmoded rectangular waveguide (splitter). Ohmic and diffraction losses	40
2.7	Re-excitation of the fundamental TE_{01}^{CPP} mode in the Rectangular / CPP apertures junction	53
2.8	Estimation of the mitre bend losses	58
2.9	Conclusions	60
Chapter 3	Methods for characterization of the mm-wave resonator	62
3.1	Introduction	62
3.2	Experimental methods used for Q-factor measurement in the lumped – element circuit (single pole) model	63
3.3	The Measurement Scheme Used in the Present Study	68
3.4	The Adjustable Grid Reflector/Outcoupler	75

3.4.1	3-grid coupler	75
3.4.2	Measurement of the 3-grid coupler reflection coefficient	81
3.5	Fabri-Perot Resonator Model. Optical Approach	83
3.5.1	Fabri-Perot Interferometer with Losses	83
3.5.2	The Q-factor of a Fabri-Perot cavity resonator	92
3.5.3	Determination of the round-trip reflectivity parameter from measured resonance linewidth	93
3.5.4	Determination of the coupling transmission coefficient from measured spectral reflection pattern	94
3.5.5	Adaptation of the Fabri-Perot model to the experimental setup	98
3.5.6	Operation of the Fabri-Perot resonator in the oscillation regime of the FEL	101
Chapter 4	Measurement of round-trip reflectivity	104
4.1	Introduction	104
4.1.1	First experiment: measurements on the duplicate resonator system	105
4.1.2	Second experiment: reflection measurements the resonator installed in the FEL system	108
4.2	Analysis of measured data	112
Chapter 5	Conclusions	120
	Appendix	126
	References	132

List of Figures

1.1	Motion of charging particles through a FEL wiggler	1
1.2	Block-diagram and conceptual design of a FEL	3
1.3	CPP waveguide structure and dispersion diagram	5
1.4	Talbot effect splitter	9
1.5	Modified resonator with the bent reflector of Talbot length	10
2.1	FEL resonator comprised of different waveguide sections	13
2.2	Illustration of a symmetric mode splitting at $z = a^2/\lambda$	21
2.3	Curved plates geometry	22
2.4	Electric field profile in CPP	24
2.5	Electric field distribution in CPP waveguide	27
2.6	Explanation for the diffraction losses calculation	29
2.7	Longitudinal and transversal wave numbers	31
2.8	Profiles mismatch at the CPP-rectangular waveguide junction	34
2.9	Weight distribution of excited modes in rectangular waveguide	38
2.10	Comparison of main cross-section profiles: (a) Gauss-Hermit model; (b) Gaussian approximation	40
2.11	Power density flow propagation	43
2.12	Power losses per unit length	47

2.13	Total ohmic losses in the splitter as a function of z	49
2.14	Rectangular window plate terminating the splitter at $z=210$ mm	50
2.15	Power flow density distribution at the end of splitter	52
2.16	Power flow density distribution at the end of the splitter	53
2.17	Reconstruction of the original distribution due to Talbot effect	55
2.18	Gauss-Hermit model: re-excited modes power distribution	57
2.19	Description for the mitre bend reflector	58
2.20	Approximation of the bend region	59
2.21	Block-diagram of the resonator losses	60
3.1	Lumped-elements and distributed-elements resonators	64
3.2	A resonator and an external circuit	65
3.3	Thevenin and Norton equivalent circuits	66
3.4	Resonator configuration	69
3.5	(a) Schematic of the experimental setup for reflection coefficient measurements; (b) transmission line components: mitre bend and cylindrical corrugated waveguide	70
3.6	Measured resonator response (narrow peaks) masked by a large amplitude “low frequency” parasitic reflection pattern	72
3.7	Resonance peaks pattern of the excited FEL resonator obtained from Fig.3.5 by strongly reducing parasitic reflection	73
3.8	Calculated loaded Q-factor of the resonator: (a) peak #6, $f_0=100.41$ GHz; (b) $f_0=99.93$ GHz	74
3.9	Adjustable 3-grids coupler	75
3.10	(a) Structure and dimensions of the polarizing grids; (b) the grid in its supporting ring	76
3.11	Central grid: decomposition of the incident wave \bar{E} into E'_x and E'_y	77

3.12	Power transmission coefficient of the adjustable 3-grids coupler: (a) – for equidistant phase shift and spacing $\Phi_1 = \Phi_2$; (b) – for non-equal spacing $\Phi_2 = \pi/4$, $\Phi_1 \neq \Phi_2$.	80
3.13	Schematic of setup for the reflection coefficient measurement	81
3.14	Reflection measurement: (a) single grid; (b) set of three parallel grids	82
3.15	Schematic view of Fabri-Perot resonator	84
3.16	Transmitted (a) and reflected (b) power pattern for a Fabri-Perot resonator	86
3.17	Reflection of an ideal Fabri-Perot interferometer; $r_1 = r_2$	90
3.18	Measurement transmission line terminated by a RF source and by resonator cavity at each end respectively	98
3.19	Two Fabri-Perot interferometers in serial	99
3.20	Reflectivity of two FP interferometers in series	101
3.21	Resonant peak of reflected power for several gain values for parameters $R_r = 0.5$, $R_1 = 0.98$	103
4.1	(a) Experimental setup for measurement of the resonator, excited by an appropriate aperture: setup diagram; (b) photograph of the experimental setup	106
4.2	(a) Dependence of the reflection pattern of the resonator on the central grid angle in the coupler; (b) zoom on a single resonant peak; (c) frequency shift of the resonant peak for the different longitudinal coupler positions	108
4.3	Setup for resonator reflectivity measurement inside the FEL tank	109
4.4	Reflection from the resonator cavity measured for different coupling coefficients: (a) In a wide frequency range; (b) blow-up of a single resonant longitudinal mode dip of the resonator in Fig. 3.30(a)	111
4.5	The Lorenz curve approximation: y_0 – off-set of Lorenzian curve; x_c, y_c – coordinates of the resonant maxima; $\Delta f_{FWHM} = \delta f_{1/2} = w$ – width of the resonance peak at -3dB level $(y_c - y_0)/2$	113
4.6	Exact dependence of the \bar{C} parameter (red) on the FWHM frequency width $\delta f_{1/2}$ of the FP resonator and the approximation of Eq.4.6 (green).	115

4.7	An example of the Lorenz approximation curve-fitting procedure for particular resonance peak	116
4.8	Quality of Lorenzian fit approximation. The single measured resonance peak for the different coupling conditions (different coupler grid angles).	117
4.9	Total round-trip reflectivity of the resonator calculated for a typical resonant peak: (a) inside the FEL tank; (b) in the laboratory experiment	119
5.1	Modified FEL resonator	121
5.2	Multi-peak analysis of resonant peaks before (a) and after (b) resonator modification	123

List of Tables

2.1	List of resonator losses	15
2.2	Geometry of the CPP waveguide and its fundamental mode propagation parameters	25
2.3	Distribution of losses in the FEL resonator	61
4.1	An example of the Origin curve-fitting procedure output	117
5.1	Measured and calculated round trip reflectivity parameters	120
5.2	Measured and calculated round trip reflectivity parameters after modification	122
5.3	Threshold gain and the corresponding threshold current values	124

Chapter 1

Introduction

In this work we investigate a novel resonator intended for use in a Free Electron Laser. Free Electron Lasers (FELs) differ from most other types of laser as they do not utilize a lasing medium in the traditional meaning of this term. In fact, the lasing medium for FELs is a high vacuum. A charged particle beam from an accelerator passes through a structure called an “undulator” or “wiggler” array - a series of powerful magnets of alternating polarity (Fig1.1).

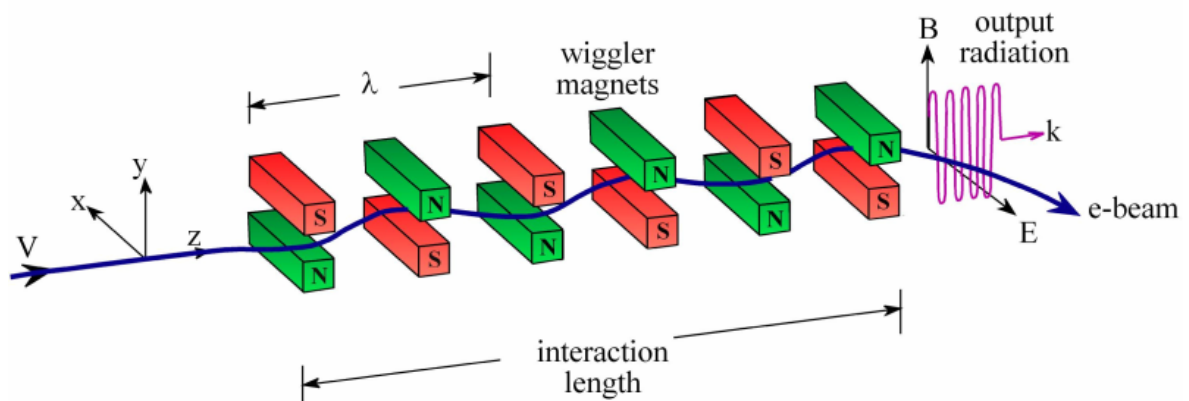


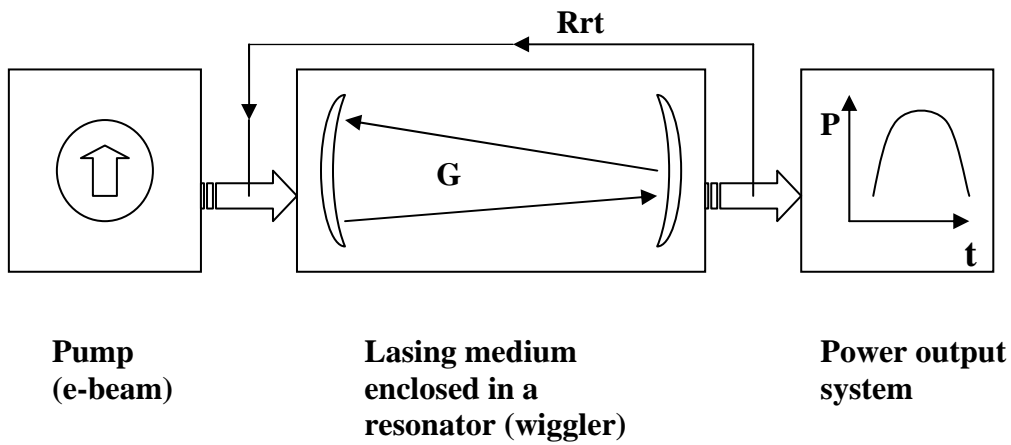
Fig. 1.1 Motion of charging particles through a FEL wiggler.

As the charged particles oscillate back and forth in response to the magnetic field, photons are emitted in all directions - some along the axis of the beam. Electromagnetic radiation can be emitted whenever a charged particle is

accelerated in a magnetic field (this is called synchrotron radiation). Mirrors placed before and after the magnets structure completes the laser resonator. As photons along the beam axis bounce back and forth, they stimulate new photons to be emitted in the same direction – “stimulated emission”.

The wavelength of FEL 'light' depends on two main parameters: the energy of the electron beam and the period of the wiggler structure. This is why the coherent output of an FEL can span the electromagnetic spectrum ranging from microwave to X-Rays and may be continuously tuned over a wide wavelength band.

The block diagram of a FEL is similar to other kinds of lasers and consists of a pump (wiggler), a lasing medium (interaction region), a high-quality resonator and a power output system (Fig. 1.2).



(a)

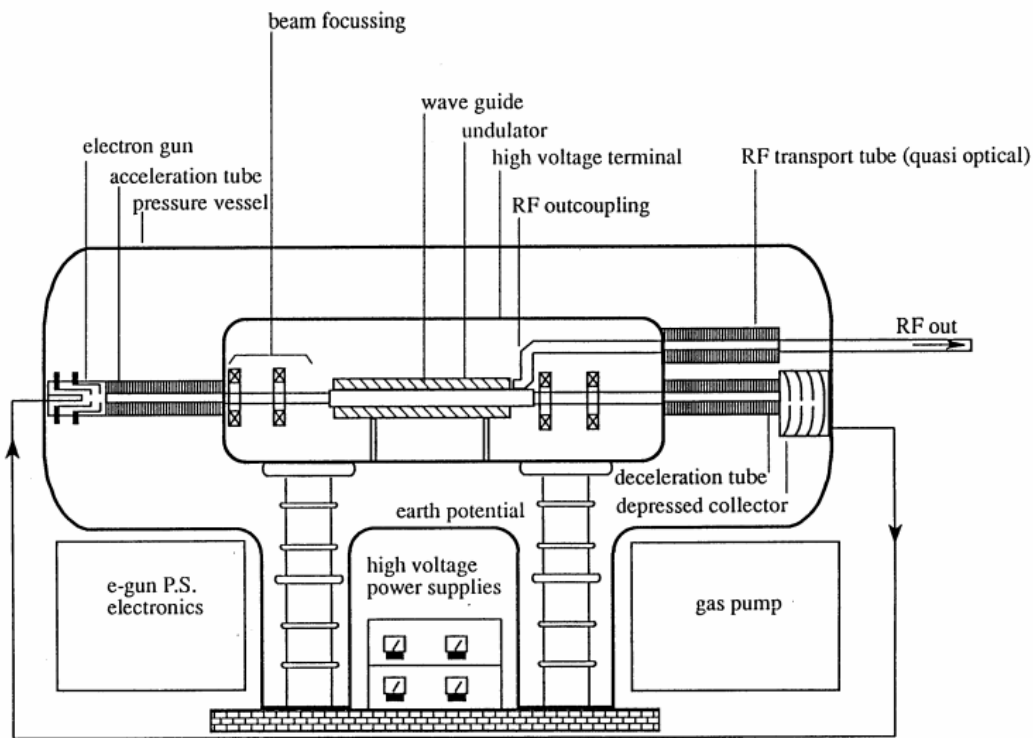


Fig. 10: A conceptual scaled design of a compact FEL for mm-wave radiation. The longitudinal dimension is about 2.5m.

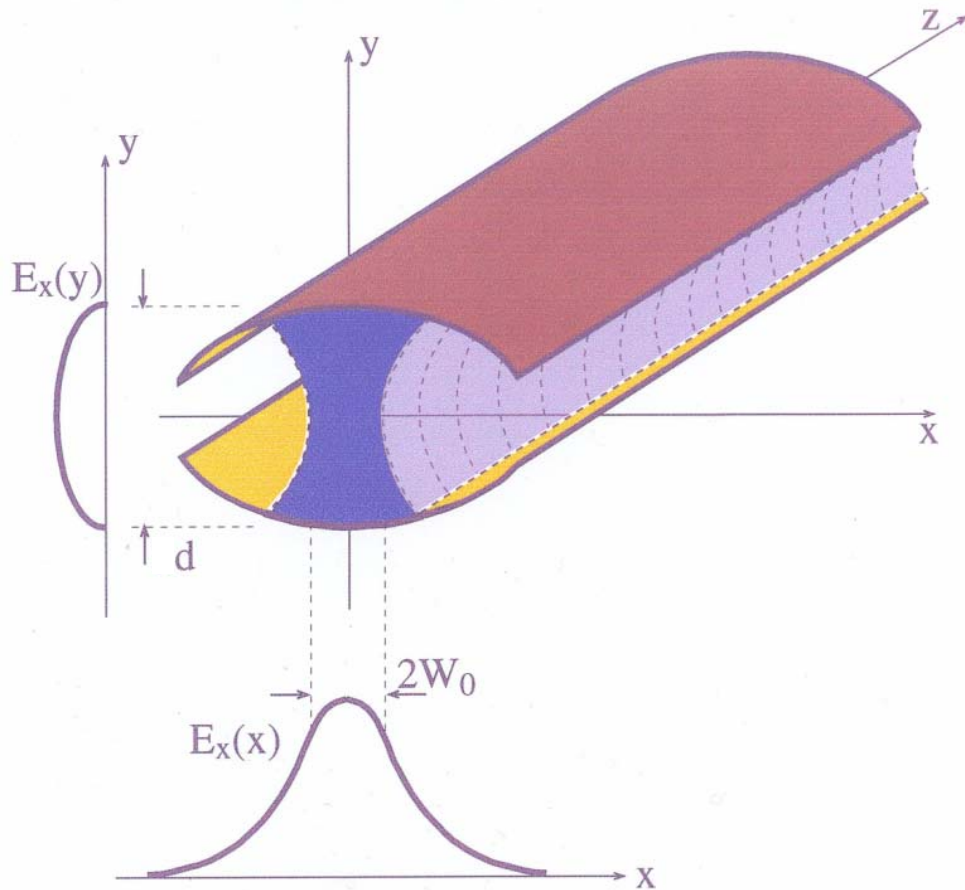
(b)

Fig.1.2 Block-diagram of an electrostatic accelerator free electron laser (a); conceptual design of a FEL for mm-wave radiation (b).

The electrostatic accelerator FEL that we employ is designed to operate at the mm-wave (W-region) near a frequency of 100 GHz. Electrons of about 60 keV energy from a electron gun are accelerated up to energy of 1.5 MeV provided by an electrostatic Van-der-Graaf generator before entering into the resonator region.

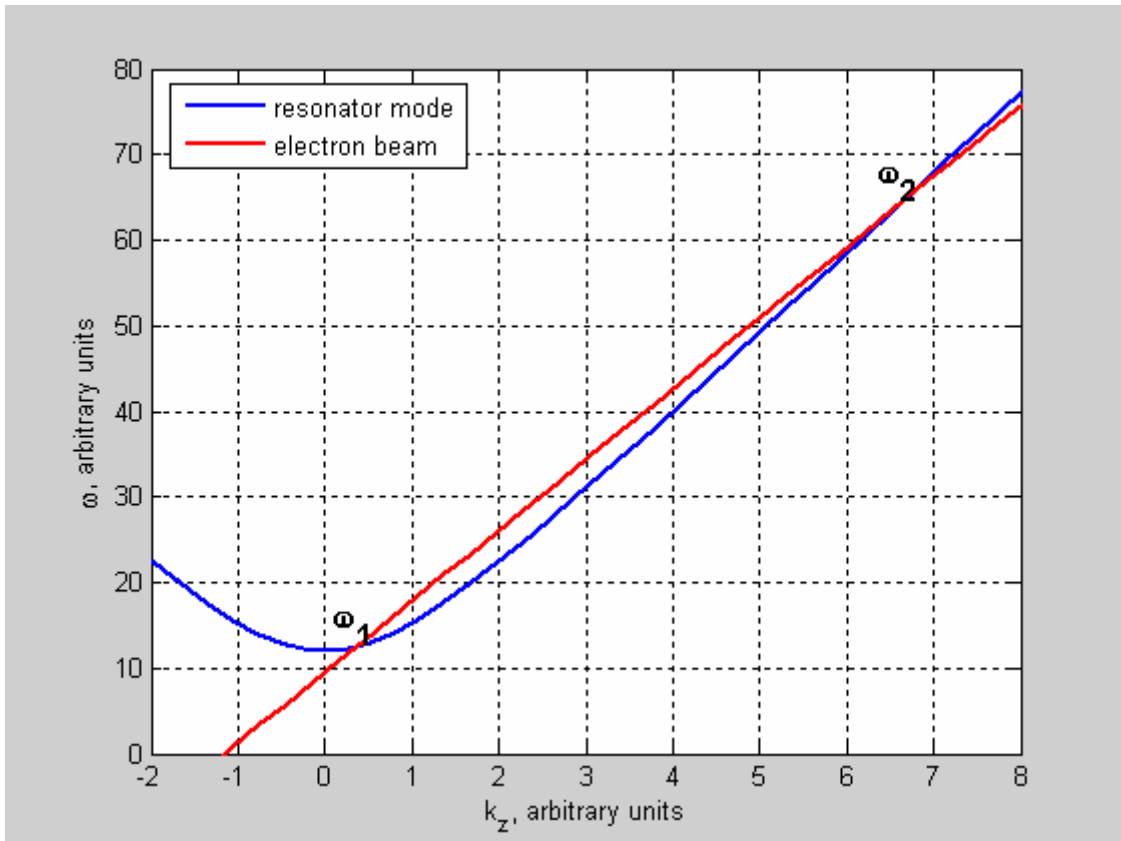
The resonator of our FEL consists of several waveguide sections of differing profiles and is integrated into the wiggler system so that interaction between the electron beam and the magnetic field of the wiggler occurs inside the waveguide cavity. This cavity uses curved parallel plate (CPP) waveguide (two elliptically shaped copper plates) open at the narrow ends. This

waveguide was designed in such a way that the electron beam at the design energy can interact only with the fundamental mode TE_{01} according to the dispersion relation. The waveguide geometry, fundamental mode description and dispersion diagram are shown in the following figure:



$$E_x = E_0 \cos\left(\frac{\pi}{d} y\right) e^{-\frac{x^2}{W_0^2}} e^{-i\beta z}$$

(a)



(b)

Fig.1.3 CPP waveguide and its fundamental mode structure (a); dispersion diagram (b).

In order to have positive feedback from resonator mirrors, two wave splitters (reflectors, based on overmoded rectangular waveguides shorted with a perforated mirror at one end) were placed at both terminations of the CPP waveguide as shown in Fig.1.4. In previous experiments ([26], [27]), the same reflectors (shown in Fig.1.4(a)) were placed in both ends of the CPP waveguide. The length of each of these splitters equals to one half of the Talbot effect optical imaging distance (described subsequently in Chapter 2). At half the Talbot imaging distance, the rectangular waveguide provides splitting of the original field distribution at the termination plane of the rectangular waveguides, where reflecting mirrors are placed. This effect allows perforation

of the center of each metallic mirror as there is no field at this position and this makes it possible to pass the electron beam through the resonator without disturbing the cavity field high round trip reflectivity. This is described in Fig.1.4.

Operation of the FEL with this type of resonator configuration and measurements of the power generated was reported earlier ([26], [27]). Only a small part of the generated energy was coupled out in these previous measurements from the cavity through the perforated mirror and a vacuum window at the end of the accelerator beam line. This is because the electron beam and the out coupled RF power were not physically separable after exciting the resonator mirror, and thus the RF power could not be transported efficiently out of the accelerator tank. In the more recent experiments at the new site of the EA-FEL in Ariel a new splitter/reflector configuration was used. To separate the laser RF radiation from the electron beam and to out-couple the desired part of the RF energy, the beam output splitter was substituted by a bent reflector, that consists of two identical splitters at right angles one to another mitered by the slanted perforated plane metallic mirror as it shown in Fig. 1.5.

As a result of such modification at the plane of the out-coupling element at the top of the vertical section (see Fig.1.5), the field distribution of CPP waveguide is reconstructed, because it is situated exactly one Talbot imaging distance from the CPP waveguide end. The out-coupled power from the resonator is then controlled, by the coupling element, away from the electron beam.

Lasing in a FEL is achieved only if a high quality (low loss) resonator cavity is employed. High total round-trip reflectivity of the resonator provides possibility of oscillation built-up in the resonator and start of the lasing process. The round trip oscillation parameter defines quantitatively the value of the threshold gain and, consequently, the threshold current of start of oscillation. In a regular laser the oscillation condition for the threshold gain constant γ_{th} is [1]:

$$r_1 r_2 e^{[\gamma_{th} - 2\alpha]l} = 1 \quad (1.1)$$

where r_1, r_2 are the amplitude reflection coefficients of the back and front mirrors, and α is the distributed loss constant of the amplitude along the interaction length l . After taking the absolute value square of (1.1) and using a more general notation, it can be written as:

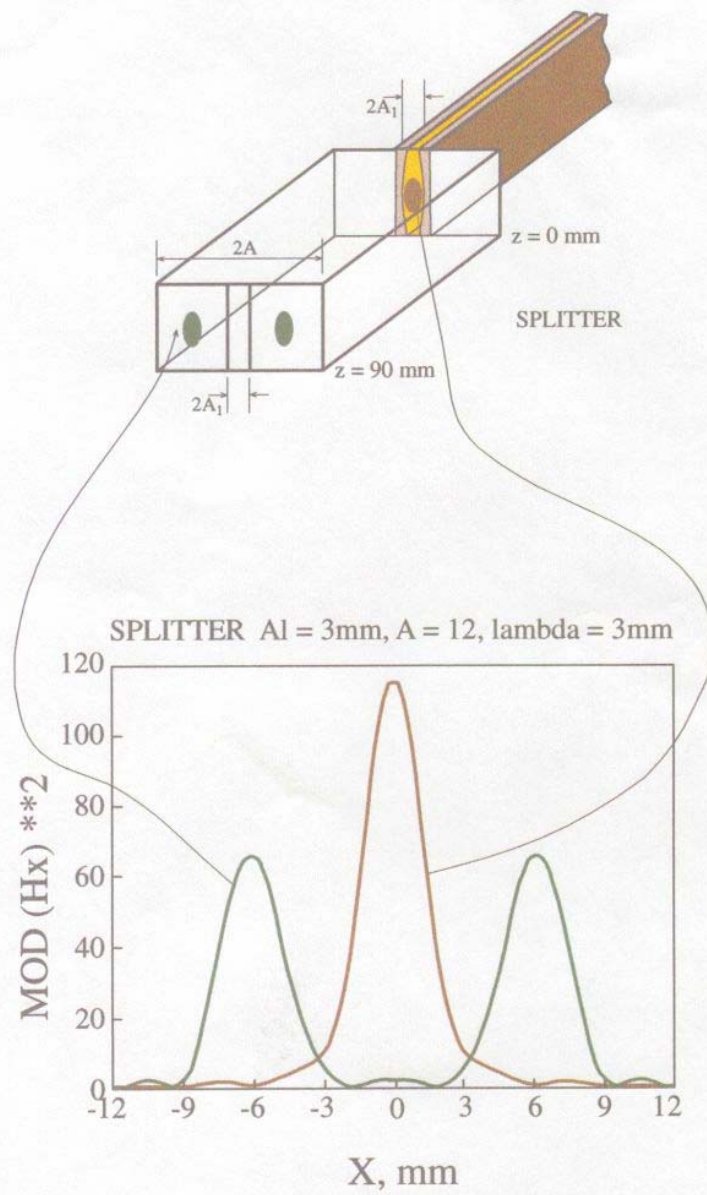
$$GR_{rt} = 1 \quad (1.2)$$

where R_{rt} is the round-trip power reflectivity of the resonator and G is the round trip gain (which in the case of the FEL is simply the single-path gain, since it exhibits gain only in one direction). The total round-trip losses of the resonator are $L_{tot_rt} = 1 - R_{rt}$. In the limit $(1 - R_{rt}) \ll 1$ one can approximate $1/R_{rt} \sim 1 + L_{tot_rt}$ and thus the oscillation condition can be written then in terms of the incremental gain and the resonator losses:

$$G - 1 = L_{tot_rt} \quad (1.3)$$

Clearly, characterization of the resonator and an estimate of its round-trip reflectivity are most important for proper laser operation.

Talbot Effect Reflector



ד"ר 24 / נובמבר / 3

(a)

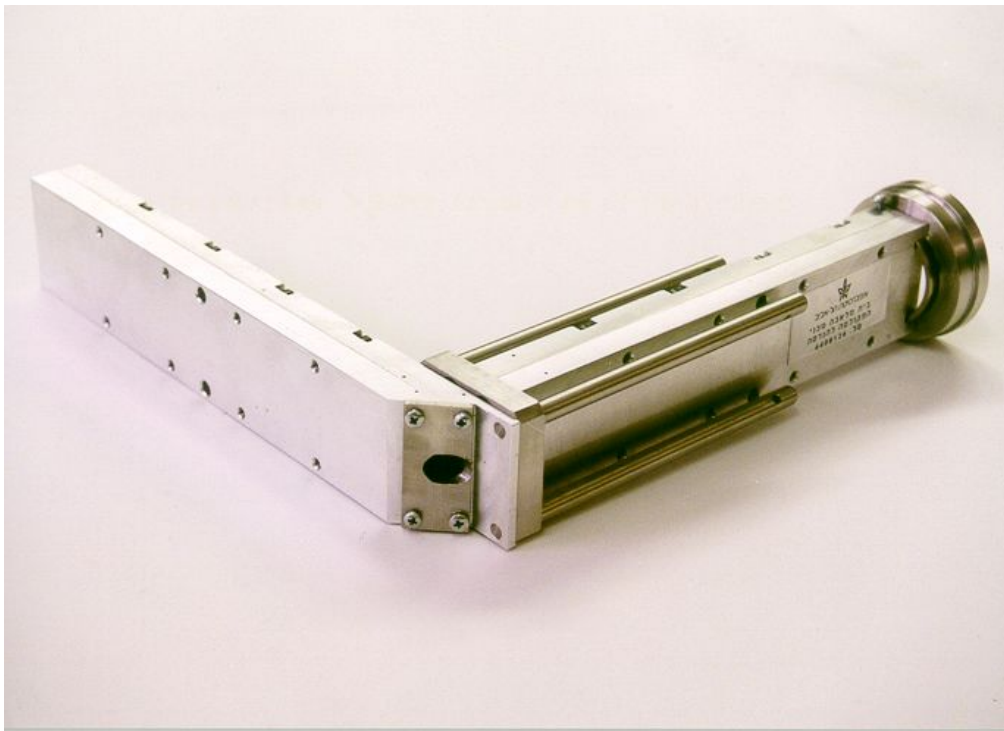
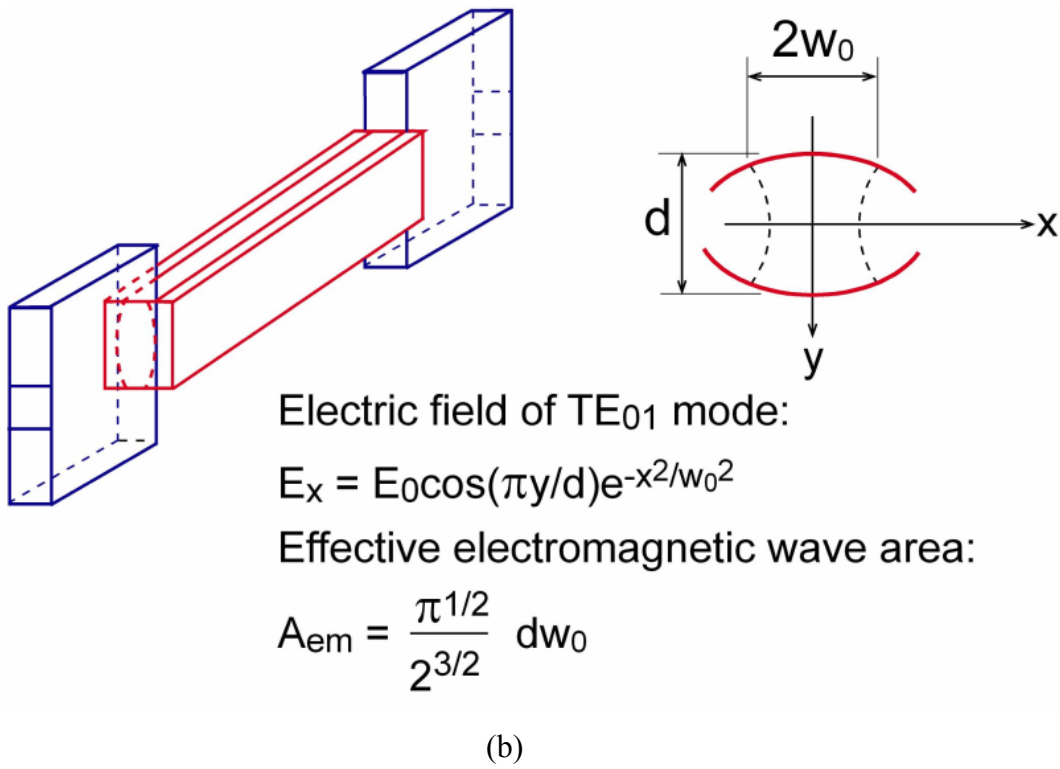


Fig.1.4 Talbot effect splitter (a); perforated splitters at the CPP waveguide ends (b); manufactured Talbot splitter (c).

DENISOV (TALBOT EFFECT) REFLECTOR

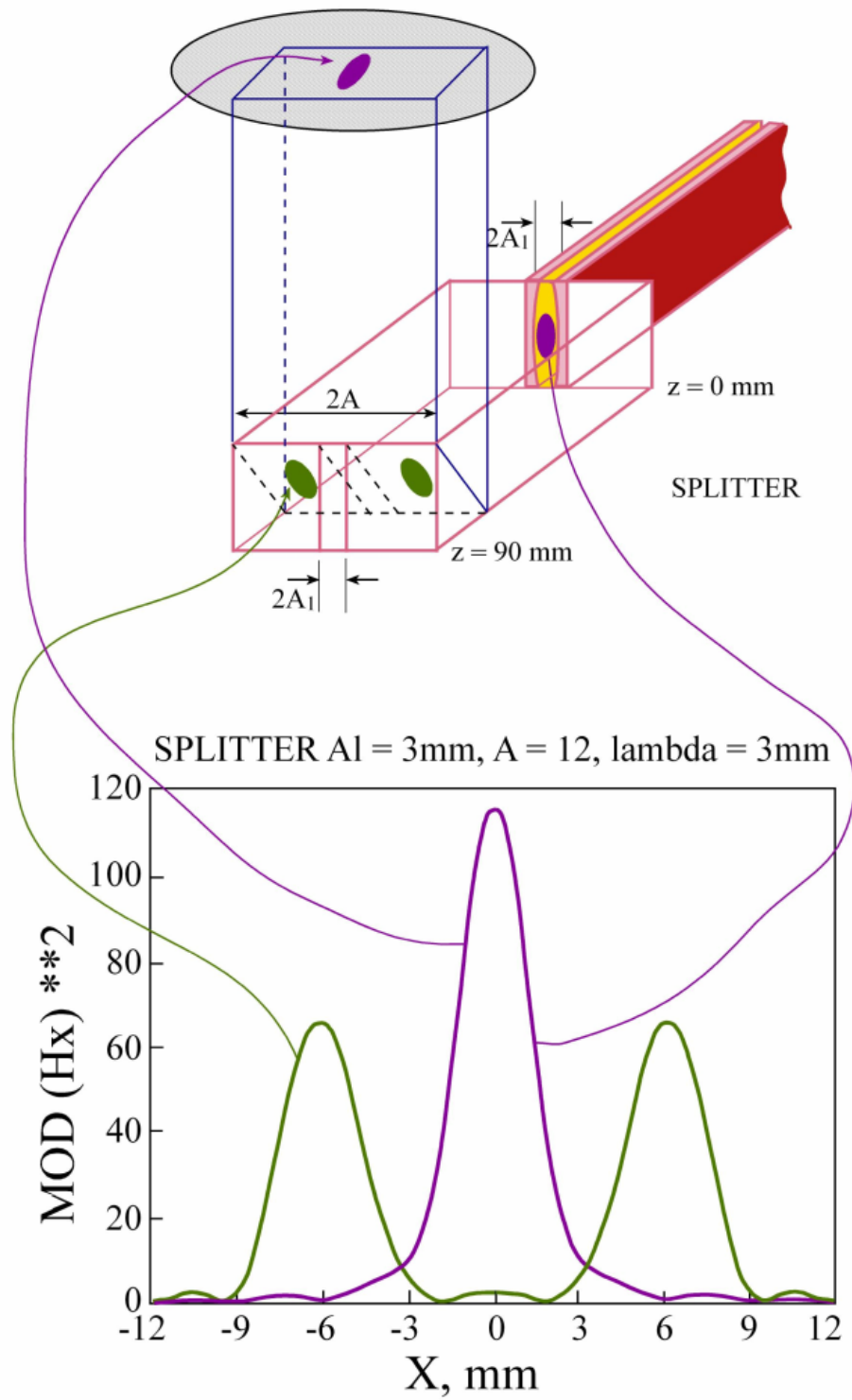


Fig.1.5 Modified resonator with the bent reflector of Talbot length.

This work, for the most part, is experimental. All measurements of the FEL resonator were made without the presence of an electron beam – “cold” measurement. Therefore, interpretation of the measured data required a theoretical formulation of the resonator parameters; comparison was made to results derived from different resonator models.

Matlab code simulation of the electromagnetic field distribution is described in Chapter 2. An optical approach for interpretation of data measured on the resonator that we used is discussed in Chapter 3. A non-symmetric Fabri-Perot interferometer model for the FEL resonator is also discussed in chapter 3. Measurements were made and used in calculation of the FEL resonator parameters (Chapter 4). Chapter 5 presents conclusions of this thesis that led to the modification of the resonator.

References

1. Yariv A., *Introduction to Optical Electronics*. Holt, Rinehart and Winston, New York, 1976.
2. Collin Robert E., *Foundations for microwave engineering*. 2nd ed. McGraw-Hill, 1992.
3. Ulrich R., Bridge T.J. and Pollack M.A., *A variable Output Coupler for Far Infrared Lasers*. Proc. Symp. On Submillimeter Waves, Polytechnic Inst., Brooklyn, 605-614, 1970.
4. Saleh A.A.M., *An adjustable quasi-optical bandpass filter – part1: theory and design formulas*. IEEE Trans. MTT, vol. 22, no.7, pp.728-734, 1974.
5. Cornbleet S., *Microwave optics*. Academic press, 1976.
6. **Yulia&Yakover Internal report**
7. Haus H., *Waves and Fields in Optoelectronics*. Prentice-Hall, 1984.
8. Fox A.G. and Li T., *Resonant Modes in a Maser Interferometer*. The Bell System Technical Journal, March, 1961.
9. Culshaw W., *Reflectors for a Microwave Fabry-Perot Interferometer*. IRE Trans. On Microwave and Theory Techniques, vol.MTT-7, pp.182-189; April, 1959.
10. Culshaw W., *High Resolution Millimeter Wave Fabry-Perot Interferometer*. IRE Trans. On Microwave and Theory Techniques, vol.MTT-8, pp.182-189; March, 1960.
11. Faingersh A., Gover A., Eliran A., Kapilevich B. *Concluding report: Measurements and calculation of round-trip reflectivity in the FEL waveguide resonator before and after modification and estimate of threshold current improvement*. Internal report of FEL group, 31-Jan-06, Tel-Aviv University.
12. Yakover I., Pinhasi Y., Gover A. *Study of waveguide resonators for FEL operating at submillimeter wavelengths*. Nuclear Instr. And Methods in Physics Research, A 375, (1996), 260-263.

13. Nakahara T., Kurauchi N., *Guided beam waves between parallel concave reflectors*. IEEE Transactions of Microwave Theory and Techniques, v.MTT-15, no2 (1967), p.66.
14. Lurie Y., *Parallel Curved Plates (PCP) versus rectangular waveguide*. Internal report of FEL group, 14-March-02, Tel-Aviv University.
15. Papas ...
16. Kazantsev Yu.N., Sov. Radio Eng. Elec. Phys., 15 (1970), p.963
17. Vaganov
18. Anaton A., Markish O.,
19. Ginzton E. L., *Microwave Measurements*. New York: McGraw-Hill, 1957, Chap. 9.
20. Lebedev
21. Altman
22. A. Asija and A. Gundavajhala, *Quick measurement of unloaded Q using a network analyzer*, *Rf Design*, pp. 48-52, October 1994.
23. M. Sucher, and J. Fox (eds.), *Handbook of Microwave Measurements*. New York: Polytechnic Press, 1963, Chapter
24. G. L. Matthaei, L. Young and E. M. T. Jones, *Microwave Filters, Impedance-Matching Networks, And Coupling Structures*. New York: McGraw-Hill, 1964, Chapter 11.
25. D. Kajfez and E. J. Hwan, Q-factor measurement with network analyzer, *IEEE Trans. Microwave Theory Tech.*, vol. MTT-32, pp. 666-670, July 1984.
26. Abramovich A, Pinhasi Y, Yakover YM, Gover A, Sokolowski JS, Canter M. *Study of radiation build up and mode evolution in the Israeli electrostatic accelerator free-electron laser oscillator* [Journal Paper], IEEE Transactions on Plasma Science, vol.27, no.2, April 1999, pp.563-7. Publisher: IEEE, USA.
27. Sokolowski JS, Abramovich A, Arensburg A, Chairman D, Draznin M, Eichenbaum AL, Gover A, Kleinman H, Pinhasi Y, Yakover YM, Rosenberg A, Shiloh J, Cohen N, Levin LA, Shahal O. *First lasing of the Israeli tandem electrostatic accelerator free electron laser* [Conference Paper], Proceedings of the 1997 Particle Accelerator Conference (Cat. No.97CH36167). IEEE. Part vol.1, 1998, pp.906-8 vol.1. Piscataway, NJ, USA.

Chapter 2

Calculation of resonator losses using Matlab simulation

2.1 Introduction

In this chapter, we evaluate the field distribution and wave propagation in our FEL resonator. Since the resonator is comprised of several waveguides with differing profiles, dimensions and electrical properties, wave excitation and propagation is also different in different parts and planes of such a resonator. Furthermore, the dimensions of the waveguides used are much greater than the radiation wavelength, thus enabling a number of transverse modes to be excited and to propagate through the resonator (makes it “overmoded”). This is a quasi-optical situation in general design of microwave devices there are usually a single mode waveguides. This multimode nature of mm-wave cavity leads to some quasi-optical effects, which may be utilized to achieve the desired performance. It may also lead to some undesirable effects such as diffraction, additional losses in the waveguide walls and decrease of efficiency. In this chapter, we estimate the ohmic and the diffraction losses in an overmoded mm-wave resonator by computer simulation of excitation and propagation of electro-magnetic waves inside the combined waveguide resonator. The simulations are repeated based on two different mathematical models; each is a different representation of modes supported by Curve Parallel Plate (CPP) waveguide. The coupling element of the resonator with the reflection tuning mechanism is not considered at all in this chapter and will be discussed later in this work.

2.2 Problem definition

A schematic of the FEL resonator is presented in Fig.2.1. This resonator is comprised of long curved parallel plates (CPP) waveguide placed inside a magnetic wiggler, within which the interaction between an accelerated e-beam and a waveguide radiation mode takes place, and the rectangular waveguide Talbot-effect reflector structures, which incorporate open holes to let the electron beam enter it and exit out.

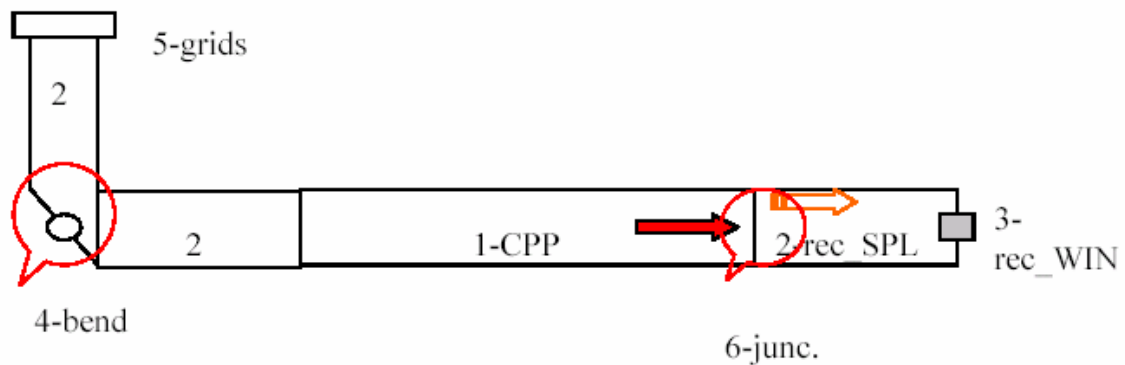


Fig.2.1 FEL resonator comprised of different waveguide sections.

An accelerated electron beam enters the resonator through the rectangular hole 3, traverses through the rectangular waveguide 2, the Curved Parallel Plates (CPP) waveguide 1 and the rectangular waveguide 2. It exits from the resonator through a circular hole in the bend section 4. Because of modes dispersion in the waveguide, only one mode out of all the transverse modes of the overmoded CPP waveguide has phase velocity, which can be synchronized with the wiggling electron current. The FEL is designed to interact with the fundamental mode of the waveguide (the TE_{01}^{CPP} mode). Although the dimensions of CPP waveguide allow other high-order modes to be excited, they do not interact with the beam and therefore, if excited, they do not experience gain, and decay relatively fast as the modes traverse back and forth along the resonator. Thus, such high-order modes may be considered as ‘parasitic’ (considered as

diffraction losses), and when excited, they eventually dissipate their energy to the resonator walls.

Radiation that is generated in the CPP waveguide in the TE_{01}^{CPP} mode and propagates to the right, arrives to junction 6 (between CPP and the rectangular waveguide), and excites in the overmoded rectangular waveguide many transverse modes having different amplitudes and propagation constants. The TE_{01}^{CPP} mode has field distribution with a maximum in the center of the waveguide, which decay to zero near the walls. A field distribution of the TE_{01}^{CPP} mode is transmitted into the entrance of waveguide 2 (under a quasi-optical assumption of the absence of reflected wave at the junction 6). The rectangular waveguide modes, excited by this distribution, propagate toward window 3 and after traversing the half Talbot length $L_T/2 = 210$ mm are reflected from the conducting wall back to the CPP waveguide.

The Talbot effect, described in the next section, is an imaging effect that takes place in any overmoded waveguide at a certain distance L_T . At this particular distance, all the transverse modes interfere in phase and reconstruct coherently a replicated image of the input radiation field. It is further shown in the next session, that at half the distance $L_T/2$ the modes interfere in such a way that a single spot at the entrance to the waveguide splits into two spots with a space in between.

The Talbot image splitting effect is taken advantage of in the straight splitter reflector section (part 2 in Fig.2.1). The interference of the propagating modes creates a split image of two spots at the position of the reflecting mirror at the end of the section (part 3 in Fig.2.1). This mirror is made out of two parts, which are spaced 10mm apart, leaving an opening ('window') through which the electron beam can be transported. Because the image at this point is split at this position, the window opening does not affect the radiation pattern and it is reflected almost at is entirely back towards the CPP – rectangular waveguide junction 6. Arriving back to this position, the radiation beam goes in its round trip through an entire Talbot length L_T , and thus regenerates at the entrance to the CPP the original distribution of the mode TE_{01}^{CPP} , that was coupled into the rectangular waveguide.

Except for slight distortion due to imperfect imaging by the Talbot effect and due to imperfect reflection at the end mirror because of its window opening, the pattern of the back-coming beam reconstructs well the TE_{01}^{CPP} mode pattern. It, consequently,

excites it back inside the CPP waveguide with high efficiency. The mode now propagates up to the junction with the bent Talbot reflector at the left side (Fig.2.1)

The situation on the other side of the resonator is similar, but the splitter consists of two identical half-Talbot-length rectangular waveguides coupled by a mitre bend with 45° mirror. Except for the bend section (that will be discussed separately), the one-way propagation in the bent splitter/coupler is equivalent to one round-trip of propagation in the straight splitter on the other side. The mitre bend transmits the split (two spot) radiation field to the vertical rectangular waveguide section where the two spots merge into a single spot by the inverse Talbot imaging effect. The radiation is then partly coupled out through the grids reflector and partly reflected back into the resonator.

The ohmic losses in the waveguide walls should be taken into account. The following losses in the resonator (in one round-trip) should be taken into account:

Location	Nature of losses	x times occurs in round-trip
CPP-splitter transition	diffraction	2
CPP waveguide	diffraction	2
CPP waveguide walls	ohmic	2
Splitter walls	ohmic	6
Splitter-CPP transition	diffraction	2
Input and output electron beam windows	diffraction	3
Mitre bend section	diffraction	2

Tab.2.1 List of resonator losses.

The main goal of this work is to estimate these losses and measure them in the experimental waveguide structure.

2.3 The Talbot imaging and splitting effects

Self-imaging (Talbot effect) requires the excitation of multiple modes in the waveguide by the input field. The input field at the CPP-rectangular waveguides junction ($\mathbf{E}^{CPP} = \mathbf{E}_{in}^{rec}$ at $z = 0$) may be written as a sum of the full set of rectangular waveguide modes $\hat{\mathbf{e}}_{mn}^{h,e}$ as follows:

$$\mathbf{E}^{CPP}(x, y, 0^-) = \mathbf{E}^{rec}(x, y, 0^+) = \sum_{m=0}^M \sum_{n=0}^N (A_{mn}^h \hat{\mathbf{e}}_{mn}^h(x, y) + A_{mn}^e \hat{\mathbf{e}}_{mn}^e(x, y)) \quad (2.1)$$

where $A_{mn}^{h,e}$ represents the amplitude of the mn -th TE (h) or TM (e) waveguide mode, which is defined in terms of overlap integral [15]:

$$A_{mn}^{h,e} = \frac{\int \int \mathbf{E}^{CPP}(x, y) \hat{\mathbf{e}}_{mn}^{h,e}(x, y) dx dy}{\int \int [\hat{\mathbf{e}}_{mn}^{h,e}(x, y)]^2 dx dy} \quad (2.2)$$

This is an eigenmodes decomposition where the $\hat{\mathbf{e}}_{mn}^{h,e}$'s are the TE or TM eigenmodes of the rectangular waveguide accordingly. The field propagation along z in the rectangular waveguide is then described as follows:

$$\mathbf{E}^{rec}(x, y, z) = \sum_{m=0}^M \sum_{n=0}^N (A_{mn}^h \hat{\mathbf{e}}_{mn}^h(x, y) + A_{mn}^e \hat{\mathbf{e}}_{mn}^e(x, y)) e^{-j\beta_{mn}z} \quad (2.3)$$

where the β_{mn} 's are the propagation constants of each mode of the rectangular waveguide.

Self-imaging effect (Talbot Effect)

The transverse propagation constant for the mn -th mode of a rectangular waveguide is given by

$$k_{co,mn} = \sqrt{\left(\frac{m\pi}{a}\right)^2 + \left(\frac{n\pi}{b}\right)^2} \quad (2.4)$$

where a and b are the transverse dimensions of the rectangular waveguide aperture. The longitudinal propagation constant is

$$\beta_{mn} = \sqrt{k_0^2 - k_{co,mn}^2} \quad (2.5)$$

In an “overmoded waveguide”, where $k_0 = 2\pi/\lambda$ for modes far from cut-off ($k_{co,mn} \ll k_0$) (which corresponds to paraxial rays approximation) a second order Taylor expansion of (2.5) results in: $\beta_{mn} \cong k_0 - k_{co,mn}^2 / 2k_0$. This can be written as follows:

$$\beta_{mn} \approx k_0 - \frac{\pi\lambda}{4} \left[\left(\frac{m}{a}\right)^2 + \left(\frac{n}{b}\right)^2 \right] \quad (2.6)$$

Note, that for a fixed n index and for the two first indexes $m = 0$ and $m = 1$:

$$\beta_{0n} - \beta_{1n} = k_0 - \frac{\pi\lambda}{4} \left(\frac{n^2}{b^2}\right) - \left(k_0 - \frac{\pi\lambda}{4} \left(\frac{n^2}{b^2}\right) - \frac{\pi\lambda}{4} \left(\frac{1}{a^2}\right) \right) = \frac{\pi\lambda}{4a^2}. \text{ For any index } m,$$

$$\beta_{mn} \approx \beta_{0n} - \frac{\pi\lambda}{4} \left(\frac{m}{a}\right)^2 \quad (2.7)$$

Using this notation, we can write the electric (or magnetic) field for fixed n :

$$\begin{aligned} \mathbf{E}_x(x, y, z) &= \sum_m A_{mn} \tilde{\mathbf{e}}_{mn,x}(x, y) e^{-j\beta_{mn}z} \\ &= \sum_m A_{mn} \tilde{\mathbf{e}}_{mn,x}(x, y) e^{-j\beta_{0n}z} e^{j\frac{\pi\lambda}{4a^2}m^2z} = \sum_m A_{mn} \tilde{\mathbf{e}}_{mn,x}(x, y) e^{-j\beta_{0n}z} e^{j\phi_m} \end{aligned} \quad (2.8)$$

where

$$\phi_m(z) = \frac{\pi\lambda}{4a^2} m^2 z \quad (2.9)$$

is a phase. The distance, where the phase difference between the m -th mode and the fundamental mode is a multiple of 2π for any m is found from the condition:

$$\begin{aligned} \frac{\pi\lambda}{4a^2} z_m &= 2\pi N \Rightarrow \\ z_N &= \frac{8a^2}{\lambda} N, \quad N = 1, 2, 3, \dots \end{aligned} \quad (2.10)$$

At this distance $\phi_m(z_N) = 2\pi Nm^2$, and $e^{i\phi_m} = 1$. Consequently, there will always be imaging (up to a constant phase) at position $z_N = NL_i$, where $L_i = \frac{8a^2}{\lambda}$:

$$\mathbf{E}(x, y, L_i) = e^{-j\beta_{0n}L_i} \mathbf{E}(x, y, 0) \quad (2.11)$$

Equation (2.11) describes the well known self-imaging (Talbot) effect, published by Henry Fox Talbot in 1836 [28]. The original effect related to a periodic

object in the transverse dimension (which is an equivalent diffraction problem). Suggestions on using this effect in overmoded waveguides was first mentioned in [31], [32]. One can find more information about recent applications of Talbot effect in [12], [29], [30]. We will consider now some special cases of this effect.

Flip (mirrored) imaging effect

At $L_m = \frac{L_i}{2} = \frac{4a^2}{\lambda}$, the phase of a m -th mode is (see Eq.(2.9)):

$$\phi_m(L_m) = m^2 \pi = \begin{cases} 2N\pi, & m - \text{even} \\ (2N+1)\pi, & m - \text{odd} \end{cases} \quad (2.12)$$

$$N = 1, 2, 3 \dots$$

Since the profile function of the modes of the rectangular waveguide are either symmetric or anti-symmetric:

$$\tilde{\mathbf{e}}_{mn,x}(-x, y) = (-1)^m \tilde{\mathbf{e}}_{mn,x}(x, y) \quad (2.13)$$

we get from Eq. (2.8) :

$$\mathbf{E}_x(x, y, L_m) = \sum_m A_{mn} \tilde{\mathbf{e}}_{mn,x}(x, y) e^{-j\beta_{0n}L_m} (-1)^m \quad (2.14)$$

$$= \sum_m A_{mn} \tilde{\mathbf{e}}_{mn,x}(-x, y) e^{-j\beta_{0n}L_m} = e^{-j\beta_{0n}L_m} \mathbf{E}_x(x, y, 0)$$

Any original distribution at $z = 0$ will be imaged and mirrored reversed with respect to plane $x = 0$ (center of aperture). Therefore, because of the symmetry of the modes, first imaging plane is at length $z = L_m = \frac{L_i}{2}$.

Symmetric initial field

If the field pattern at $z = 0$ is symmetric relative to the plane $x = 0$, it will excite only even ($m = 2\mu$) modes in the x dimension. In this particular case, we will get imaging even at shorter distance:

$$L_t = \frac{L_m}{2} = \frac{L_i}{4} = \frac{2a^2}{\lambda} \quad (2.15)$$

This can be directly verified by substituting in (2.9):

$\phi_m(L_t) = \frac{\pi m^2}{2} = 2\pi\mu^2$, $e^{i\phi_m} = 1$ Thus for a symmetric input pattern first imaging occurs at $z = L_t$. We will call further to this distance ‘‘Talbot length’’. For the parameters of the FEL reflector $\lambda = 3$ mm and $a = 25$ mm, the $L_t = 417$ mm.

Splitting of a symmetric mode distribution

Assuming symmetric (relative to plane $x = 0$) initial (at $z = 0$) field distribution polarized in the x dimension, one could insert into the rectangular waveguide along its entire length a thin conducting plate at its center ($x = 0$; $-b/2 < y < b/2$) without disturbing the field (see Fig. 2.2).

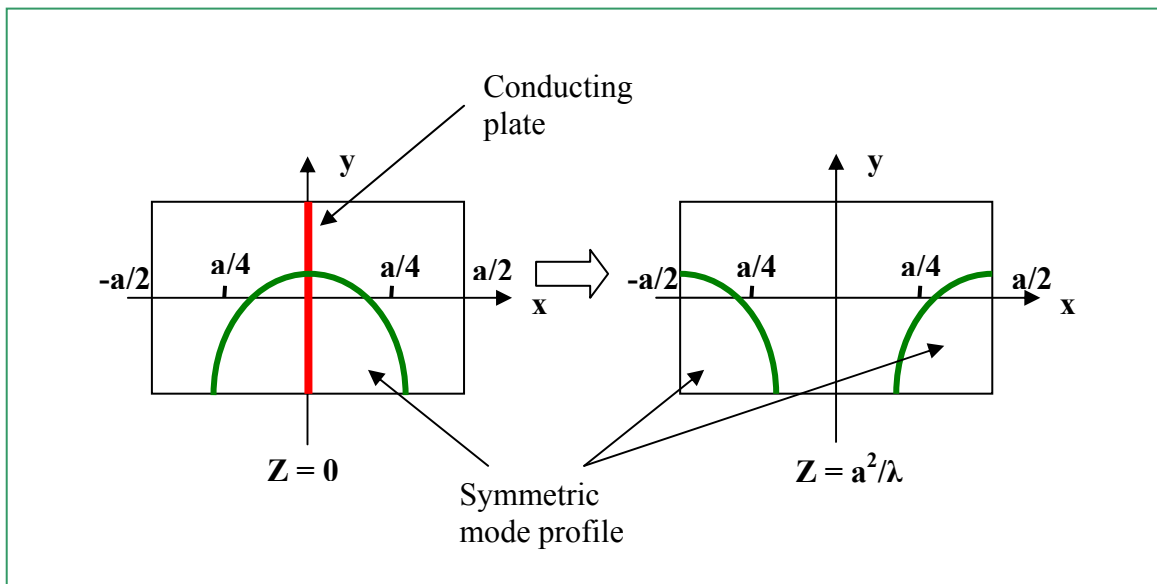


Fig. 2.2 Illustration of a symmetric mode splitting at $z = a^2/\lambda$.

Thus, we can consider each side of the split waveguide independently with its corresponding half-initial field distribution. Now we can consider for each part the flip imaging effect as described above (Eq. (2.14)) with $a' = \frac{a}{2}$. A reversed (mirror) image will be created on each side (see Fig. 2.2) at distance

$$L_s = \frac{4a'^2}{\lambda} = \frac{4a^2}{4\lambda} = \frac{a^2}{\lambda} \quad (2.16)$$

If the initial field distribution at the entrance to the rectangular waveguide is narrower than its width (see Fig. 2.2), then the mirrored imaging of each half-waveguide independently will seem like splitting of the initial picture.

2.4 Curved Parallel Plates waveguide. Ohmic and diffraction losses

The main waveguide section of the resonator is made of two curved parallel plates with a curvature R , at a distance b from each other. The geometric relation that holds for the CPP waveguide section may be written as

$$x^2 + \left[y \pm \left(R - \frac{b}{2} \right) \right]^2 \leq R^2 \quad (2.17)$$

which is depicted in Fig.2.3:

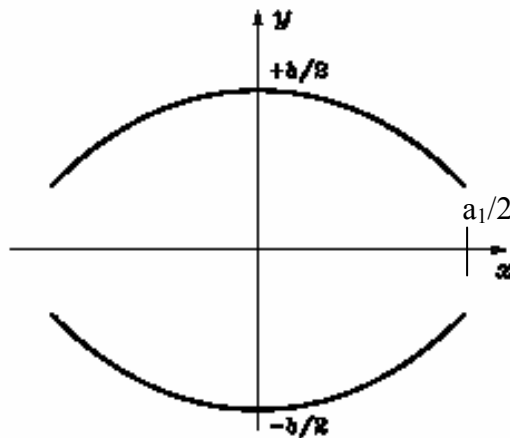


Fig.2.3 Curved plates geometry: $R=15.875\text{mm}$; $b=10.7\text{mm}$; $a_1=22\text{mm}$;

The model used in the analysis of this CPP waveguide is following I.Yakover [12]. It assumed that the fundamental mode TE_{01}^{CPP} could be described by a relatively simple expressions:

$$\mathbf{E}_{01}^{CPP}(x, y) = U_0^{CPP} e^{\frac{-x^2}{w_0^2}} \cos\left(\frac{\pi}{b} y\right) \hat{\mathbf{x}} \quad (2.18)$$

$$\mathbf{H}_{01}^{CPP}(x, y) = \frac{U_0^{CPP}}{Z_{CPP}} e^{\frac{-x^2}{w_0^2}} \cos\left(\frac{\pi}{b} y\right) \hat{\mathbf{y}}$$

where U_0^{CPP} is an amplitude, w_0 is the Gaussian beam waist parameter and Z_{CPP} is an impedance. If we define:

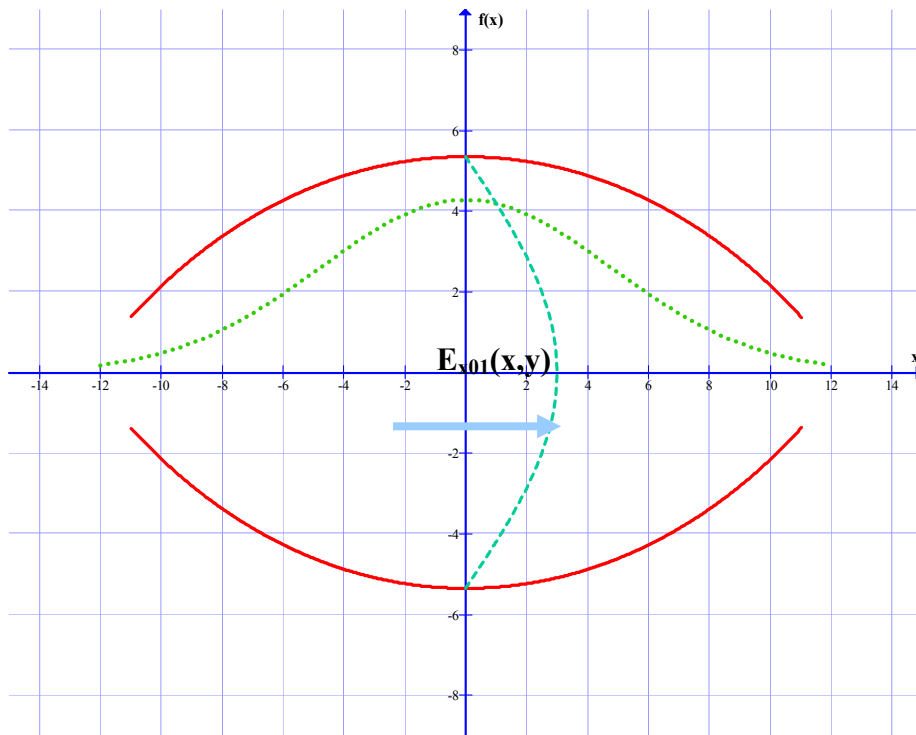
$$\bar{R} = \sqrt{2Rb - b^2} \quad (2.19)$$

the cut-off wave number K_{co}^{CPP} and the Gaussian beam waist parameter w_0 are [12]:

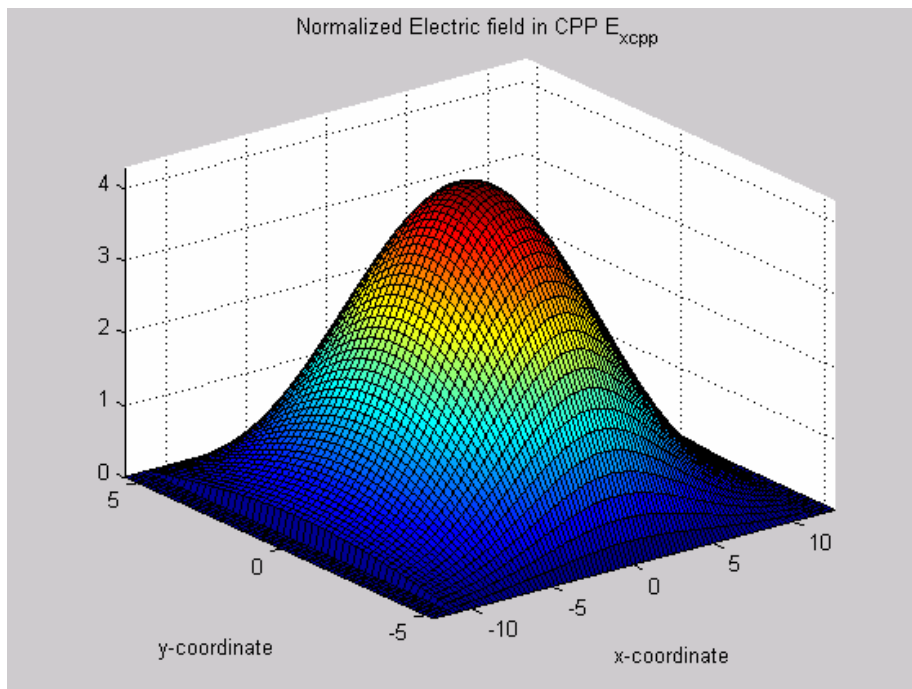
$$K_{co}^{cpp} = \frac{\pi + \arctg \frac{b}{\bar{R}}}{b} = 0.35 \text{mm}^{-1} \quad (2.20)$$

$$w_0 = \sqrt{\frac{\bar{R}}{k_{co}^{cpp}}} = 6.53 \text{mm}$$

The corresponding field profile $E(x,y)$ at the CPP aperture is shown in the following figure:



(a)



(b)

Fig.2.4 Electric field profile in CPP: (a) cross-section view; (b) 3D view.

The following table gives additional information about the CPP geometry and the CPP propagation mode TE_{01}^{CPP} :

CPP waveguide length L_{CPP} , (mm)	890
Curvature radius R, (mm)	15.875
Cross section area A_{cpp} , (mm^2)	174.56
Volume of waveguide V_{cpp} , (cm^3)	~ 155
Internal walls surface area S_{cpp} , (cm^2)	432.61
Wide dimension of CPP waveguide a_1 , (mm)	22
Distance between parallel plates b, mm	10.7
Parameter w_0 , (mm)	6,53
Cut-off wave number, (mm^{-1})	0.35

Tab.2.2 Geometry of the CPP waveguide and its fundamental mode propagation parameters.

A different approach based on paper [13] was described by Y.Lurie [14]. In this more precise model, the modal structure of CPP waveguide is represented by a set of Gauss-Hermit modes. Mr. A.Anaton and Mr. O.Markish, (two undergraduate students of Tel-Aviv University), utilized Lurie's model as part of their graduation project. A description and a full list of the Gauss-Hermit modes for our CPP waveguide are given in [18]. Assuming that only the fundamental mode TE_{01}^{CPP} propagates we get:

$$\tilde{H}_x^h = -jD^{cpp} \frac{\beta_{01}}{K_{c,01}^2} \frac{\exp\left(\frac{-\delta_{01}^2 x^2}{1+\alpha^2 y^2}\right)}{(1+\alpha^2 y^2)^{1/4}} \left[\frac{-2\delta_{01}^2 x}{(1+\alpha^2 y^2)^2} \sin(\varphi_{01}) + \frac{\alpha^2 x K_{c,01} y}{1+\alpha^2 y^2} \cos(\varphi_{01}) \right]$$

$$\tilde{E}_y^h = \frac{-\omega\mu}{\beta_{01}} \tilde{H}_x^h$$

$$\tilde{H}_y^h = -jD^{cpp} \frac{\beta_{01}}{K_{c,01}^2} \frac{\exp\left(\frac{-\delta_{01}^2 x^2}{1+\alpha^2 y^2}\right)}{(1+\alpha^2 y^2)^{1/4}} * \left[\frac{\alpha^2 y}{2} \frac{4\delta_{01}^2 - \alpha^2 y^2 - 1}{(1+\alpha^2 y^2)^2} \sin(\varphi_{01}) + \left(K_{c,01} \left[1 + \frac{\alpha^2 x^2}{1+\alpha^2 y^2} \left(1 - \frac{2\alpha^2 y^2}{1+\alpha^2 y^2} \right) \right] - \frac{\alpha}{2(1+\alpha^2 y^2)} \right) \cos(\varphi_{01}) \right] \quad (2.21)$$

$$\tilde{E}_x^h = \frac{\omega\mu}{\beta_{01}} \tilde{H}_y^h$$

where

$$\alpha = \frac{2}{\sqrt{2Rb - b^2}},$$

$$\beta_{01} = \sqrt{(\omega/c)^2 - K_{c,01}^2},$$

$$\delta_{01} = \sqrt{(\alpha K_{c,01})/2},$$

$$K_{c,01} = \frac{1}{b} * [\pi + \arctg(\alpha b/2)],$$

$$\varphi_{01} = K_{c,01} y * \left[1 + \frac{\alpha^2 y^2}{2 * (1 + \alpha^2 y^2)} \right] - 1/2 * \arctg(\alpha y). \quad (2.22)$$

The coefficient D^{cpp} is the amplitude of the fields normalized to carry 1 Watt of the total power:

$$P_{in}^{CPP} = \frac{1}{2} \text{Re} \left\{ \iint (\tilde{\mathbf{E}}_x^h \tilde{\mathbf{H}}_y^{h*} - \tilde{\mathbf{E}}_y^h \tilde{\mathbf{H}}_x^{h*}) dx dy \right\} = 1 \quad (2.23)$$

We have considered both \hat{x} and \hat{y} components of the electric field \mathbf{E}_{01}^{CPP} as well as corresponding of magnetic field components. The electric field profile $\mathbf{E}_{01}^{CPP}(x,y)$ of the fundamental Gauss-Hermit mode is shown in Fig.2.5 (compare with Fig.2.4):

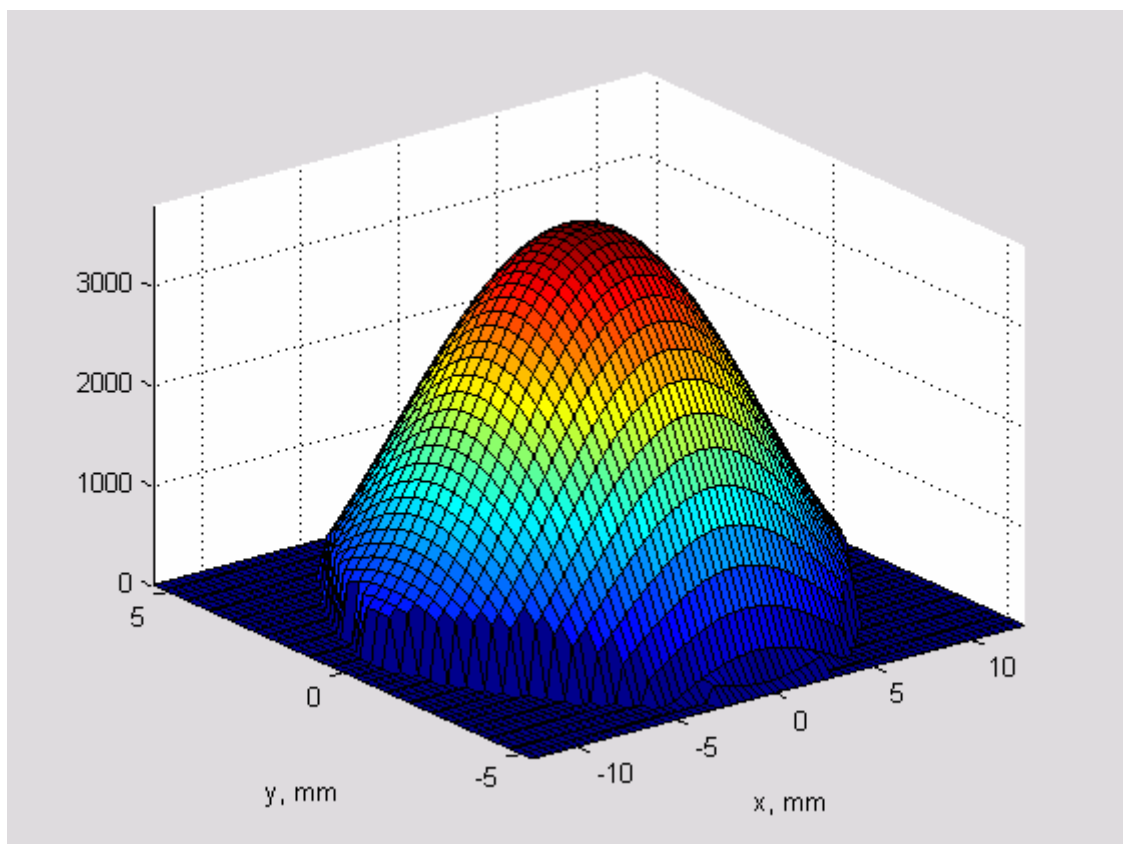


Fig.2.5 Electric field distribution in CPP waveguide.

Propagating electromagnetic waves in a CPP waveguide decay with distance due to finite conductivity σ of the copper waveguide walls. Furthermore, because at points $(a_1/2;0)$ and $(-a_1/2;0)$ (see Fig.2.4) the cavity is open, a small part of energy leaks out through the gap between the resonator plates.

Ohmic losses

The ohmic losses per unit length in the CPP waveguide walls may be found from the follow general expression [2]:

$$P_l = \frac{R_s}{2} \oint_l |H_{\parallel}|^2 dl \quad (2.24)$$

Here H_{\parallel} is the tangential magnetic field near the walls and R_s is the real part of the wall's surface impedance given by

$$Z_s = \frac{1+j}{\sigma\delta_s} = (1+j)R_s \quad (2.25)$$

where δ_s is a skin depth.

A detailed description and calculation of the tangential magnetic field at the curved walls for the Gauss-Hermit model may be found in [18]. Assuming the case of the small losses, the total ohmic losses can be given by multiplication of waveguide length L_{cpp} by the dP/dz since the last is a constant at any z in the CPP walls.

The result of calculation is:

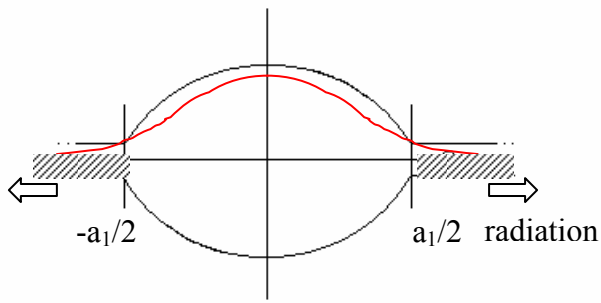
$$P_{wall}^{GH} = \frac{dP_{loss}}{dz} L_{cpp} * 100\% = 0.014 * 0.89 * 100 = 1.25\%$$

after one pass for the Gauss-Hermit model, and

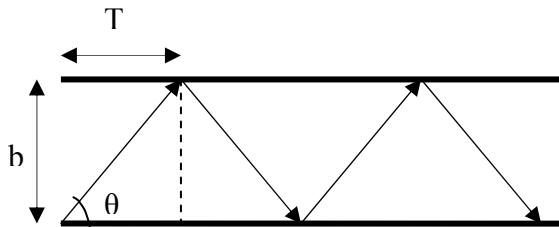
$$P_{wall}^G = \frac{dP_{loss}}{dz} L_{cpp} * 100\% = 0.001 * 0.89 * 100 \approx 0.09\%$$

for the Gaussian approximation model.

Diffraction losses



(a)



(b)

Fig.2.6 Explanation for the diffraction losses calculation: a) cross-section view; b) zigzag propagation.

To estimate the diffraction losses between the curved plates we use a zigzag ray propagation of the waveguide mode. We assume that on each incidence of the ray on a plate a power fraction (2.26) is lost.

$$\delta P_{diff} = 2 \frac{\int_{a_1/2}^{\infty} |E_x|^2 dx}{\int_{-\infty}^{\infty} |E_x|^2 dx} \quad (2.26)$$

Equation (2.26) follows from the geometry of the curved plates and (see Fig.2.6(a)) equals to the ratio of the “out-of-plates tails” power and the total power of the CPP energy distribution. Thus, the total diffraction losses are $P_{diff} = \delta P_{diff} N$, where N is the number of “zigzag” reflections of the ray along the waveguide (see Fig. 2.6(b)):

$$N = \frac{L_{cpp}}{T} = \frac{L_{cpp} * tg\left(\frac{K_{c,01}}{K_z}\right)}{b} \quad (2.27)$$

The relation between the different wave numbers is explained in the following diagram:

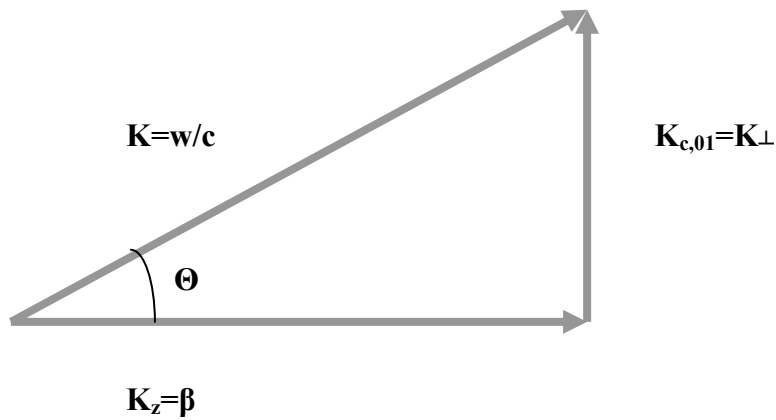


Fig.2.7 Longitudinal and transversal wave numbers

Calculation of Eq.(2.26) gives 0.064% of diffraction loss in one-way trip along the waveguide for the Gauss-Hermit distribution. The Gaussian approximation gives a 0.05% diffraction loss.

The total round-trip losses in the CPP waveguide are therefore the sum of the diffraction (radiation) losses and the ohmic losses in the walls. The results are ~1.25% for the Gauss-Hermit representations and ~0.1% for the Gaussian approximation model. These losses could be neglected in further considerations.

2.5 Transition from CPP to rectangular waveguides

The fields in the rectangular waveguide (see Fig. 2.8) can be described by the complete set of TE and TM eigenmodes [2] (apart from the factor $e^{-j\beta_{mn}z}$):

TE modes

$$\tilde{\mathbf{h}}_{z,mn}^h = D_{mn}^h \cos\left(\frac{m\pi}{a}\left(x + \frac{a}{2}\right)\right) \cos\left(\frac{n\pi}{b}\left(y + \frac{b}{2}\right)\right)$$

$$\tilde{\mathbf{h}}_{x,mn}^h = jD_{mn}^h \frac{\beta_{mn}}{K_{c,mn}^2} \frac{m\pi}{a} \sin\left(\frac{m\pi}{a}\left(x + \frac{a}{2}\right)\right) \cos\left(\frac{n\pi}{b}\left(y + \frac{b}{2}\right)\right) \quad (2.28)$$

$$\tilde{\mathbf{h}}_{y,mn}^h = jD_{mn}^h \frac{\beta_{mn}}{K_{c,mn}^2} \frac{n\pi}{b} \cos\left(\frac{m\pi}{a}\left(x + \frac{a}{2}\right)\right) \sin\left(\frac{n\pi}{b}\left(y + \frac{b}{2}\right)\right)$$

$$\tilde{\mathbf{e}}_{x,mn}^h = \frac{k_0 Z_0}{\beta_{mn}} \tilde{\mathbf{h}}_{y,mn}^h$$

$$\tilde{\mathbf{e}}_{y,mn}^h = -\frac{k_0 Z_0}{\beta_{mn}} \tilde{\mathbf{h}}_{x,mn}^h$$

$$Z_0 = 120\pi \text{ } [\Omega]$$

TM modes

$$\begin{aligned}\tilde{\mathbf{e}}_{z,mn}^e &= D_{mn}^e \sin\left(\frac{m\pi}{a}\left(x + \frac{a}{2}\right)\right) \sin\left(\frac{n\pi}{b}\left(y + \frac{b}{2}\right)\right) \\ \tilde{\mathbf{e}}_{x,mn}^e &= -jD_{mn}^e \frac{\beta_{mn}}{K_{c,mn}^2} \frac{m\pi}{a} \cos\left(\frac{m\pi}{a}\left(x + \frac{a}{2}\right)\right) \sin\left(\frac{n\pi}{b}\left(y + \frac{b}{2}\right)\right) \\ \tilde{\mathbf{e}}_{y,mn}^e &= -jD_{mn}^e \frac{\beta_{mn}}{K_{c,mn}^2} \frac{n\pi}{b} \sin\left(\frac{m\pi}{a}\left(x + \frac{a}{2}\right)\right) \cos\left(\frac{n\pi}{b}\left(y + \frac{b}{2}\right)\right)\end{aligned}\tag{2.29}$$

$$\tilde{\mathbf{h}}_{x,mn}^e = -\frac{k_0}{\beta_{mn} Z_0} \tilde{\mathbf{e}}_{y,mn}^e$$

$$\tilde{\mathbf{h}}_{y,mn}^e = \frac{k_0}{\beta_{mn} Z_0} \tilde{\mathbf{e}}_{x,mn}^e$$

$$Z_0 = 120\pi [\Omega]$$

The D_{mn} coefficients are determined from the normalization of the modes to 1W of power:

$$P_{mn}^p = \frac{1}{2} \operatorname{Re} \left\{ \iint (\tilde{\mathbf{e}}_{x,mn}^p \tilde{\mathbf{h}}_{y,mn}^{p*} - \tilde{\mathbf{e}}_{y,mn}^p \tilde{\mathbf{h}}_{x,mn}^{p*}) dx dy \right\} = 1\tag{2.30}$$

where index p refers to h (for TE-mode) or e (for TM-mode).

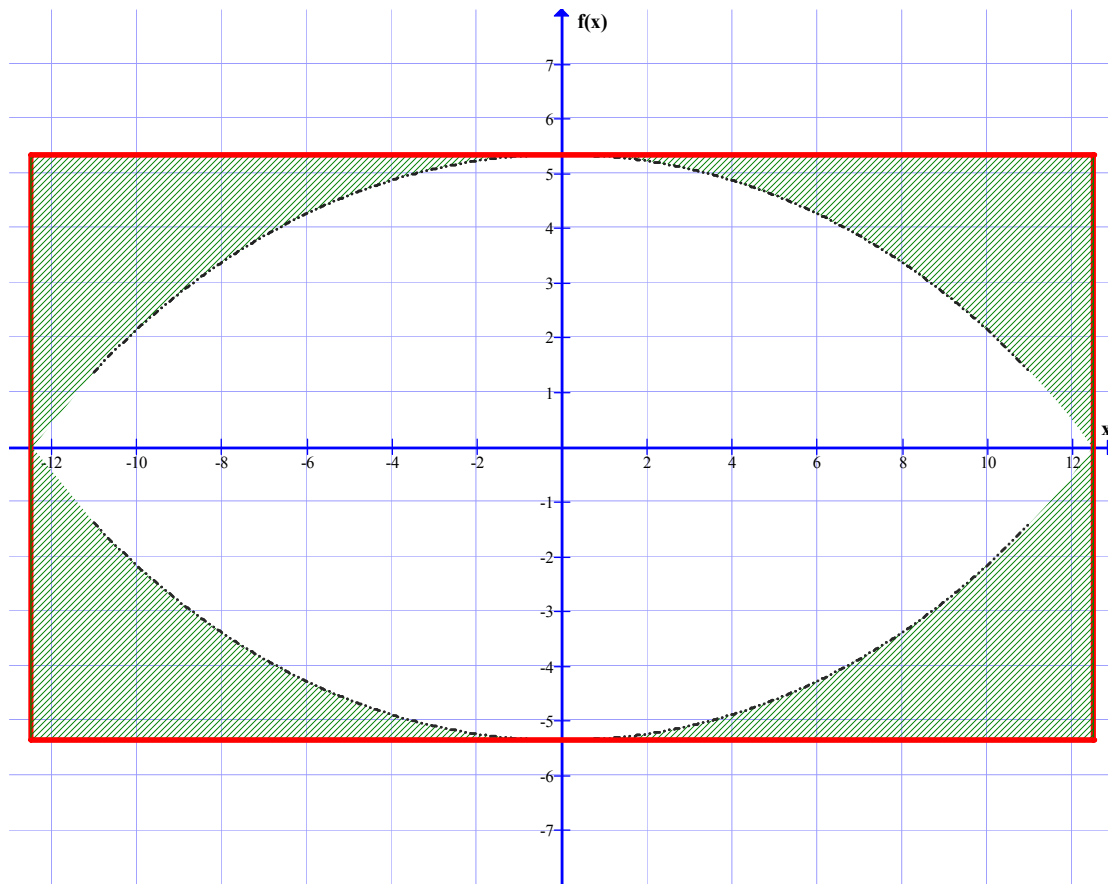


Fig. 2.8 Profiles mismatch at the CPP-rectangular waveguide junction.

The integrals in (2.30) can be solved analytically and the normalization coefficients for the TE and TM modes are:

$$D_{mn}^h = \sqrt{\frac{2\varepsilon_{0m}\varepsilon_{0n}}{ab} \left(\frac{K_{co,mn}}{\beta_{mn}} \right)^2} \frac{\omega\mu}{\beta_{mn}}$$

$$D_{mn}^e = \sqrt{\frac{2\varepsilon_{0m}\varepsilon_{0n}}{ab} \left(\frac{K_{co,mn}}{\beta_{mn}} \right)^2} \frac{\beta_{mn}}{\omega\varepsilon} \quad (2.31)$$

where $\varepsilon_{0m} = \begin{cases} 1, & \text{if } m=0 \\ 2, & \text{else} \end{cases}$.

In general, the problem of excitation of a waveguide through an aperture can be solved by “full mode-matching” technique. The solution is found from equations of continuity of the transverse electric and magnetic fields, taking into account both forward and backward waves at the excitation plane. In our problem – for our operation frequency, both waveguides are overmoded, and we can use the qiasi-optical approximation. In the CPP waveguide we assume a single incident (TE_{01}) propagation mode and neglect backward reflection of the mode or any excitation of reflected higher order modes from the interface of the two apertures (geometry of the interface apertures mismatch is shown in the Fig. 2.8). It means that the entire energy of the incident wave TE_{01}^{CPP} mode is redistributed among all the rectangular waveguide modes, which are excited in the splitter. We will calculate the amplitude of each of the excited mode, which is proportional to its field overlap with the exciting input wave and will confirm that the energy conservation law holds for this transition.

The continuity equations for both the x and y components of the electric fields at the interface plane are:

$$\mathbf{E}^{CPP}(x, y, 0^-) = \mathbf{E}_{01}^{h, CPP} = \mathbf{E}_{tot}^{rec}(x, y, 0^+) = \mathbf{E}^h(x, y, 0^+) + \mathbf{E}^e(x, y, 0^+)$$

for TE modes:

$$\mathbf{E}^h(x, y, 0^+) = \sum_m \sum_n (A_{mn}^h \tilde{\mathbf{e}}_{x, mn}^h \hat{\mathbf{x}} + A_{mn}^h \tilde{\mathbf{e}}_{y, mn}^h \hat{\mathbf{y}}) \quad (2.32)$$

for TM modes:

$$\mathbf{E}^e(x, y, 0^+) = \sum_m \sum_n (A_{mn}^e \tilde{\mathbf{e}}_{x, mn}^e \hat{\mathbf{x}} + A_{mn}^e \tilde{\mathbf{e}}_{y, mn}^e \hat{\mathbf{y}})$$

We can cross multiply the electric field at the both sides of the junction plane $z=0$ by the vector $\tilde{\mathbf{h}}_{m'n'}^*$ and calculate the power at both sides by taking the

integral of the result over the intersection aperture. We will also define the normalization power of the mode as:

$$P_{mn}^{norm} = \frac{1}{2} \iint (\tilde{\mathbf{e}}_{mn}^p \times \tilde{\mathbf{h}}_{mn}^{*p}) \hat{\mathbf{z}} dx dy = 1W \quad (2.33)$$

Thus, we will get, using the orthogonality condition

$$\iint (\mathbf{e}_{mn}^p \times \mathbf{h}_{m'n'}^{*p}) \hat{\mathbf{z}} dx dy = \begin{cases} 1, & \text{if } m,n = m',n' \\ 0, & \text{else} \end{cases} \quad (2.34)$$

for the TE or TM modes respectively:

$$\frac{1}{2} \left\{ \iint (E_x^{cpp} \tilde{h}_{y,mn}^{*p} - \tilde{E}_y^{cpp} \tilde{h}_{x,mn}^{*p}) dx dy \right\} = P_{mn}^{norm,p} A_{mn}^p \quad (2.35)$$

The amplitude of the mn mode excitation is given, therefore, in terms of the overlap integral:

$$A_{mn}^p = \frac{\iint (E_x^{cpp} \tilde{h}_{y,mn}^{*p} - \tilde{E}_y^{cpp} \tilde{h}_{x,mn}^{*p}) dx dy}{\iint (\tilde{\mathbf{e}}_{mn}^p \times \tilde{\mathbf{h}}_{mn}^p) \hat{\mathbf{z}} dx dy} \quad (2.36)$$

From the energy conservation law using the normalization procedure, we should also accept:

$$P_{in} = P_{out} = \sum_m \sum_n \left| A_{mn}^{TE} \right|^2 + \left| A_{mn}^{TM} \right|^2 = 1W \quad (2.37)$$

In the Gaussian approximation model, we get simpler expressions. Since there is only x -component in the exciting electric field (Eq.2.18), and the curvature of the plates (Fig. 2.8) is neglected, it is found [12], [16] that only x -component of the electric field $E_x \hat{\mathbf{x}}$ and y -component of the magnetic field $H_y \hat{\mathbf{y}}$ will present in the excited fields of the Talbot rectangular waveguide. Furthermore, due to continuity in the $\hat{\mathbf{y}} - \hat{\mathbf{z}}$ plane, the CPP fundamental mode (Eq.2.18) will excite on by modes with index $n=1$. Finally, due to symmetry of the problem, the amplitudes of the rectangular waveguide modes will vanish for all odd m . Thus, the modes that will be excited and propagate in the rectangular splitter are:

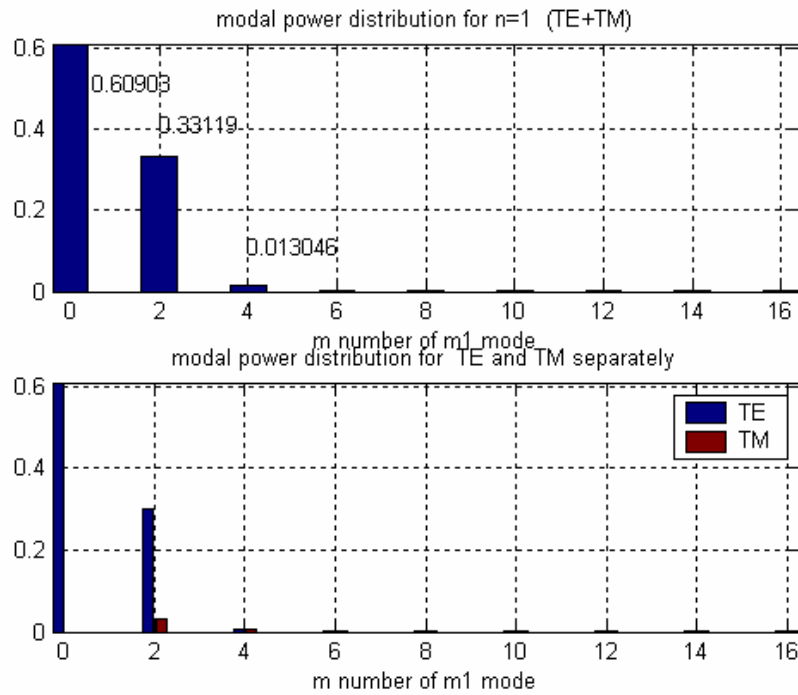
$$\begin{aligned} \mathbf{E}(x,y) &= \sum_{m1} \left(A_{m1}^h \tilde{e}_{x,m1}^h + A_{m1}^e \tilde{e}_{x,m1}^e \right) e^{-j\beta_{m1}z} \hat{\mathbf{x}} \\ \mathbf{H}(x,y) &= \sum_{m1} \left(\frac{1}{Z_{m1}^h} A_{m1}^h \tilde{h}_{y,m1}^h + \frac{1}{Z_{m1}^e} A_{m1}^e \tilde{h}_{y,m1}^e \right) e^{-j\beta_{m1}z} \hat{\mathbf{y}} \end{aligned} \quad (2.38)$$

$$m = 0, 2, 4 \dots \text{even}$$

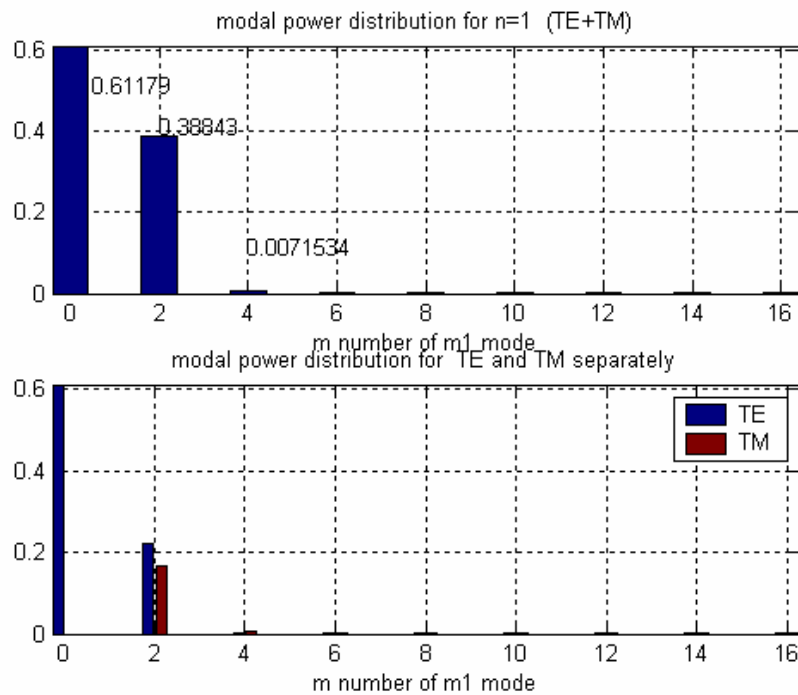
here Z_{m1}^h and Z_{m1}^e are wave impedances of the modes.

Note that this is correct only in the Gaussian approximation. In the Gauss-Hermit model, y -component of the electric field, x -component of the magnetic field and higher order modes are excited too.

The power distribution to each rectangular mode as part of the total excited field power (1W) is shown in the following diagrams:



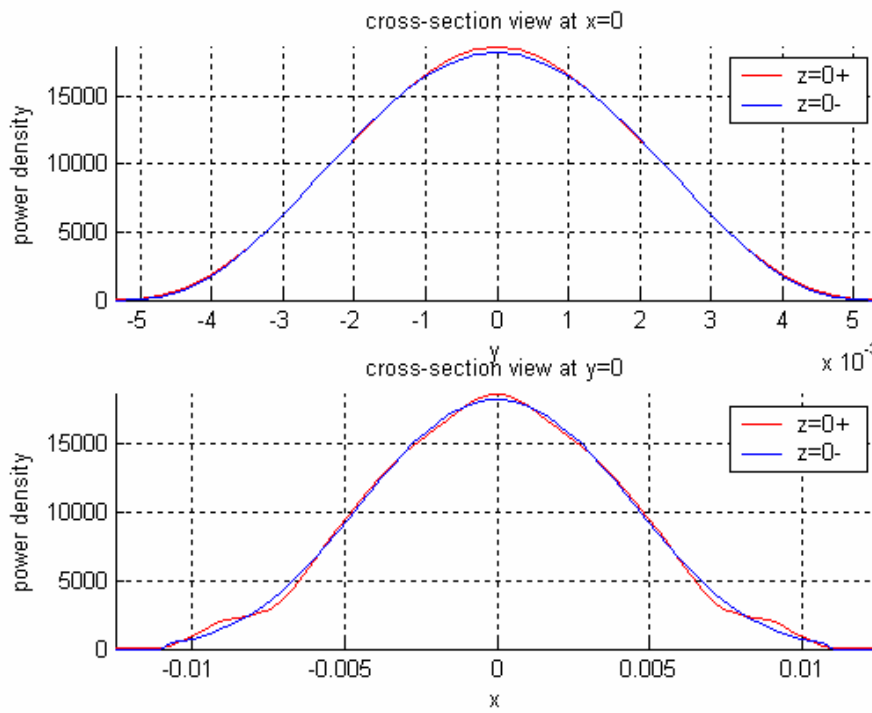
(a)



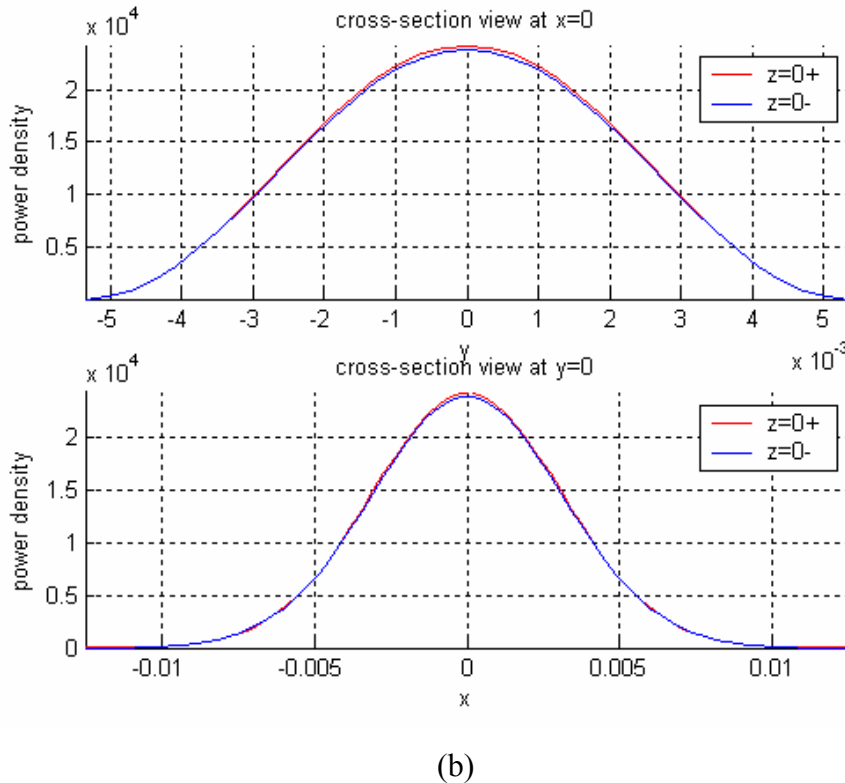
(b)

Fig. 2.9 Weight distribution of excited modes in rectangular waveguide: (a) Gauss-Hermit model; (b) Gaussian approximation.

Comparison of the main cross-section profiles of power flow density at both sides of the junction provides proves of the adequacy of the approximation for the two models:



(a)



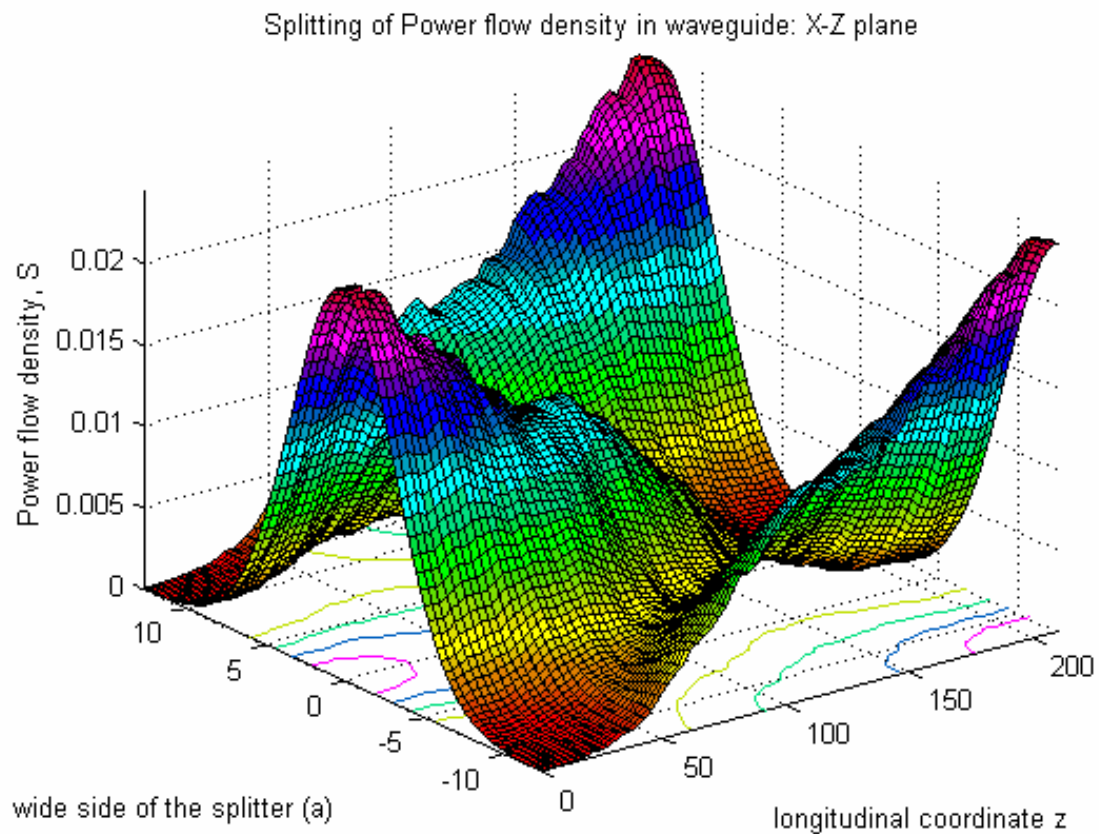
(b)
Fig. 2.10 Comparison of the main cross-section profiles (a) Gauss-Hermit model; (b) Gaussian approximation

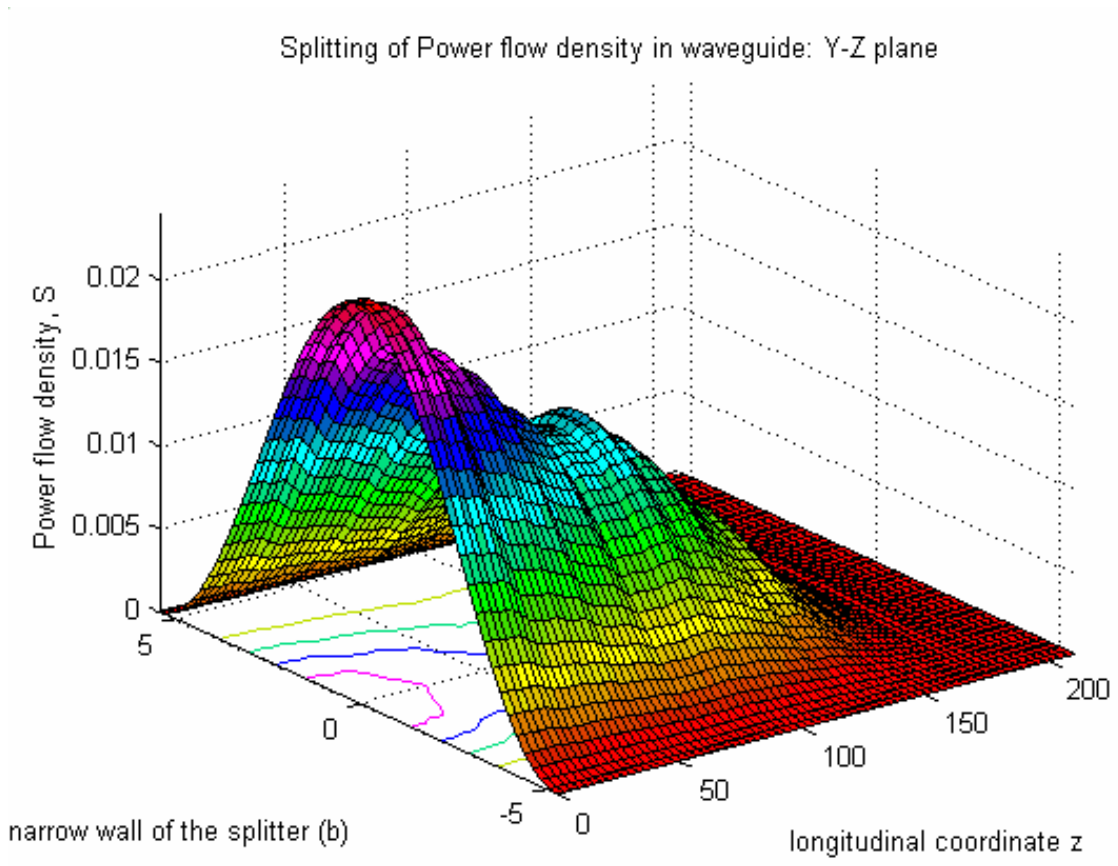
2.6 Propagation in an overmoded rectangular waveguide (splitter). Ohmic and diffraction losses

There is a particular field distribution in the splitter input, which can be described as a sum of a number of rectangular waveguide modes. The wave propagates through the splitter up to the perforated short at the half Talbot length plane $z = 210$ mm. Initially the maximum of field (and power flow density) distribution is located at the center of the splitter. All fields, are negligible near the sidewalls. As the wave propagates toward the splitter, the electromagnetic field splits along the x -coordinate plane while in the y direction the distribution does not change (assuming that only the

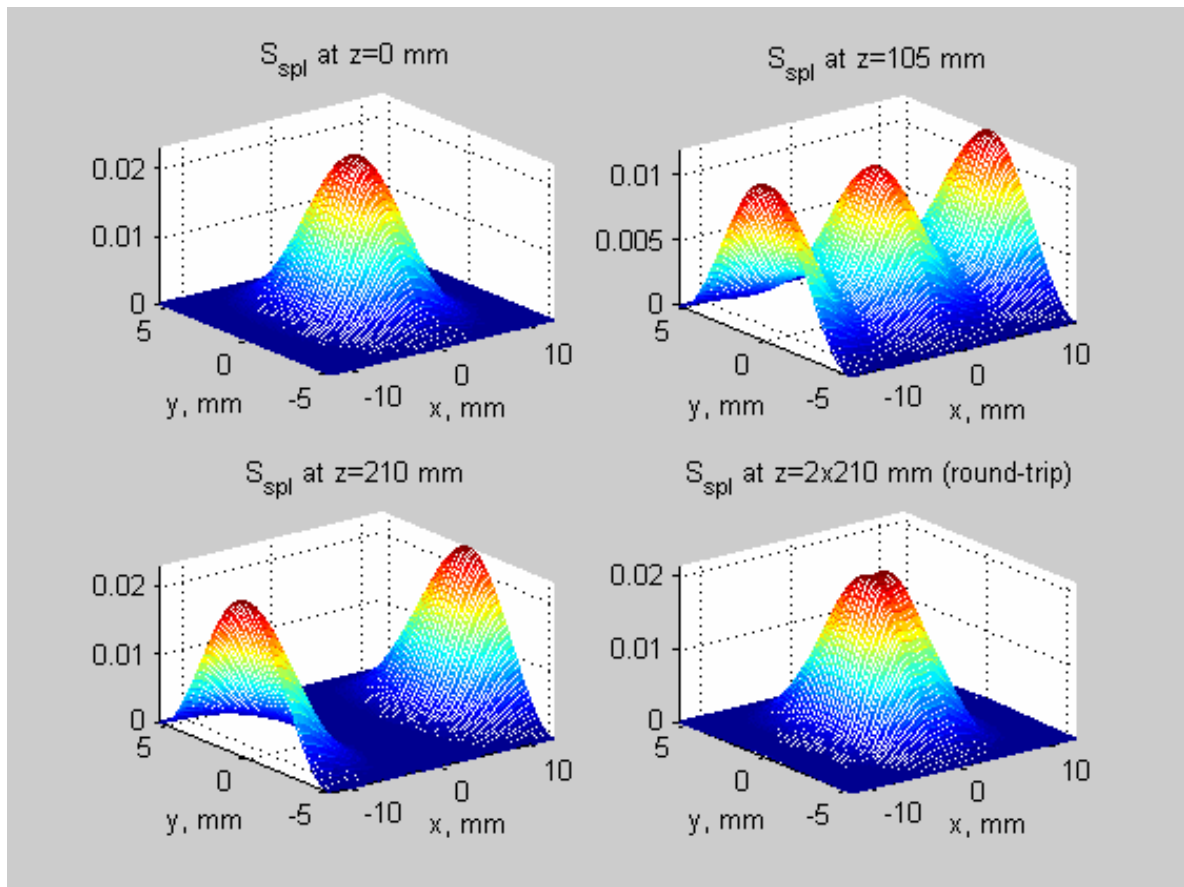
$n=1$ modes are excited). As a result, electromagnetic energy of the propagating waves increases near the sidewalls (narrow b-dimension) of the rectangular waveguide and becomes maximal near the b-walls at the plane of the perforated mirror. Hence, we can expect extremely small ohmic losses right after the CPP-rectangular junction ($z=0$ mm) and maximal loss near the end of the splitter (at $z=210$ mm) where a maximal tangential component of the magnetic field is generated

. The following 3-D plots illustrate the effect of fields splitting:





(b)



(c)

Fig. 2.11 Power density flow propagation: (a) X-Z dependence in $y = 0$ plane; (b) Y-Z dependence in $x = 0$ plane; (c) power flow density distribution (x, y dependence) at different distances along the Talbot rectangular waveguide: $z=0$ – input, $z=105\text{mm}$ – starting to split, $z=210\text{mm}$ – full splitting, $z=420$ – imaging.

The power density plots shown in the Fig.2.11 a) and b) were calculated from the calculated field distributions according to:

$$S = \frac{1}{2} \Re e \left(\sum_{m1} \mathbf{E}_{m1} \times \sum_{m1} \mathbf{H}_{m1}^* \right) \quad (2.39)$$

All plots shown were calculated with the Gaussian approximation model in order to illustrate the fields splitting effect. For the more accurate Gauss-Hermit model, the corresponding plots look very similar.

Wall losses

In a single mode waveguide or, when a single mode propagates in an overmoded waveguide, the power loss into the walls per unit length is found from (2.24):

$$P_{l,mn} = \frac{R_s}{2} \oint_L |\hat{\mathbf{n}} \times \bar{\mathbf{H}}_{mn}|^2 dl \quad (2.40)$$

Assuming small losses, the mode would propagate as in a lossless waveguide, but with slowly varying amplitude

$$\{\bar{\mathbf{E}}, \bar{\mathbf{H}}\}_{mn} = A_{mn}(z) \{\hat{\mathbf{e}}_{mn}(x, y), \hat{\mathbf{h}}_{mn}(x, y)\} e^{-j\beta_{mn}z} \quad (2.41)$$

The fast varying coefficient ($e^{-j\beta_{mn}z}$) cancels out in the absolute value operation in (2.40). By conservation of energy, the power loss rate to the walls is equal to the power attenuation rate of the mode:

$$P_{l,mn} = -\frac{dP_{mn}}{dz} = \frac{R_s}{2} |A_{mn}(z)|^2 \oint_L |\hat{\mathbf{n}} \times \hat{\mathbf{h}}_{mn}|^2 dl \quad (2.42)$$

Since $|A_{mn}|^2$ is proportional to the mode power, we can write:

$$-\frac{dP_{mn}}{dz} = \alpha_{mn} P_{mn}(z) = P_{l,mn} \quad (2.43)$$

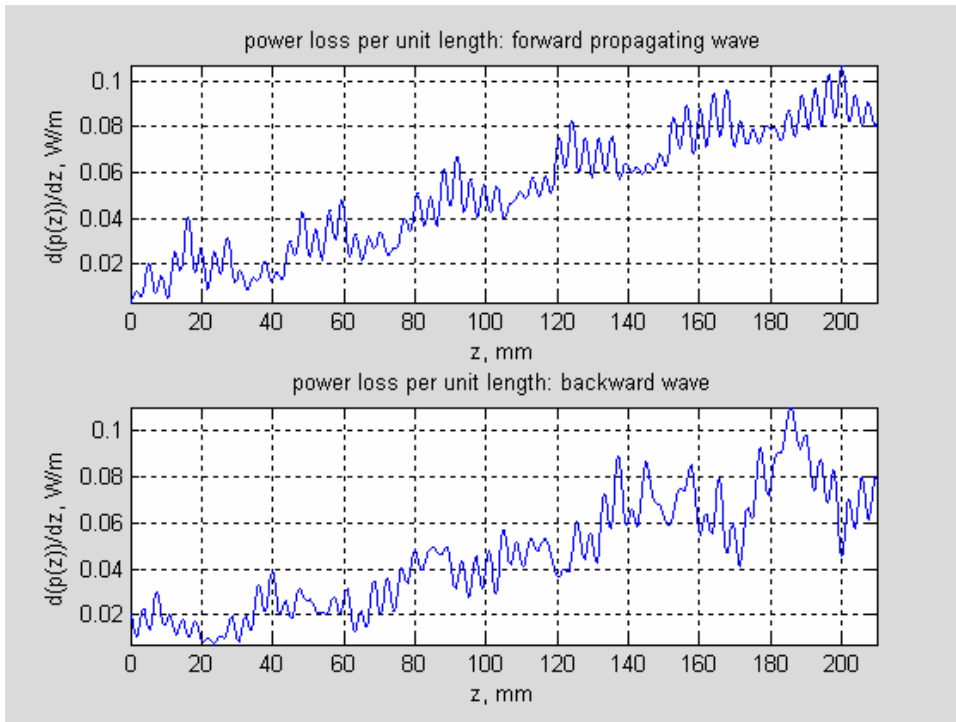
where α_{mn} is the power attenuation constant of the mode mn which apparently attenuates exponentially.

In the case when a number of modes propagate in the waveguide, the simple mode constant attenuation rate derivation does not apply. When, substituting (2.41) in (2.40):

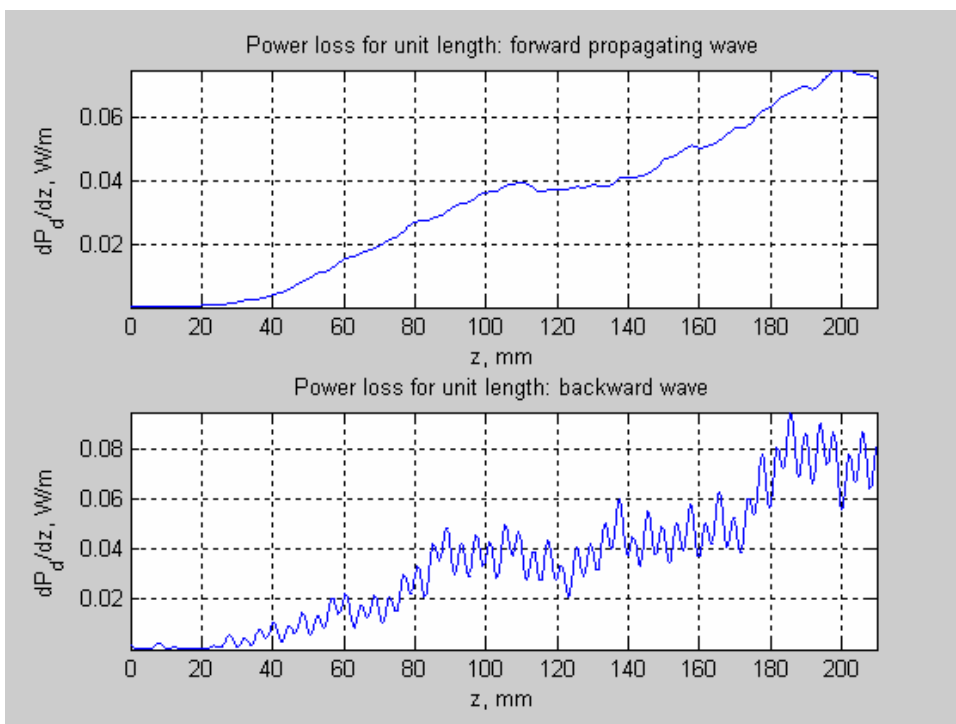
$$P_l(z) = -\frac{dP_{tot}(z)}{dz} = \frac{R_S}{2} \oint_{cs} \left| n \times \sum_{mn} H_{mn} \right|^2 dl = \frac{R_S}{2} \oint_{cs} \left| \sum_{mn} H_{\parallel mn} \right|^2 dl = \frac{R_S}{2} \oint_{cs} \left| \sum_{mn} A_{mn} \hat{\mathbf{h}}_{mn}(x, y) e^{-j\beta_{mn}z} \right|^2 [W / m] \quad (2.44)$$

where the integral is taken along the perimeter of the waveguide cross section (cs). In this case, the ohmic losses per unit waveguide length become a function of the coordinate z and not constant even in a small losses approximation. The $e^{-j\beta_{mn}z}$ factors do not cancel out and the interference between the modes causes z dependent attenuation rate of the total power.

The power losses per unit length as a function of the coordinate z and the total ohmic losses as a function of z shown in the following plots:



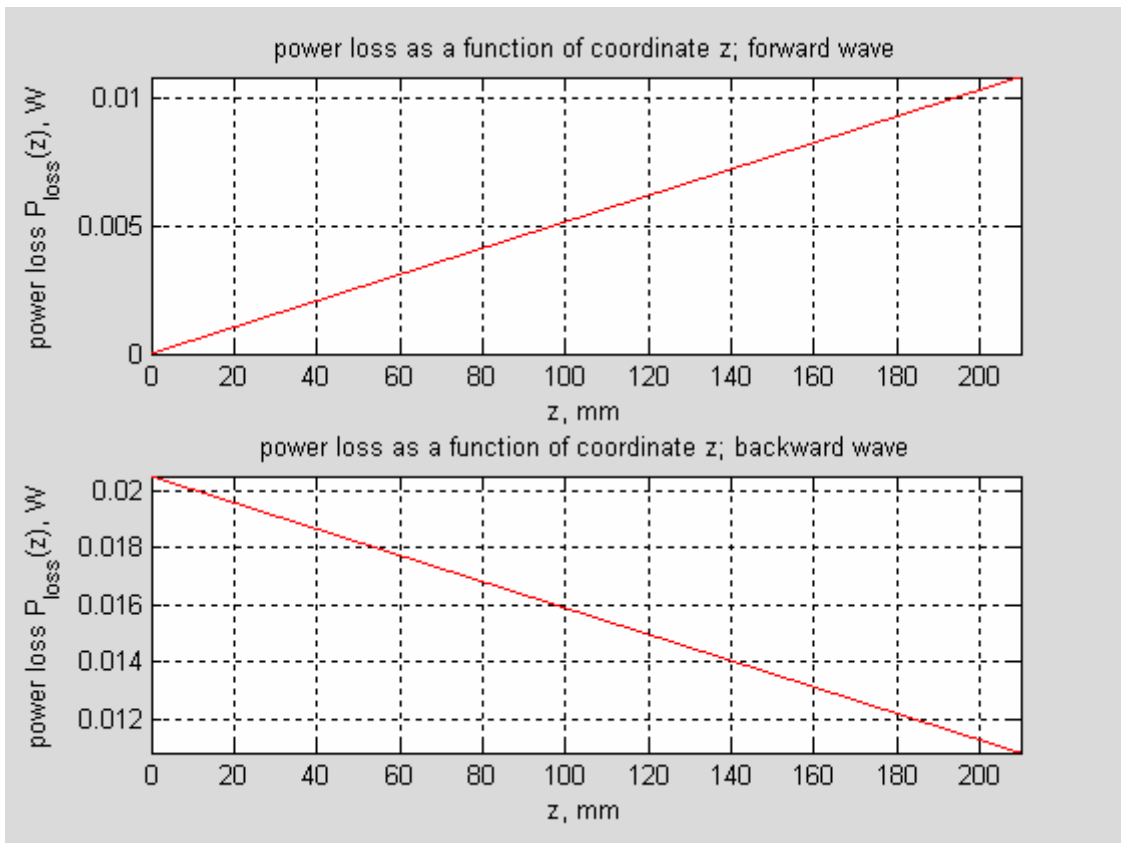
(a)



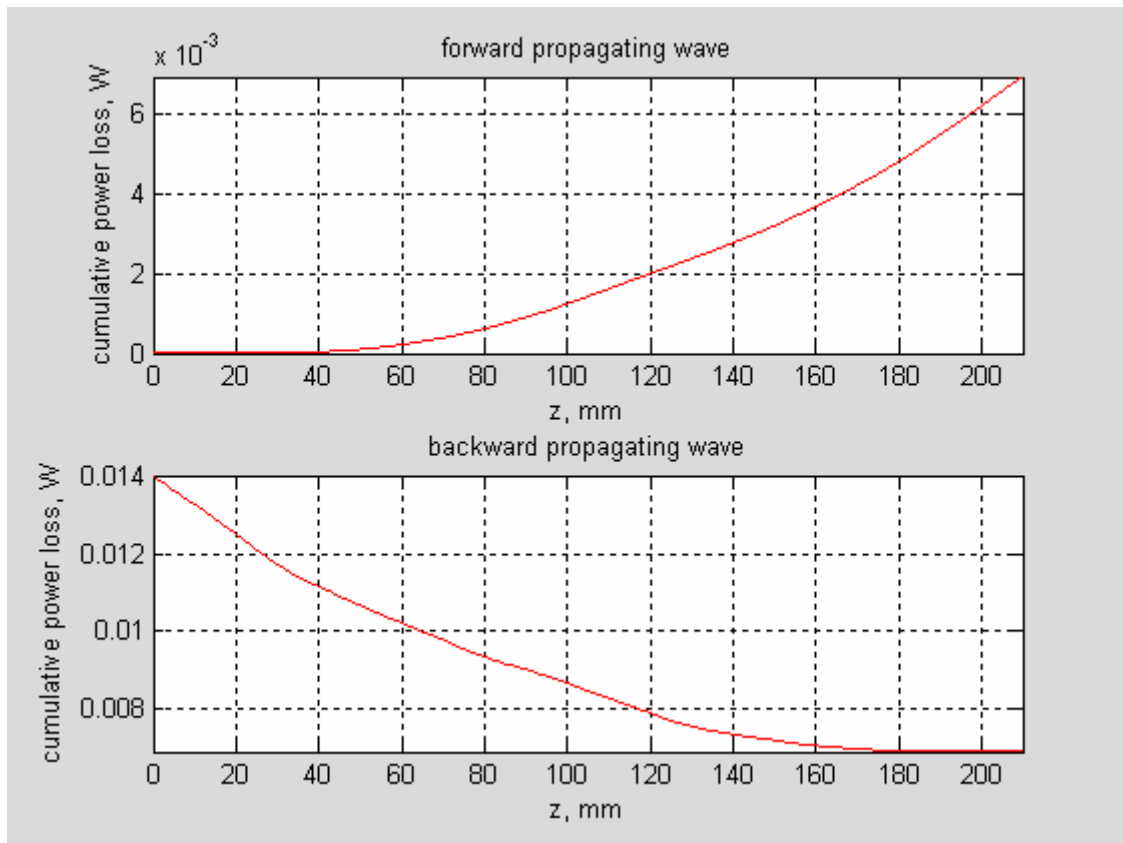
(b)

Fig.2.12 Power losses per unit length. Input power - 1 W; (a) Gauss-Hermit model; (b) Gaussian approximation.

The total ohmic losses as a function of z were calculated using (2.44) and are shown in the following plots for the case of wave propagation in the rectangular splitter excited by the TE_{01} CPP mode:



(a)



(b)

Fig. 2.13 Total ohmic losses in the splitter as a function of z . Total input power – 1W;
 (a) Gauss-Hermit model; (b) Gaussian approximation.

Thus, after one round-trip of propagation the total ohmic losses found for the splitter are:

2.03 % found from the Gauss-Hermit model

1.4 % for a Gaussian model

Diffraction losses at the Talbot splitter hole

At the plane $z = 210$ mm, that is at the Talbot length, the splitter is terminated by a conducting plate with a rectangular window in the y -direction as shown in the Fig. 2.14 :

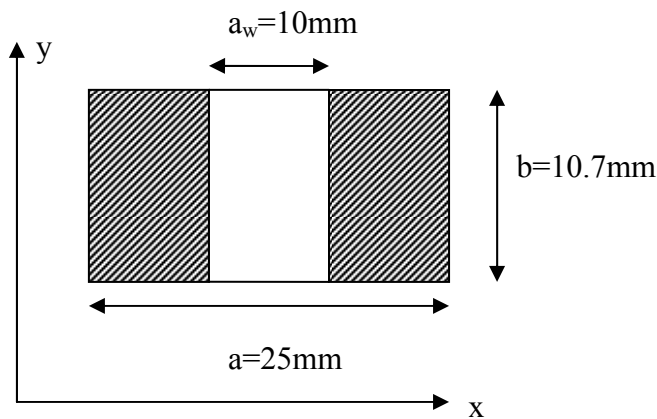
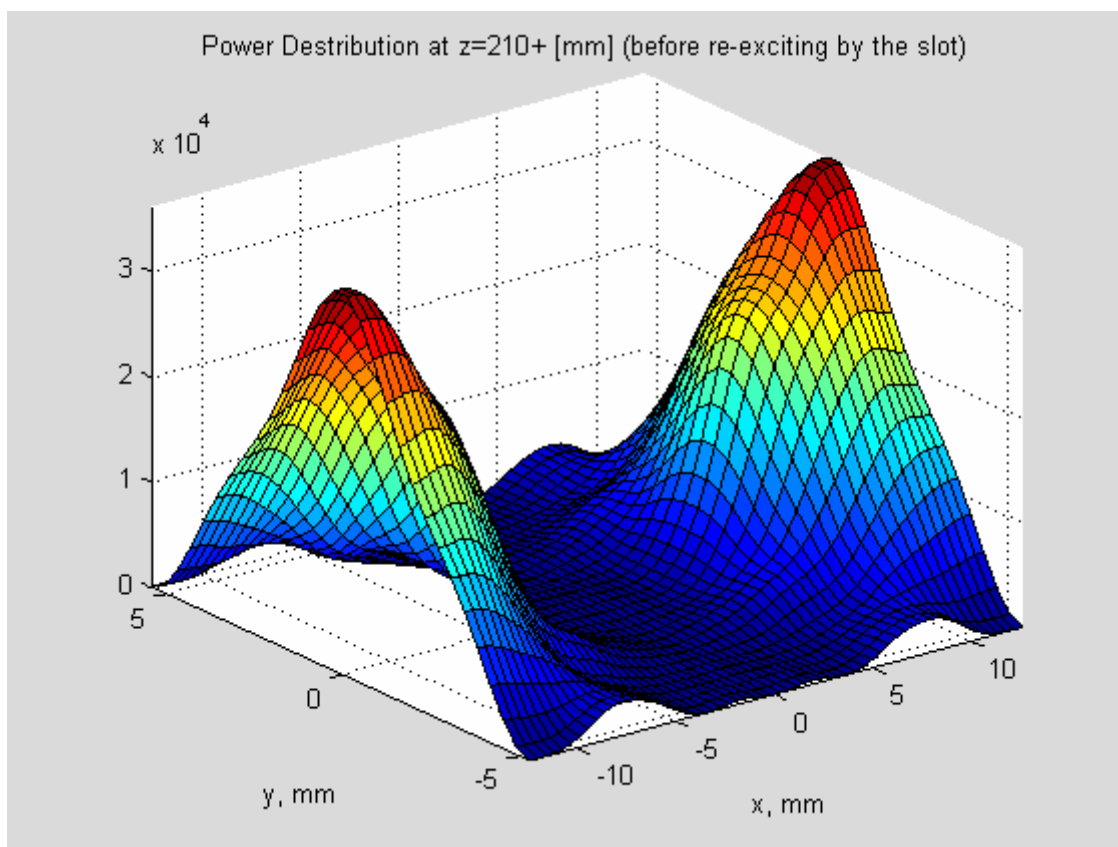
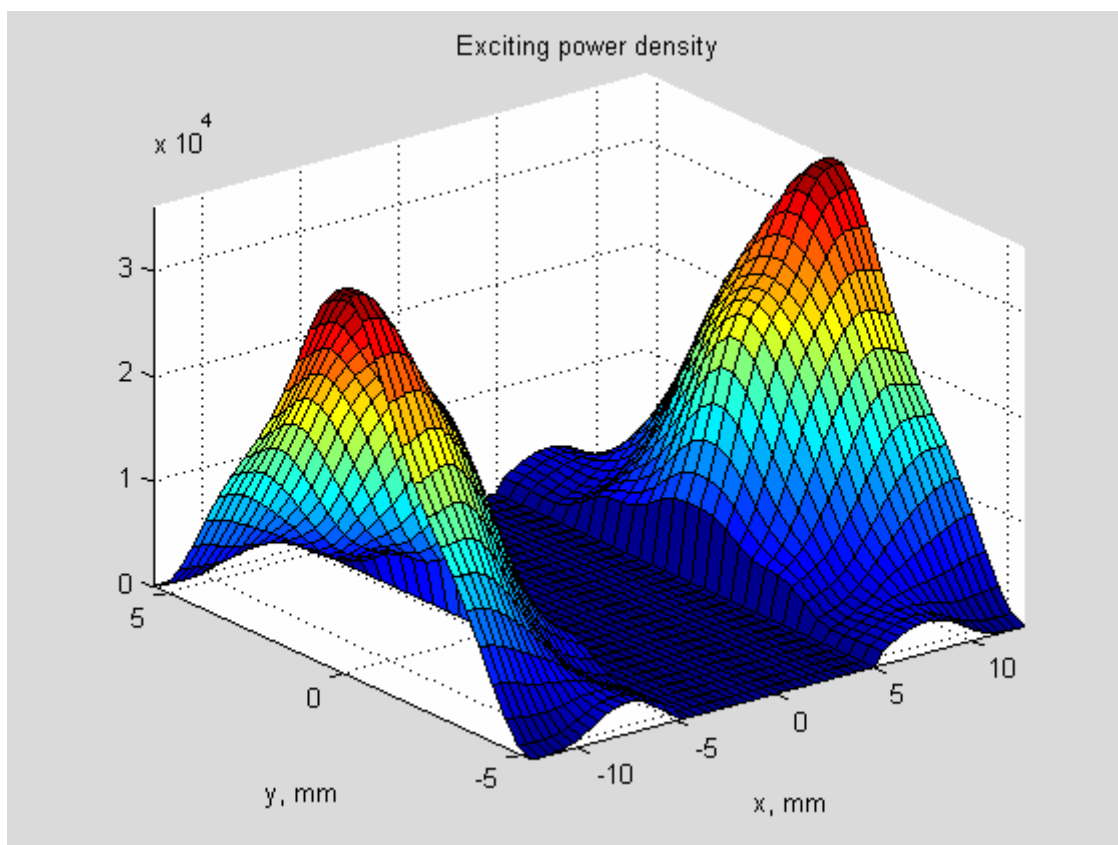


Fig. 2.14 Rectangular window plate terminating the splitter at $z=210$ mm.

Due to the splitting effect, the main part of the wave power density is distributed on the sides (in the x direction) toward the b -walls of the rectangular waveguide, and thus one obtains high power reflection from the terminating plate. Nevertheless, a small part of energy is contained in the tails of split Gaussian -like distribution. It leaks out through the window. A simple way to find the power loss due to this effect is to multiply the power density distribution at the plane of the window by a window function that equals to zero at the mirrors and equals to 1 at the opening. Note that this approximation is possible only for the optical approximation. Such a window in a single mode waveguide represents reactive load not fully matched using free space outside of resonator. The power flow density distribution before and after reflection from the perforated termination is shown in the following figures:

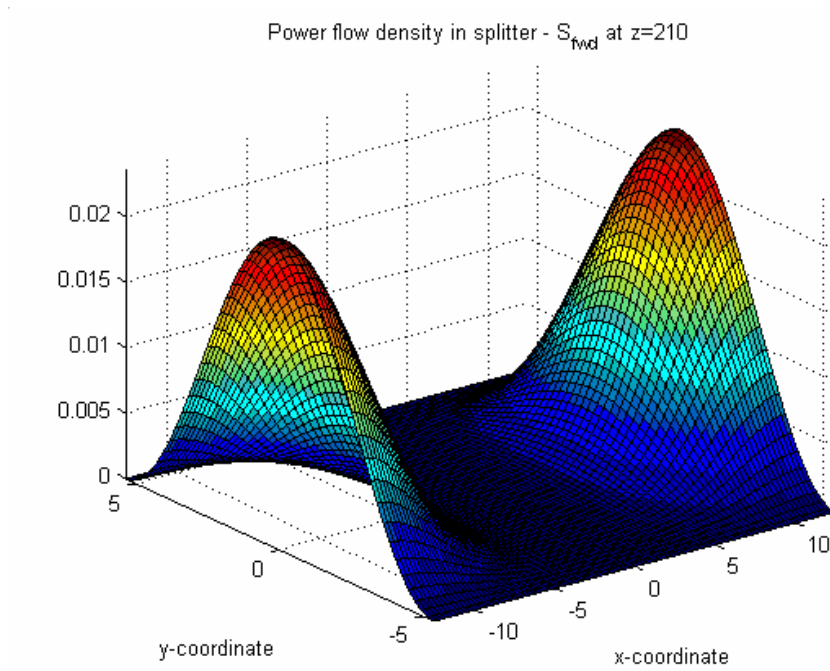


(a)

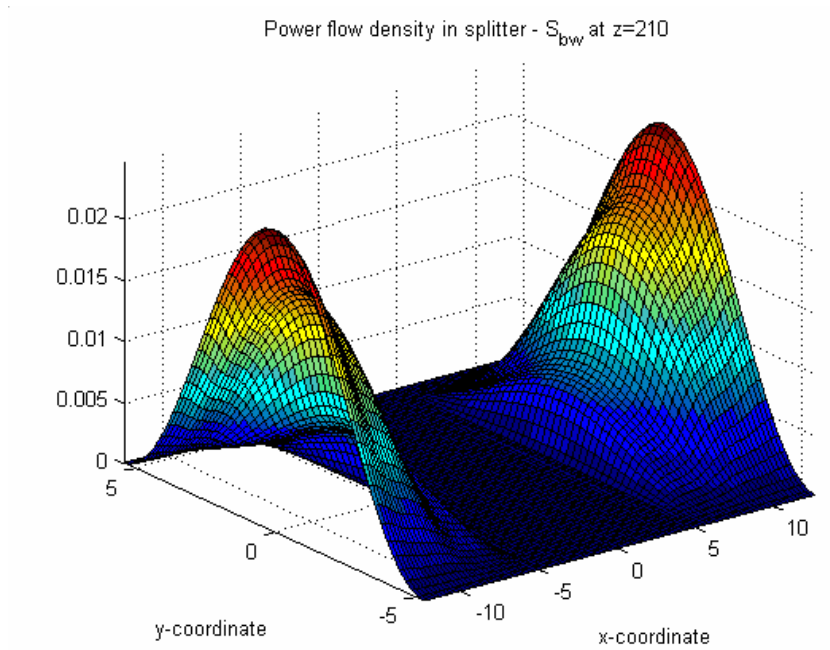


(b)

Fig. 2.15 Power flow density distribution at the end of splitter before (a) and after (b) reflection. Gauss-Hermit model.



(a)



(b)

Fig. 2.16 Power flow density distribution at the end of the splitter before (a) and after (b) reflection. Gaussian approximation model.

Power losses calculated due to power leakage through the window opening are 5.3 %.

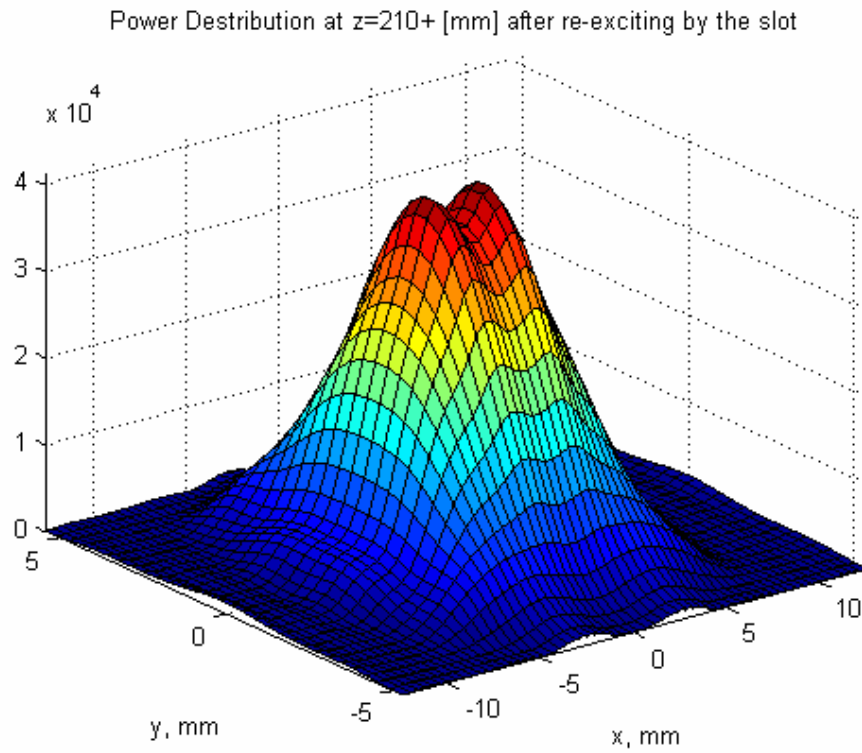
Within the bounds of this approach, calculated power losses are 2 %.

The lost part of energy contains a weighted contribution of each mode. Hence, each mode becomes distorted after reflection from the end mirror, which contains a window. The way to consider this diffraction effect is to calculate the overlap integral again and to find the new modal energy distribution of the reflected wave. This operation does not result in any additional loss, but changes the distribution of the multi-mode backward wave and will affect the further recovery of the original CPP mode distribution by the Talbot imaging effect. Therefore, we shall use the overlap integral technique repeatedly to solve each discontinuity problem in our resonator. For each exciting field distribution there will be a particular set of excited modes. In the case above the wave reflected from the terminating plate excites the full set of rectangular waveguide modes.

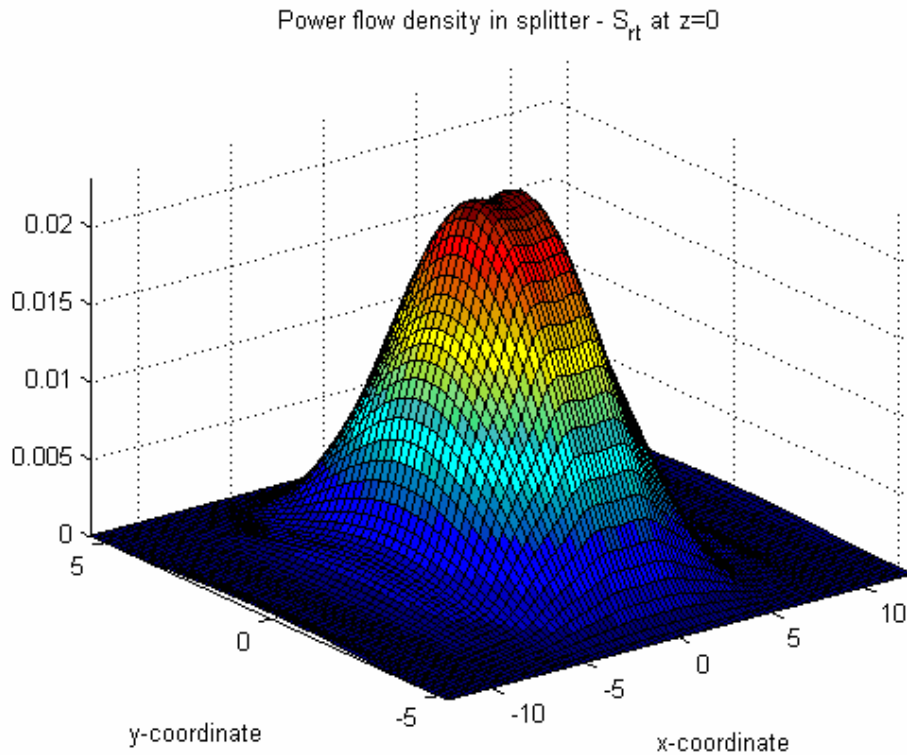
2.7 Re-excitation of the fundamental TE_{01}^{CPP} mode in the Rectangular / CPP waveguides junction

After one round trip of propagation in the splitter, the electromagnetic wave returns to the junction of the different waveguides. The rectangular aperture becomes the exciting field distribution aperture and the curved parallel plate waveguide forms the waveguide of the excited cavity. A similar consideration (see section 2.5) was used to find the amplitude distribution of the excited modes in the rectangular waveguide. Due to the Talbot imaging effect, the transverse power distribution after a round trip in the splitter is expected to regenerate the original distribution of the TE_{01} mode of the CPP waveguide at the $z = 0^+$ plane (see Fig. 2.17). Due to this field distribution

reconstruction, the main part of the energy is concentrated in the center of aperture. Losses at the corners of rectangular waveguide are not significant, and the original TE_{01} mode can be re-excited in the CPP waveguide quite efficiently.



(a)



(b)

Fig. 2.17 Reconstruction of the original distribution due to Talbot effect; Gauss-Hermit model (a); Gaussian model (b);

According to the Gauss-Hermit model, only the following modes meet the synchronism condition with the electron beam [14]:

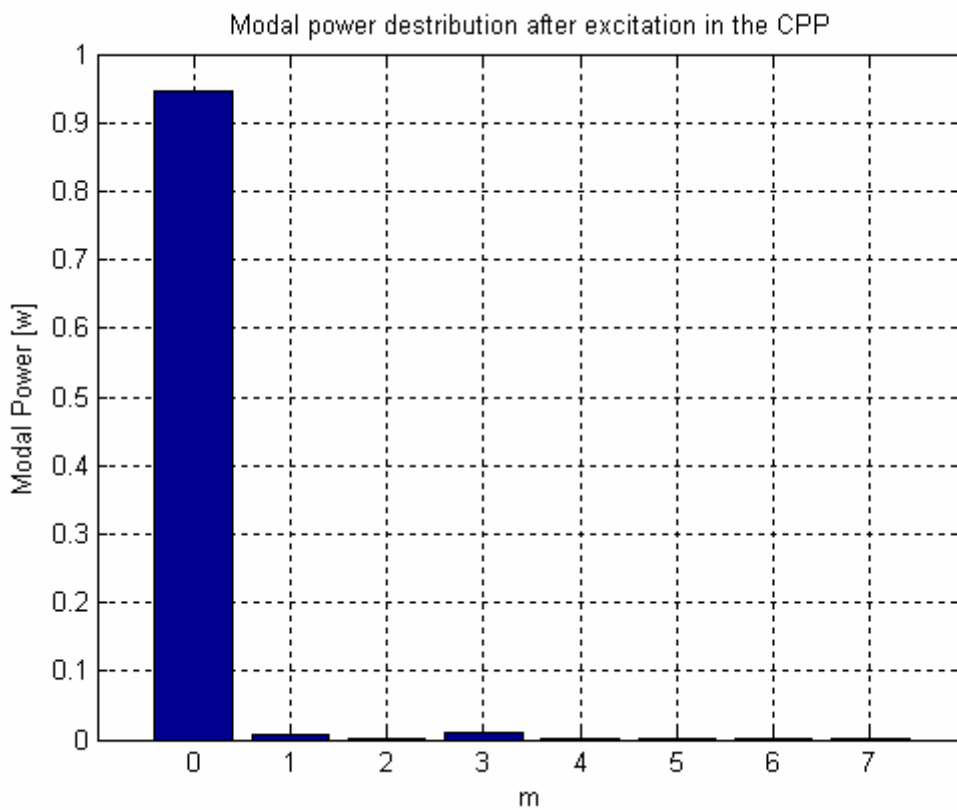
$$TE_{01}, TM_{01}, TE_{10}, TM_{10}, TE_{20}, TM_{20}, TE_{30}, TM_{30},$$

in addition, may be relevant for FEL interaction in the CPP.

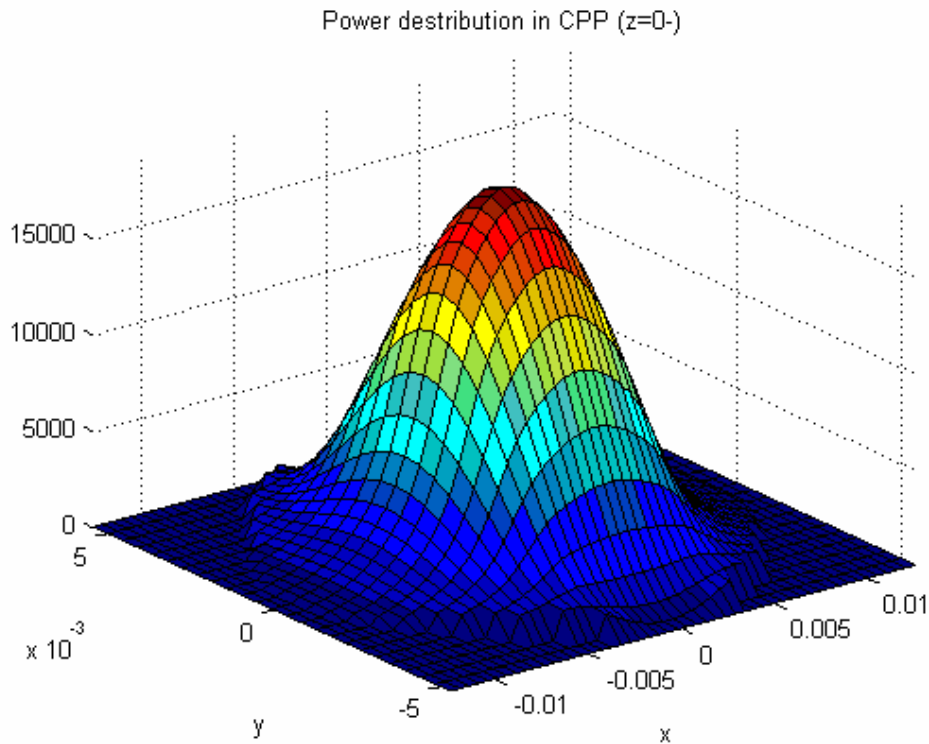
However, only modes TE_{01} and TM_{01} have significant magnitude at the center of the waveguide ($x=y=0$). Hence, for a small radius of electron beam only these modes can be amplified. We are interested in excitation of the TE_{01} mode only, so that the part of energy contained in the excited TM_{01} mode may be said to be lossless (from the FEL operation point of view).

It should be enough to calculate the energy enclosed only in the excited TE_{01} mode. The remainder of energy does not contribute to the FEL amplification process in the laser resonator.

Re-excited modes power distributions at $z = 0^-$ and the power flow density plot are shown in Fig. 2.18:



(a)



(b)

Fig. 2.18 Gauss-Hermit model: re-excited modes power distribution (a); reconstructed power flow density distribution at the CPP aperture at $z=0^-$ (b).

Calculated power loss due to re-excitation of the CPP waveguide by the rectangular aperture distribution of backward wave are:

5.4 % for the Gauss-Hermit model;

1.9 % for the Gaussian model.

2.8 Estimation of the mitre bend losses

The reflector on the decelerator side of the resonator consists of two identical rectangular splitters connected through a waveguide bend that contains of a perforated conductive mirror according to the Fig. 2.19:

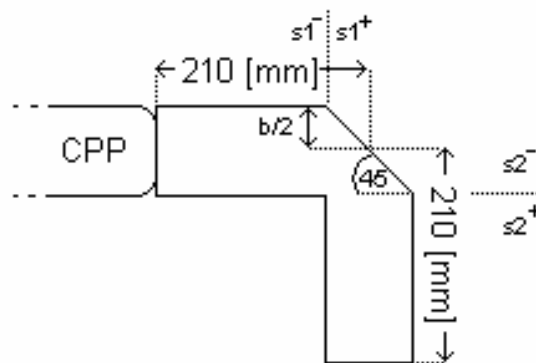


Fig. 2.19 Description for the mitre bend reflector.

As mentioned in the Introduction chapter, such a construction allows one to separate the electron beam and the propagated electro-magnetic energy and allows one to guide the radiation to a user outside of the laser. Using an optical approximation, the split wave is reflects from the waveguide bend metallic mirror at 90° , and continues its propagation without distortion through an addition Talbot splitting section. As a result, one-way passage of the electromagnetic wave through the splitter is equivalent to a round-trip propagation in half of the Talbot length splitter.

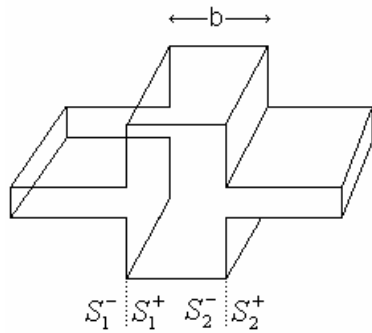


Fig. 2.20 Approximation of the bend region.

The problem of the multi-mode wave propagation in the bend region has no simple analytical solution because of the huge number of modes excited and the interaction of modes in the bend region. Furthermore, the numerical solution is complicated for the same reason, because of limitation of modern computers. However, some approaches to this problem are outside of the scope of this work, but are described in the project of A. Anaton and O. Markish [18]. According to simulation they carried out based on two symmetric aperture transitions (see Fig. 2.20) and calculations of the Fresnel integral of diffraction [18], the power losses for a one-way pass through the bend are 6.2%. The diffraction losses at the round hole in the center of the mirror are 4%. They predict power losses after one round-trip through the bend region of $(6.2 * 2 + 4 * 2) = 20.4\%$. This estimation is a rough approximation and needs more detail consideration. However, one should note that experimental measurement of bend losses gave about $18 \pm 3\%$ round-trip power losses. The Gaussian model calculation gives about 13 % of total power losses in the bend region.

2.9 Conclusions

The different kinds of losses in the resonator can be schematically represented as follows:

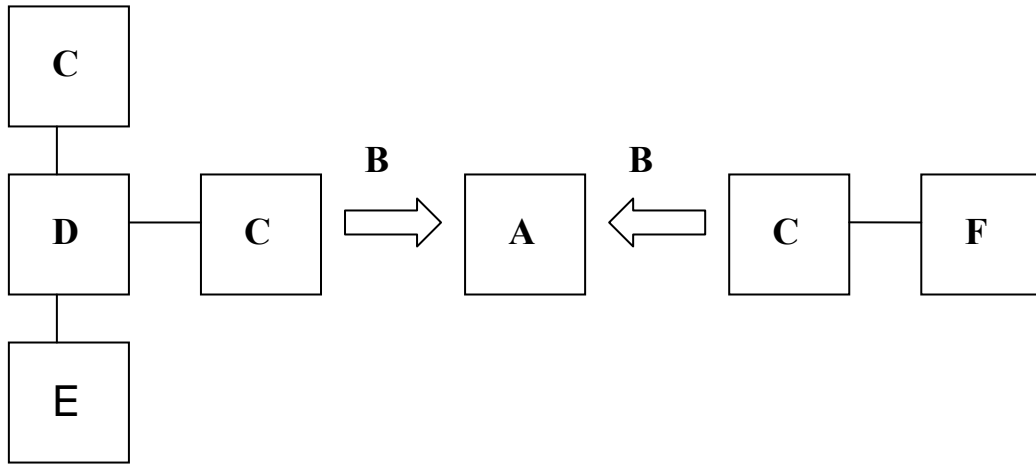


Fig.2.21 Block-diagram of the resonator losses.

Different parts of this diagram are complying with those from Fig. 2.1 and are described in Table 2.1. In the following table, the results of simulations carried out so far are summarized (based on the diagram in Fig. 2.21).

Kind of losses	Block on diagram	Power losses in one round-trip, %; Gauss-Hermit model	Power losses in one round-trip, %; Gaussian approximation
CPP waveguide losses (ohmic + diffraction)	A	~1	~0
CPP-rectangular waveguide (wg) transition loss	Optic approx.	0	0

Rectangular wg ohmic losses	C	2.03	1.4
Rectangular window (beam input) loss	F	5.3	2
Round window (beam output) loss	E	8	2
CPP wg re-excitation loss	B	5.4	1.9
Mitre bend losses	D	12.4	9

Tab.2.1 Distribution of losses in the FEL resonator.

Finally, the total round-trip losses L_{rt} of the resonator can be estimated from the following expression:

$$L_{rt} = A + 2*B + 3*C + D + E + F = 42.5 \% \text{ Gauss-Hermit model}$$

$$L_{rt} = A + 2*B + 3*C + D + 2*E + F = 22.6 \% \text{ Gaussian model} \quad (2.45)$$

References

1. Yariv, A. *Introduction to Optical Electronics*. Holt, Rinehart and Winston, New York, 1976.
2. Collin, R.E. *Foundations for microwave engineering*. 2nd ed. McGraw-Hill, 1992.
3. Ulrich, R., Bridge, T.J. and Pollack, M.A. *A variable Output Coupler for Far Infrared Lasers*. Proc. Symp. On Submillimeter Waves, Polytechnic Inst., Brooklyn, 605-614, 1970.
4. Saleh, A.A.M. An adjustable quasi-optical bandpass filter – part1: theory and design formulas. *IEEE Trans. MTT*, vol. 22, no.7, pp.728-734, 1974.
5. Cornbleet, S. *Microwave optics*. Academic press, 1976.
6. Kapilevich, B., Faingersh, O. and A. Gover Accurate determination of Q-factor of a quasi-optical resonator. *Microwave and Optical Tech .Letters*, vol.36, No.4, 2003.
7. Haus, H. *Waves and Fields in Optoelectronics*. Prentice-Hall, 1984.
8. Fox, A.G. and Li T. Resonant Modes in a Maser Interferometer. *The Bell System Technical Journal*, March, 1961.
9. Culshaw, W. Reflectors for a Microwave Fabry-Perot Interferometer. *IRE Trans. On Microwave and Theory Techniques*, vol.MTT-7, pp.182-189; April, 1959.
10. Culshaw, W. High Resolution Millimeter Wave Fabry-Perot Interferometer. *IRE Trans. On Microwave and Theory Techniques*, vol.MTT-8, pp.182-189; March, 1960.
11. Gover, A., Faingersh, O. and others Radiation measurements in the new tandem accelerator FEL, *Nuclear Instr. And Methods In Physics Research*, A 528 (2004), pp. 23-27.
12. Yakover, I., Pinhasi, Y., and A. Gover. Study of waveguide resonators for FEL operating at submillimeter wavelengths. *Nuclear Instr. And Methods in Physics Research*, A 375, (1996), 260-263.

13. Nakahara, T. and N. Kurauchi. Guided beam waves between parallel concave reflectors. *IEEE Transactions of Microwave Theory and Techniques*, v.MTT-15, no2 (1967), p.66.
14. Lurie Y. Parallel Curved Plates (PCP) versus rectangular waveguide. *Internal report of FEL group*, 14-March-02, Tel-Aviv University.
15. Borgnis, F.E. and C.H. Papas. *Electromagnetic Waveguides and Resonators*. In Encyclopedia of Physics, Ed. S. Fluge (Springer Verlag, Berlin, 1958) v. XVI, pp. 285-422.
16. Kazantsev, Yu.N. *Sov. Radio Eng. Elec. Phys.*, 15 (1970), p.963.
17. Vaganov
18. Anaton, A. and O. Markish. Characterization of mm-wave resonator. *Project submitted for degree "Bachelor of Science"*. Tel-Aviv University, 2003.
19. Ginzton E. L., *Microwave Measurements*. New York: McGraw-Hill, 1957, Chap. 9.
20. Lebedev
21. Altman
22. Asija, A. and A. Gundavajhala. Quick measurement of unloaded Q using a network analyzer, *Rf Design*, pp. 48-52, October 1994.
23. Sucher, M. and J. Fox (eds.), *Handbook of Microwave Measurements*. New York: Polytechnic Press, 1963.
24. Matthaei, G. L., Young, L. and E. M. T. Jones. *Microwave Filters, Impedance-Matching Networks, And Coupling Structures*. New York: McGraw-Hill, 1964, Chapter 11.
25. Kajfez, D. and E. J. Hwan. Q-factor measurement with network analyzer, *IEEE Trans. Microwave Theory Tech.*, vol. MTT-32, pp. 666-670, July 1984.
26. Abramovich A, Pinhasi Y, Yakover YM, Gover A, Sokolowski JS, Canter M. Study of radiation build up and mode evolution in the Israeli electrostatic accelerator free-electron laser oscillator [Journal Paper]. *IEEE Transactions on Plasma Science*, vol.27, no.2, April 1999, pp.563-7. Publisher: IEEE, USA.
27. Sokolowski JS, Abramovich A, Arensburg A, Chairman D, Draznin M, Eichenbaum AL, Gover A, Kleinman H, Pinhasi Y, Yakover YM, Rosenberg A,

- Shiloh J, Cohen N, Levin LA, Shahal O. First lasing of the Israeli tandem electrostatic accelerator free electron laser [Conference Paper]. *Proceedings of the 1997 Particle Accelerator Conference* (Cat. No.97CH36167). IEEE. Part vol.1, 1998, pp.906-8 vol.1. Piscataway, NJ, USA.
28. Talbot H.F. Facts relating to optical science, *no.4, Phil. Mag.*, 9, 1836, pp. 401-407.
 29. Berry M.V., Klein S. Integer, Fractional and Fractal Talbot effects, *J. Modern Optics*, 43, 1996, pp.2139-2164.
 30. Berry M.V., Bodenschatz E. Caustic, multiply-reconstructed by Talbot effects. *J. Modern Optics*, 46, 1999, pp.349-365.
 31. Denisov, G.G., *et al.* Suggestions on FOM-FEM microwave design. Proc. Of second Workshop on FEM-mm waves, Rijnhuizen, September 7-8, 1992.
 32. Denisov, G.G. Microwave systems for millimeter and submillimeter Free Electron Masers, *Nucl. Instr. and Meth.*, A341, 1994.

Chapter 3

Methods for characterization of the mm-wave resonator

3.1 Introduction

Microwave cavities are important microwave devices, which are an integral part of oscillators also in the mm-wave region. Microwave cavities are considered in the literature either from a lumped equivalent circuit viewpoint or from the standpoint of a transmission line bounded by known discontinuities. At high (mm-wave) frequencies, when the resonator dimensions are much larger than a wavelength, a distributed circuit approach must be used. However, a lumped circuit approach would yield the same results if the Q-factor is high (i.e. the losses in the cavity are small). For low Q-factors, the lumped equivalent circuit approximation is not valid. The difficulty stems from the fact that in this case the resonant frequencies are sufficiently close to each other and interfere with the desired frequency, so that the one-pole representation is no longer adequate [19]. The multi-frequency mm-wave cavity is similar to the situation in quasi-optical resonator and may, therefore, be analyzed using optical resonator formulation.

In this chapter we will define the fundamental parameters of distributed resonators and will introduce the different models used for hollow resonators.

Further, we will describe the experimental measurements that were made on the FEL resonator. First, I will present the measurement of the reflection resonant peaks of the FEL resonator and the scheme of measurement will be described. Subsequently, a novel coupling element into and out of the FEL resonator and its calibration procedure will be described. An optical approach for measurements of mm-wave resonator will be formulated based on an optical model for a non-symmetric lossy Fabri-Perot (FP) interferometer. An algorithm which allows estimating the total round-trip reflectivity of

the resonator from the directly measured FWHM (resonance linewidth) will be presented. This parameter is most important because it determines the oscillation threshold of the FEL. We will also introduce a new model of multiple coupled FP interferometers, useful for better matching of the data and interpretation of the measured reflection coefficient patterns. Finally, results of the experimental investigation of the FEL operation with resonator and ways to improve of the resonator for future development of the FEL will be discussed.

3.2 Experimental methods used for Q-factor measurement in the lumped – element circuit (single pole) model

The three fundamental characteristics of an RF resonator that can be determined by measurement are: (1) resonant frequency, (2) coupling coefficient, and (3) unloaded Q factor (Q_0). The last can be defined by using the exact fields inside the resonator. Practical calculation of the values of Q_0 is usually very difficult and it is hard to take into account practical causes of internal resonator losses. As a result, the real value of Q_0 may be much lower than that obtained from exact field equations.

In the past, RF resonators were tested by specialized instruments, such as Q-meters [25]. Those devices have largely been replaced by more universal ones e.g. network analyzers. At microwave frequencies, the Q factor which used to be measured by precision slotted lines, have also been replaced by network analyzers. As will be described in more detail later, a 3-point measurement can determine all the three needed numbers. A novel Q-factor measurement is the use of an over-determined measurement procedure in which some 20 or more points are taken by an automatic network analyzer and subsequently processed by use of a personal computer. The results of the data processing provide not only the three fundamental parameters, but also the estimates on their standard deviations and an estimate of the coupling losses.

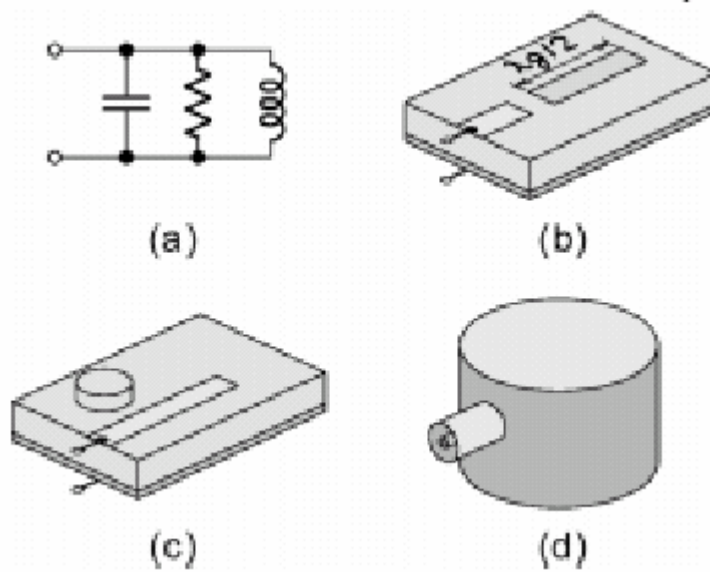


Fig.3.1 Lumped-elements and distributed-elements resonators.

In contrast to a lumped element resonator, a distributed element resonator may be a simple half-wavelength microstrip transmission line, capacitively coupled to a input microstrip line, such as shown in Fig.3.1(b). To achieve a high Q factor, a dielectric resonator can be inductively coupled to the microstrip line, such as in Fig.3.1(c). For high power handling, it may be necessary to employ a hollow cylindrical or rectangular cavity, such as in Fig. 3.1 (d), in which the input is connected to a coaxial transmission line.

Figure 3.2 show the lumped RLC equivalent circuit, which is, according to [25], appropriate for all the distributed element resonators shown in Fig. 3.1. An external RF source of voltage V_s and internal impedance R_c , which is matched to the input transmission line is shown. This source would represent the network analyzer, which is connected to the input port 1 of the resonator through a transmission line and coupling L-R elements. The transmission line of length l , located between input (port 1) and the location of the coupling (port 2) could be physically very short. This length is usually not known very accurately.

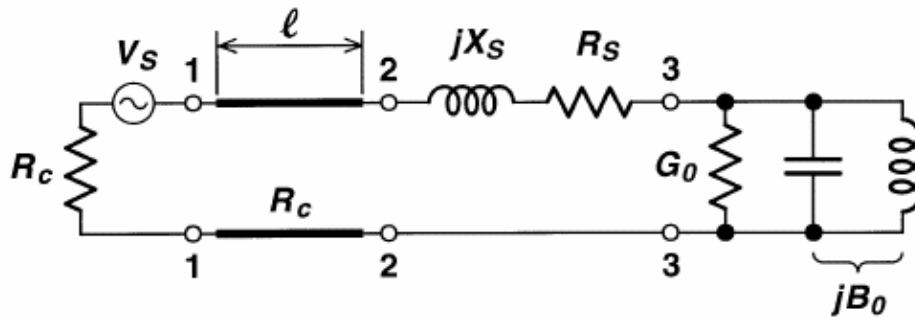


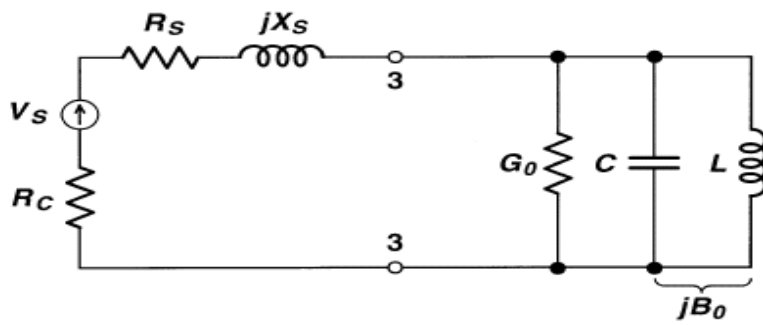
Fig.3.2 A resonator and an external circuit

Port 3 is the location of the resonator itself. The impedance $R_s + jX_s$ represent the transformation properties of the coupling mechanism. For a loop coupling, X_s is a positive reactance, and for a probe coupling, X_s is a negative reactance. The value of X_s can be considered as constant [25] in a frequency range of interest (say 1 % on each side of the resonant frequency). The reactance of the resonator, represented by a parallel LC circuit, varies with frequency hundreds or even thousands time faster than X_s .

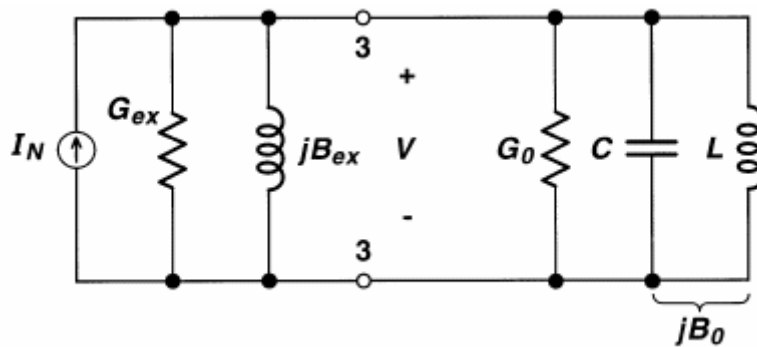
On the right hand side of port 3 is the unloaded resonator. As discussed above, for the case of a low-loss cavity the unloaded Q factor is denoted Q_0 :

$$Q_0 = \frac{2\pi f_0 C}{G_0} \quad (3.1)$$

where f_0 is a resonance frequency. The conductance G_0 represents the dissipation inside the resonator proper. Typically, this dissipation is caused by conductor losses and by dielectric losses G_0 . The corresponding resistance R_0 is the inverse value, $R_0 = 1/G_0$.



(a)



(b)

Fig.3.3 (a) Thevenin and (b) Norton equivalent circuits for port 3.

To the left of port 3 (towards port 1), is the series resistance R_s and the reactance X_s , and behind them a transmission line terminated in a Thevenin source. As the source impedance is equal to the characteristic impedance of the transmission line, the length of the transmission line does not change the impedance seen by the observer (any length of a transmission line, which is terminated in a matched load, has input impedance, equal to R_c).

Using circuit theory, the external circuit, can be replaced by a Norton equivalent, consisting of a current source in parallel with the impedance, as shown in Fig.3.3(b). As a further simplification, the impedance $R_c+R_s+jX_s$ can be transformed into an admittance $G_{ex}+jB_{ex}$ as shown in Fig.3.3(b), thus is the external admittance of the resonator.

At port 3 one may note that the external circuit influences the resonator in two ways. First, the susceptance B_{ex} detunes the resonant frequency. However, this

frequency shift is usually small, and is of little consequence. The loaded resonator has a slightly different resonant frequency. Secondly the, conductance G_{ex} is in parallel with G_0 . Thus the coupling elements increase the resonator conductance to $G_0 + G_{ex}$, lowering the overall Q to a value Q_L , expressed by

$$\frac{1}{Q_L} = \frac{1}{Q_0} + \frac{1}{Q_{ex}} \quad (3.2)$$

where the external Q factor Q_{ex} is:

$$Q_{ex} = \frac{2\pi f_0 C}{G_{ex}} \quad (3.3)$$

The ratio of the power dissipated in the external circuit to the power dissipated in the resonator is called the coupling coefficient k . As both G_0 and G_{ex} are at a voltage V , the ratio of powers is equal to the ratio of conductances:

$$k = \frac{V^2 G_{ex}}{V^2 G_0} = \frac{G_{ex}}{G_0} = \frac{Q_0}{Q_{ex}} \quad (3.4)$$

If the power dissipated in the external circuit is equal to the power dissipated in the resonator, the coupling is said to be critical, and the coupling coefficient in this case is $k=1$. Undercoupling regime means that more power is dissipated in the resonator than in the external circuit, while overcoupling regime means that more power is lost in the external circuit than in the resonator. Use of (3.2) in Eq.(3.4) gives the relationship between unloaded and loaded Q :

$$Q_0 = Q_L(1 + k) \quad (3.5)$$

In the process of measurement, the resonator is loaded by the external circuit (here the network analyzer), and the measurement will yield the loaded Q, Q_L . For strong coupling between the network analyzer and the resonator, the measured loaded Q is lowered. To find the unloaded Q, the measurement should be designed in such a way, that it also provides the value of the coupling coefficient k. Then, using Q_L and k, one computes Q_0 from Eq.(3.5). This is how most Q factor measurements are made [19], [24].

For this resonator measurement one needs one port only. When the network analyzer is attached to this port, the equivalent circuit looks as shown in Fig.3.2. The measurement procedure is well documented in microwave measurement handbooks such as Ginzton [19], Sucher and Fox [23], or Matthaei, Young and Jones [24]. Although these books were written before the first network analyzer was made, the principles involved remain unchanged from the slotted-line and admittance-bridge era. With few modifications, the reflection-type measurement can be performed with a network analyzer [25]. The beauty of this measurement is that a perfect circle that gives the reflection coefficient is plotted on a Smith chart, measured as a function of frequency. (If one does not get perfect circle, there is usually something wrong with the calibration or the reference position!)

3.3 The Measurement Scheme Used in the Present Study

The quasi-optical mm-wave resonator was assembled and installed into the accelerator tank in January 2002. The configuration of the resonator installed in the FEL is shown in Fig. 3.4:

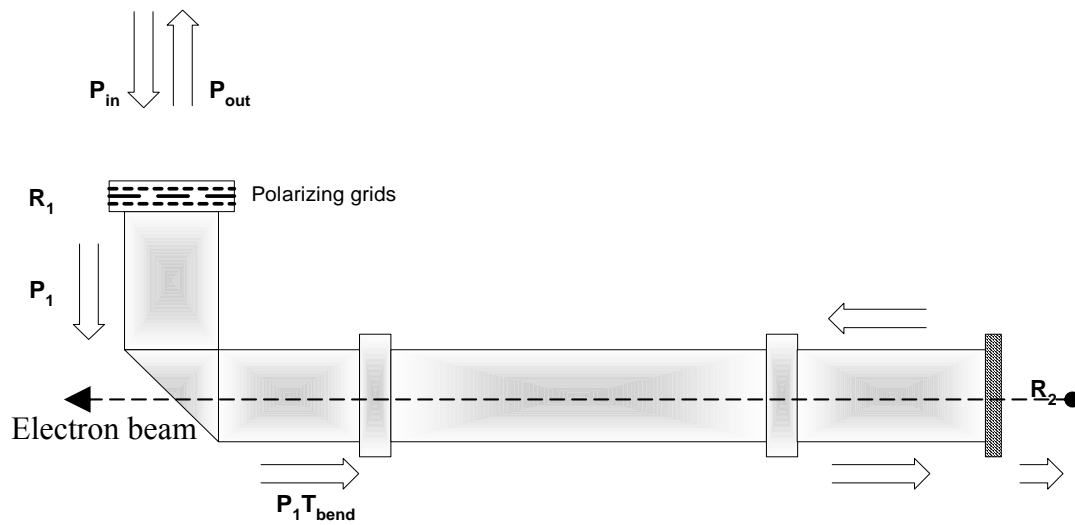
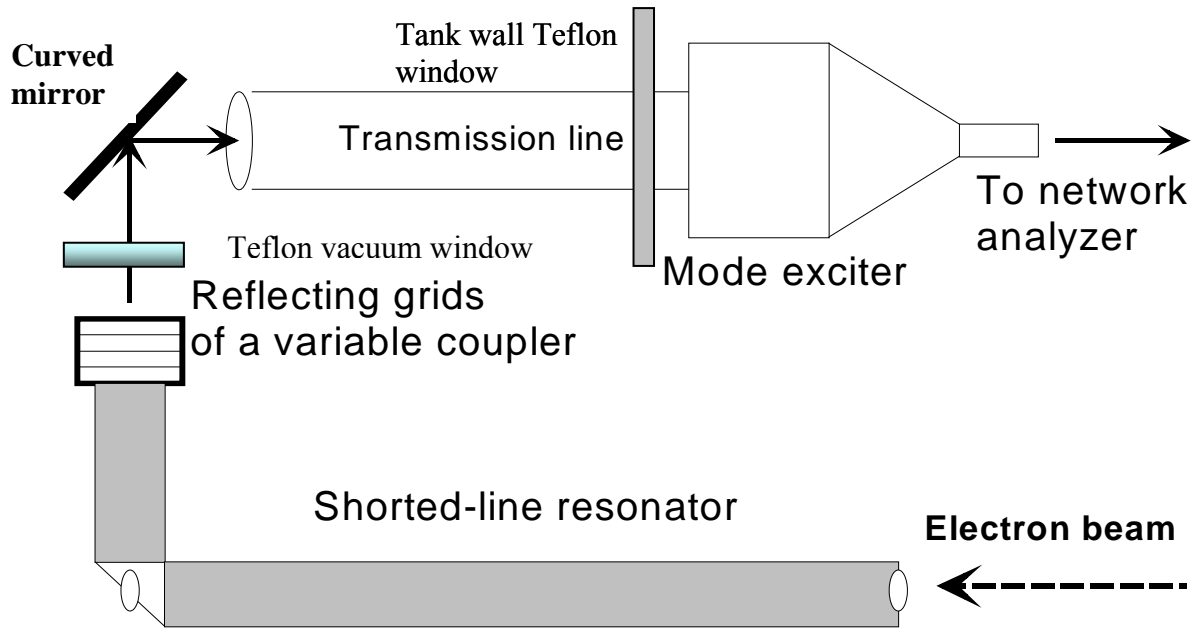


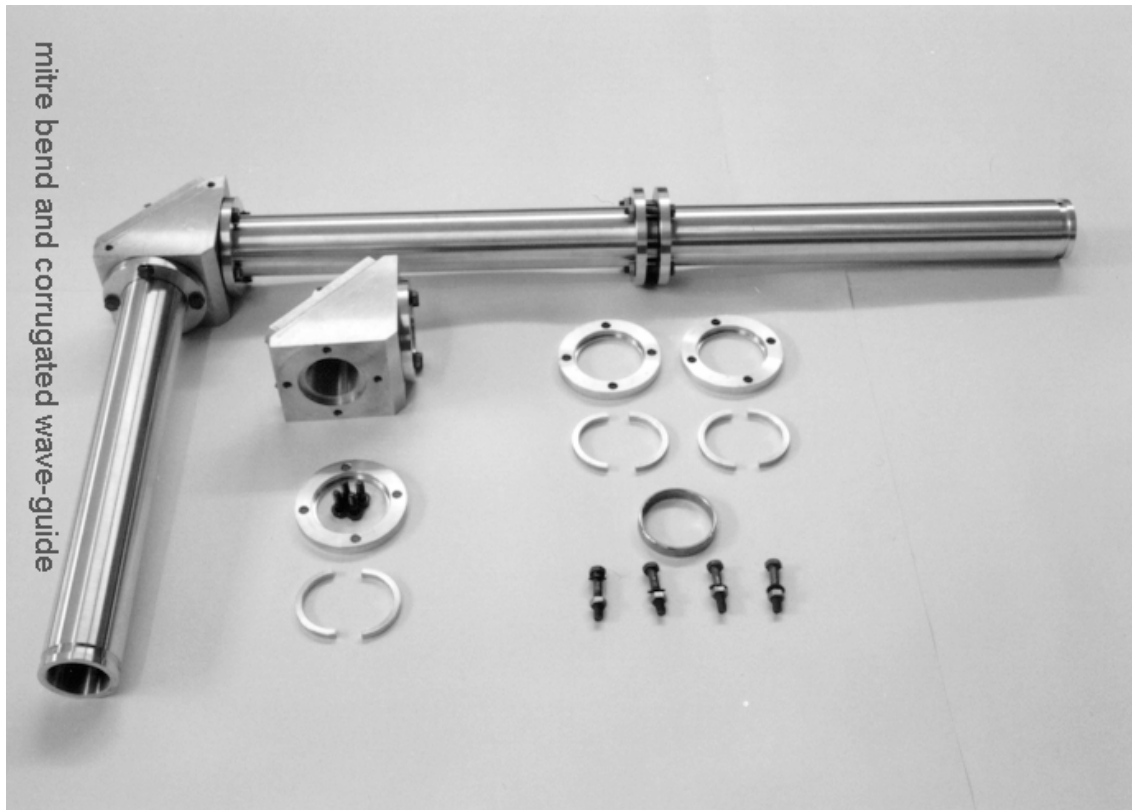
Fig. 3.4 Resonator configuration.

Attainment of low round-trip resonator losses (smaller than the FEL single-path gain) is a necessary condition for obtaining the desired laser operation. Therefore, accurate experimental measurements of resonator losses are most important.

The resonator location in the wiggler allows a signal for probing the resonator to be fed only from the coupling element end. Thus, excitation of the resonator for the measurement of its quality is accomplished by energy feed through the coupler. The coupling coefficient was determined separately and the signal reflected from the resonator system was measured. The theory described in Chapter 2 and the theory of optical resonators predicts that the reflection coefficient of a resonant cavity is minimal at the resonance frequency and it is maximal at antiresonance [2]; there is a periodicity in the absorption peaks. Information on internal resonator losses can be extracted from the measured pattern of reflection coefficient vs. frequency. The experimental scheme for reflection coefficient measurements is shown in the figure 3.5:



(a)



(b)

Fig.3.5 (a) Schematic of the experimental setup for reflection coefficient measurements; (b) transmission line components: mitre bend and cylindrical corrugated waveguide.

The measurement equipment comprises a microwave source in the W-band range (75-115 GHz), a wide frequency band sweeper and a Scalar Network Analyzer (SNA). The input wave was transformed using a specially designed mode exciter in order to obtain a good matching between the signal source and the circular waveguide. The probing wave and the wave reflected from the resonator are transmitted through the corrugated circular waveguide mm-wave transmission line that was developed to transmit the FEL radiation from the resonator outcoupler out of the accelerator (see Fig.3.5). The transmission line is about 5m long. To obtain good matching between the circular aperture of the feed transmission line and the rectangular aperture of the resonator splitter, a

special curved off-axis matching mirror was used. The transmission coefficient of the variable outcoupler was about 10% and provided weak coupling between the resonator and an external load (source, network analyzer, corrugated transmission line and matching curved mirror).

The measured power reflection coefficient is shown in Fig. 3.6:

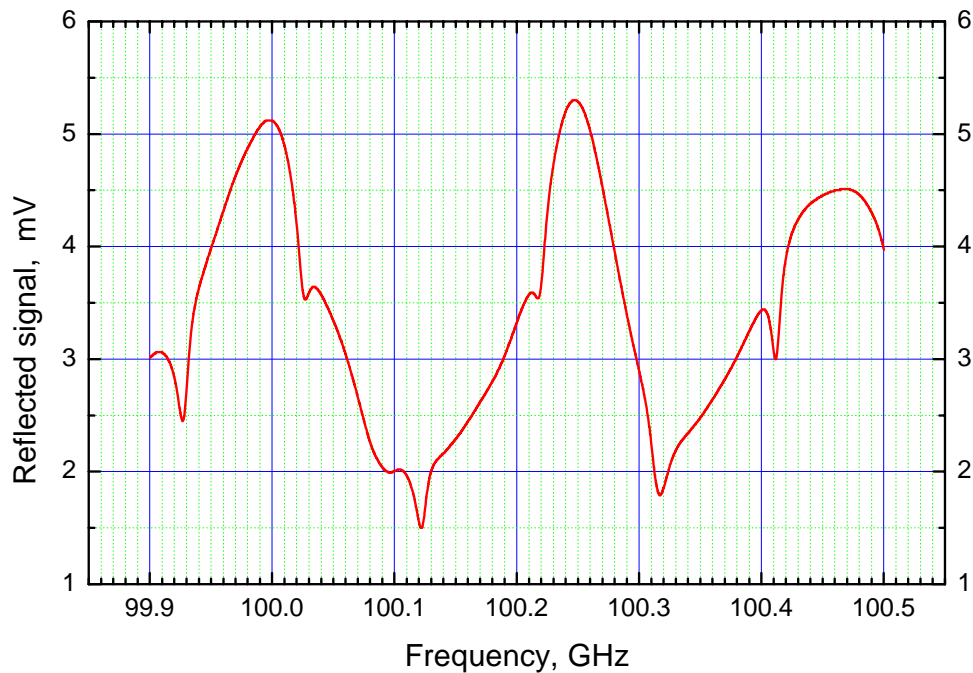


Fig.3.6 Measured resonator response (narrow peaks) masked by a large amplitude “low frequency” parasitic reflection pattern.

The weak power absorption dips correspond to resonance absorption of the resonator for weak coupling. The “low-frequency” envelope curve is due to parasitic reflections between mismatched sections in the transmission system. An attempt was made to eliminate parasitic reflections and to extract the intrinsic resonator behavior.

Using the FFT computer filtering procedure from the “MicroCal Origin” program libraries we strongly reduce the “low frequency” spectral pattern

associated with parasitic reflections. The resulting spectral pattern is shown in Fig.3.7:

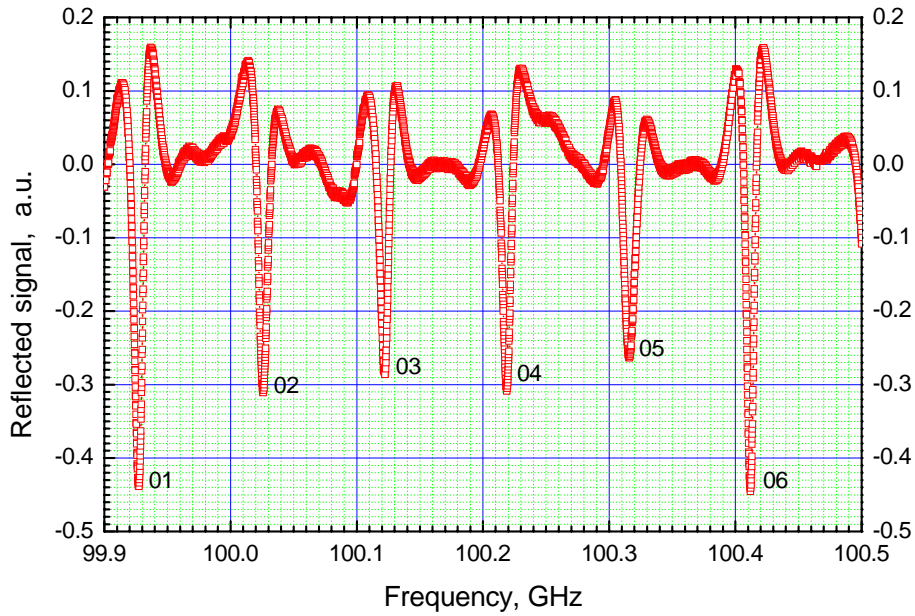
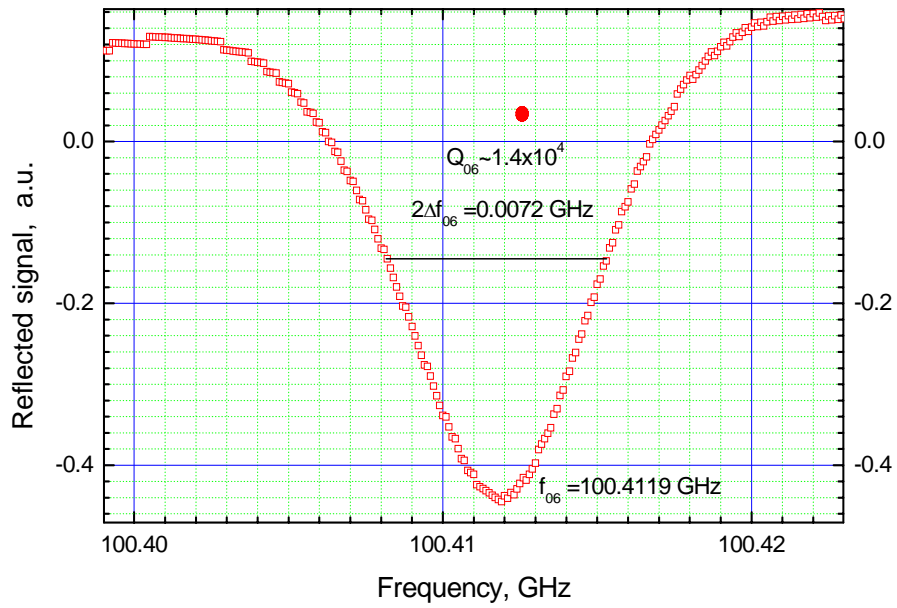


Fig. 3.7 Resonance peaks pattern of the excited FEL resonator obtained from Fig.3.6 by strongly reducing parasitic reflection.

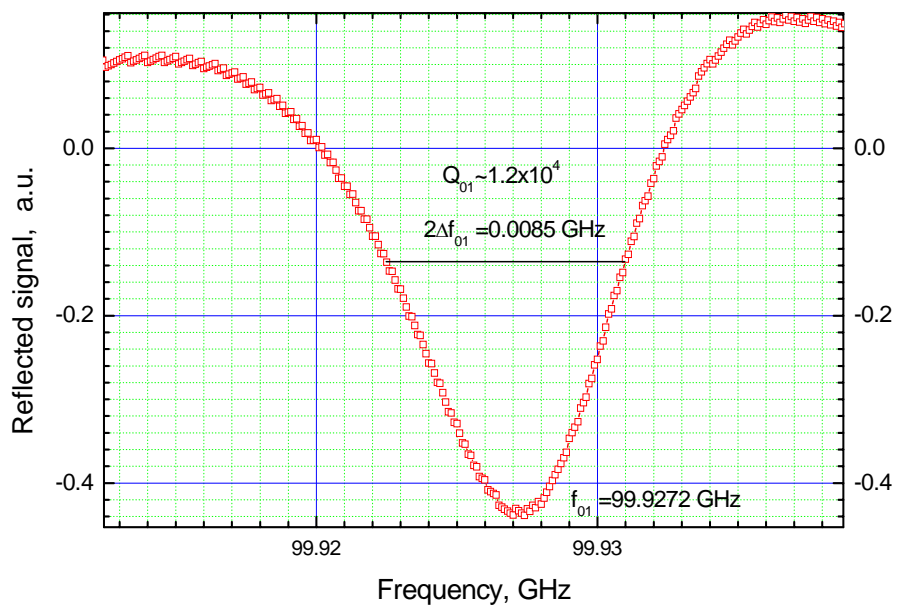
A crude estimate of resonator losses was made by calculation of the loaded Q-factor of the resonator according to:

$$Q = \frac{f_0}{\delta f_{1/2}} = \frac{\delta \lambda_{1/2}}{\lambda_0} \quad (3.6)$$

where f_0 is the resonant frequency of a particular peak and $\delta f_{1/2}$ is the -3dB bandwidth of that peak. The results for two typical peaks (#1 and #6 in the Fig.3.7) are shown in Fig. 3.8:



(a)



(b)

Fig. 3.8 Calculated loaded Q-factor of the resonator: (a) peak #6, $f_0=100.41$ GHz; (b) $f_0=99.93$ GHz.

3.4 The Adjustable Grid Reflector/Outcoupler

3.4.1 3-grid coupler

The adjustable coupling element consists of a set of three polarizing grids which are parallel to each other and assembled into one unit as depicted in Fig. 3.9:

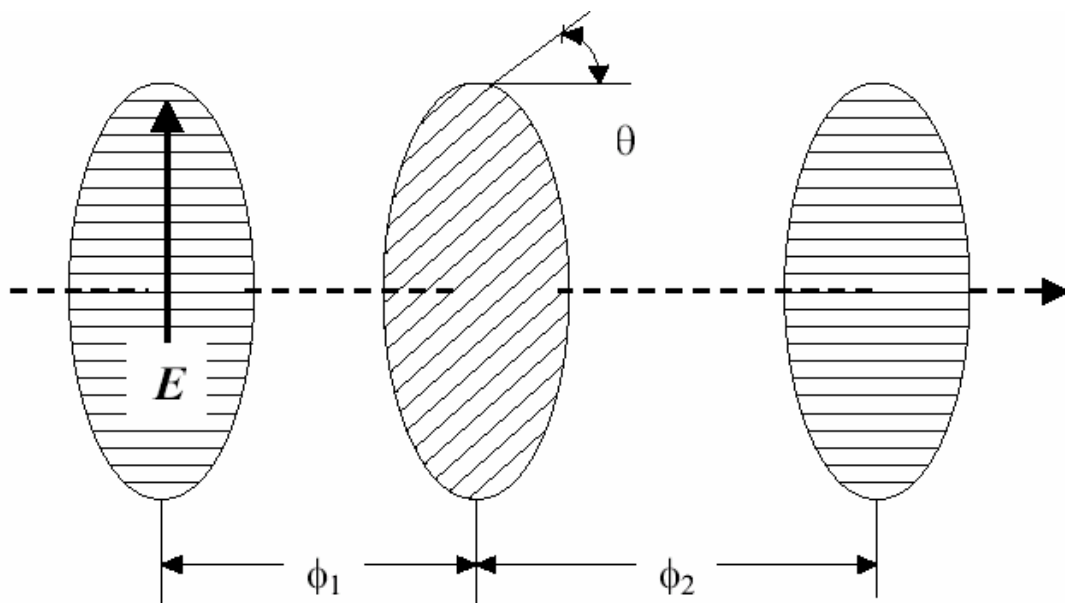
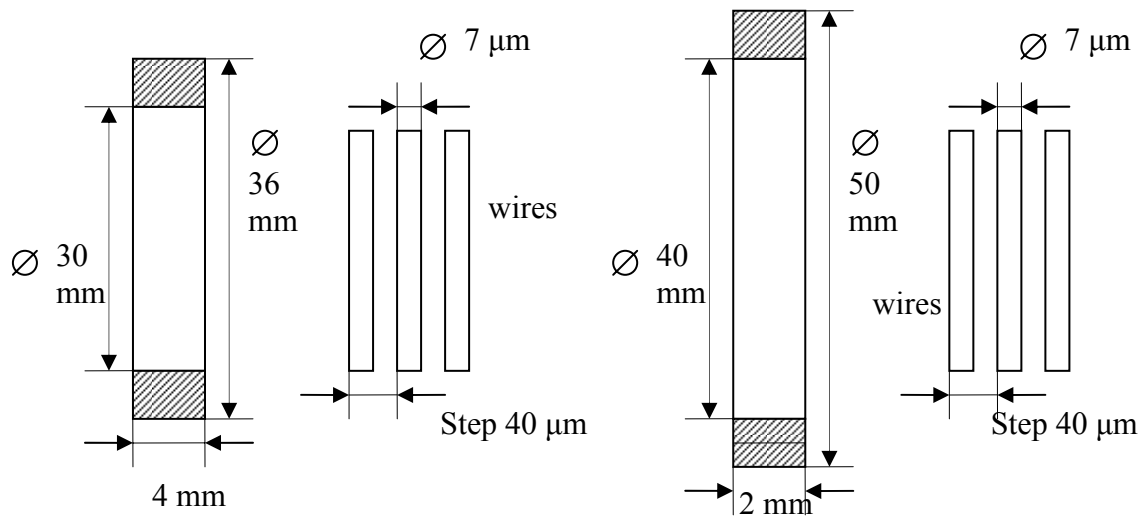
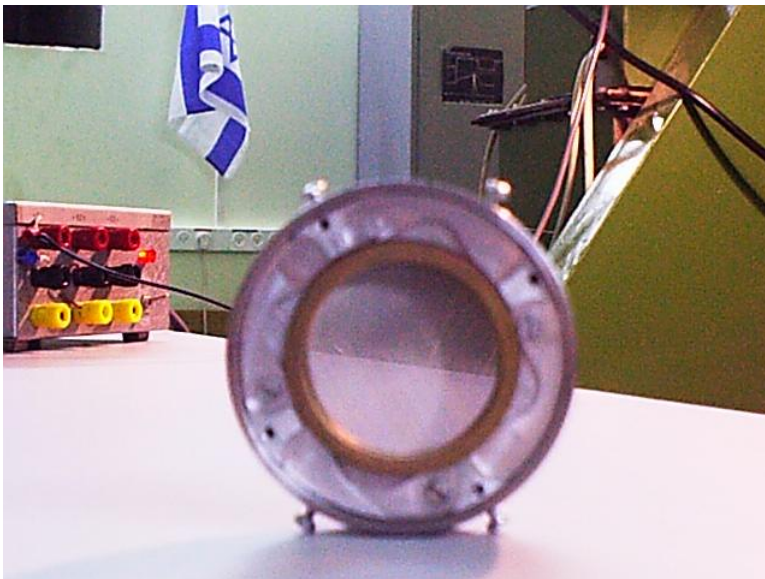


Fig. 3.9 Adjustable 3-grids coupler.

Each grid is a diffraction lattice using parallel Tungstem wires supported by a copper frame. The diameter of the two outer grids is smaller than the central grid as shown in Fig. 3.10:



(a)



(b)

Fig.3.10 Structure and dimensions of the polarizing grids (a); the grid in its supporting ring (b).

The two outer grids are fixed and allow maximum transmission of power. This occurs if the parallel grid wires are perpendicular to the E-field polarization of the incident wave [2]. The inner grid can be rotated so that the angle Θ between the parallel grid wires and the electrical field direction can be adjusted (Fig. 3.9). The wave incident on the central grid can be considered as the composition of two waves – one polarized parallel to the wires and the other perpendicular to them (Fig.3.11):

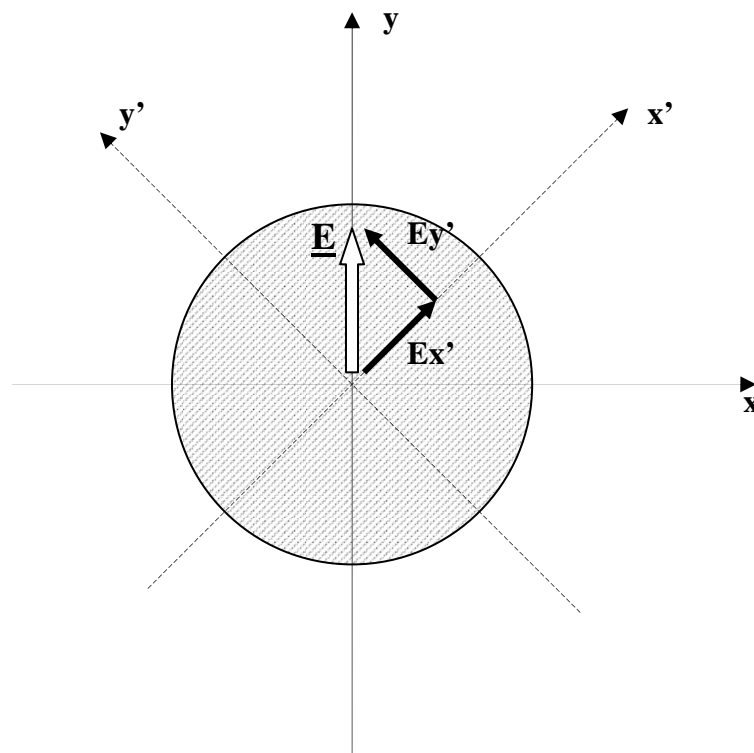


Fig.3.11 Central grid: decomposition of the incident wave \bar{E} into E'_x and E'_y .

The decomposed incident wave component polarized perpendicular to the wires ($E_{y'}$ in Fig.3.11) is transmitted because the grid is transparent for this polarization. The part of the decomposed incident wave polarized parallel to the wires ($E_{x'}$ in Fig.3.11) is reflected (except for ohmic losses of the filaments) towards one of the outer grids. Because of this 3-grid system, the wave, incident on the 3-grid reflector and the wave reflected from it are of the same

polarization. Similarly, the transmitted wave (after passing three grids) is also in the original polarization direction. The 3-grid reflector is used as a coupling element between the resonator cavity and the feeding transmission line. It allows adjustment of the reflection (transmission) coefficient without changing the polarization of the waves reflected into (transmitted out) the resonator.

A theoretical description of the operation of the 3-grids system may be found in [3] and [6]. According to [3], a system consisting of three grids can be subdivided into two basic sections separated by electrical lengths ϕ_1 and ϕ_2 . Each section consists of two successive grids and the space between them. The scattering matrix of each section can be written using network representation [4], [5] as:

$$[A_p] = \frac{1}{\cos\theta} \begin{bmatrix} \cos\Phi_p & i\sin\Phi_p \\ \frac{i(\cos^2\theta - \cos^2\Phi_p)}{\sin\Phi_p} & \cos\Phi_p \end{bmatrix} \quad (3.7)$$

where $\Phi_p = kd_p = \omega d_p/c$ is the phase change between 2 adjacent grids given in radians, d – is the physical distance between grids and $p = 1$ or 2 according to the selected pair of grids.

The total scattering matrix of the 3-grid system is calculated by multiplying the A matrices of the two basic sections $[A] = [A_1] \cdot [A_2]$. Using (3.7) the elements of $[A]$:

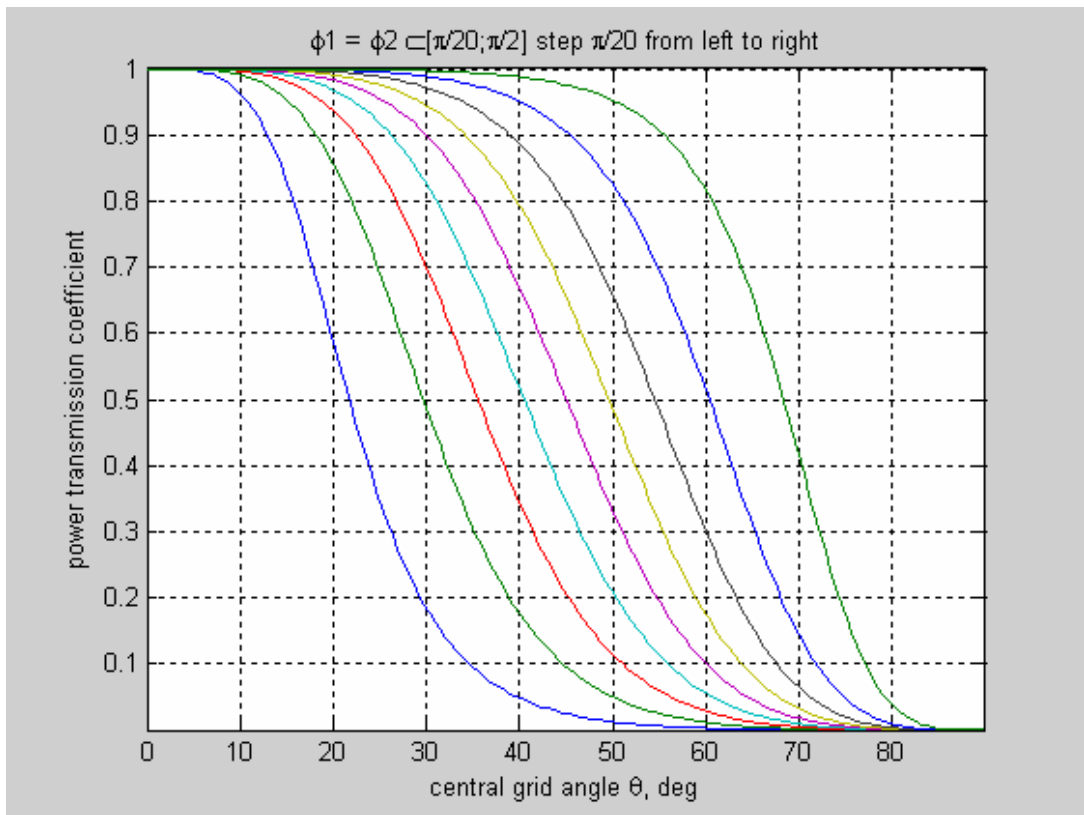
$$\begin{aligned} A_{11} &= \frac{1}{\cos^2\theta} \left[\cos\Phi_1 \cos\Phi_2 - \frac{\sin\Phi_1(\cos^2\theta - \cos^2\Phi_2)}{\sin\Phi_2} \right] \\ A_{12} &= \frac{i\sin(\Phi_1 + \Phi_2)}{\cos^2\theta} \\ A_{21} &= \frac{i}{\cos^2\theta} \left[\frac{\cos\Phi_2(\cos^2\theta - \cos^2\Phi_1)}{\sin\Phi_1} + \frac{\cos\Phi_1(\cos^2\theta - \cos^2\Phi_2)}{\sin\Phi_2} \right] \end{aligned} \quad (3.8)$$

$$A_{22} = \frac{1}{\cos^2 \theta} \left[\cos \Phi_1 \cos \Phi_2 - \frac{\sin \Phi_2 (\cos^2 \theta - \cos^2 \Phi_1)}{\sin \Phi_1} \right]$$

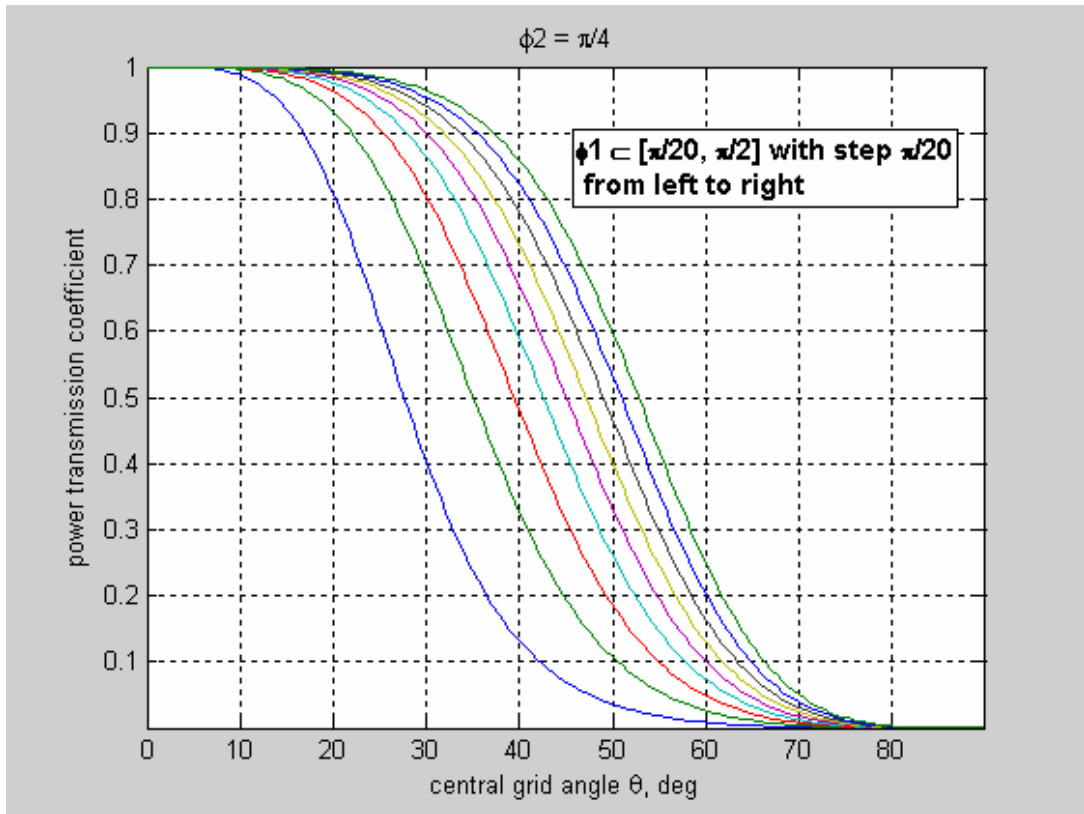
The power transmission coefficient T can be calculated [2]:

$$T = \frac{4}{|A_{11} + A_{12} + A_{21} + A_{22}|^2} \quad (3.9)$$

The power transmission coefficient of the 3-grids tunable reflector as a function of the central grid rotation angle for the different distances between the grids is shown in Fig. 3.12:



(a)



(b)

Fig.3.12 Power transmission coefficient of the adjustable 3-grids coupler: (a) – for equidistant phase shift and spacing $\Phi_1 = \Phi_2$; (b) – for non equal spacing $\Phi_2 = \pi/4$, $\Phi_1 \neq \Phi_2$. Frequency – 100GHz.

According to [6], for optimal spacing between the grids a symmetrical curve around the half-power transmission points is obtained; minimal internal re-reflections between two neighboring grids are obtained for:

$$\phi_{opt} = k \frac{\lambda}{8} = \frac{\pi}{4} [rad] \quad (3.10)$$

In this case Eq.(3.9) may be rewritten as:

$$T = \frac{\sin^4 \theta}{\cos^4 \theta + \sin^4 \theta} = \frac{1}{1 + \text{ctg}^4 \theta} \quad (3.11)$$

Finally, it should be noted that the transmission coefficient of a isolated single grid depends on the angle between the direction of the grid wires and the incident wave polarization (goes as $\sin^4 \theta$).

3.4.2 Measurement of the 3-grid coupler reflection coefficient

The experimental arrangement for the measurement of the 3-grid coupling element is shown in the Fig. 3.13:

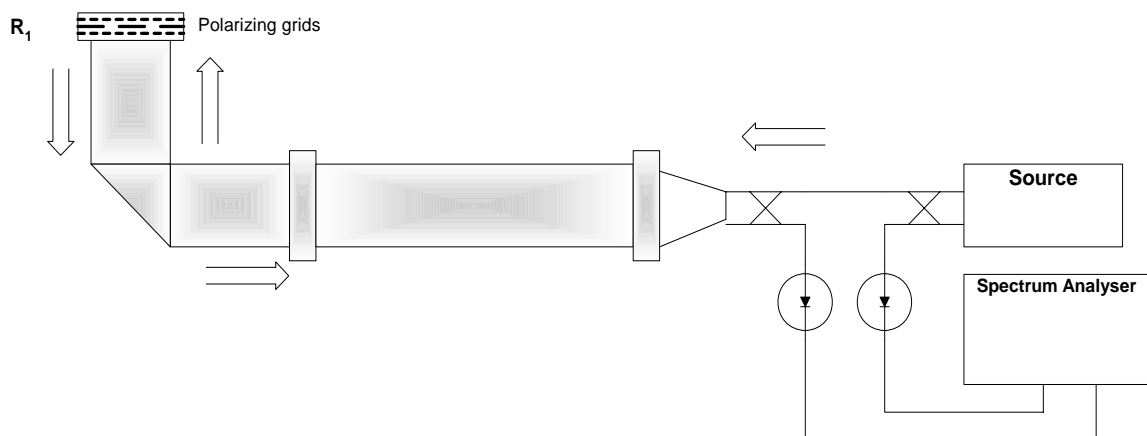
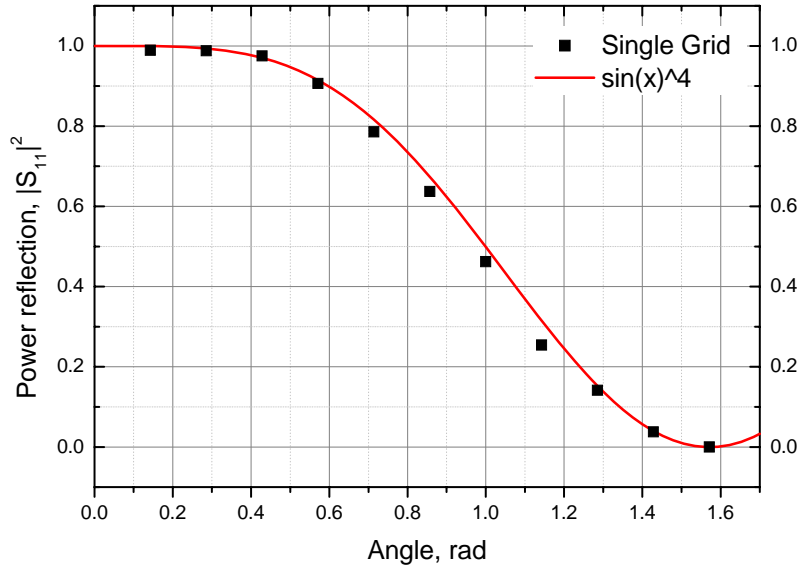


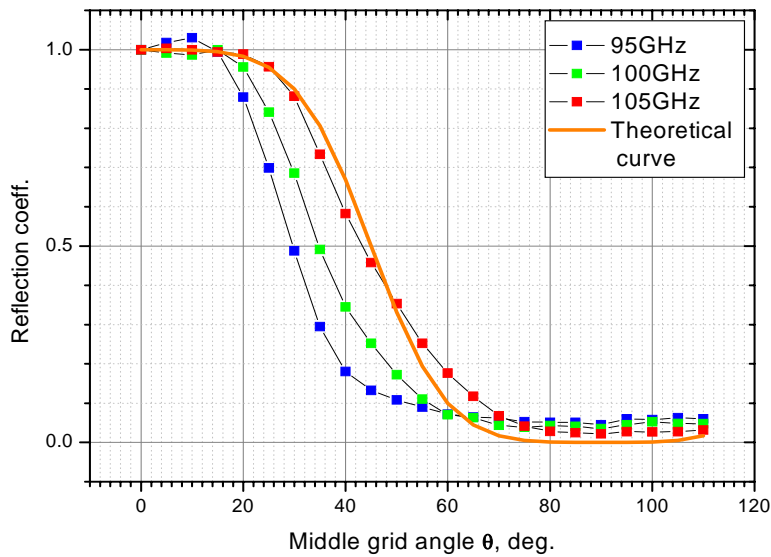
Fig.3.13 Scheme of setup for the reflection coefficient measurement.

The 3-grid coupling element, which enabled control of the resonator end reflector from short to full transmission by adjusting the inner grid angle, was assembled and placed at the output of the resonator bend section. At the other end, the resonator was excited by a HP 100 GHz source through a mode exciter that converts the TE_{01} mode of the source output waveguide to the hybrid mode of the CPP waveguide. The power reflected from the grids was measured. The

results of the reflection coefficient measurement as a function of the rotation grid angle are shown in Fig. 3.14 for several frequencies:



(a)



(b)

Fig.3.14 Reflection measurement: (a) single grid; (b) set of three parallel grids.

The measured data (shown in Fig.3.14) is in good agreement with theory. One can conclude from the plot of Fig. 3.14 (b) that grid spacing is nearly optimal at a frequency $f = 105$ GHz. An additional conclusion is that the 3-grid reflector can be used as a suitable coupling element in FEL resonators, providing coupling which can varied continuously from zero reflection to total reflection.

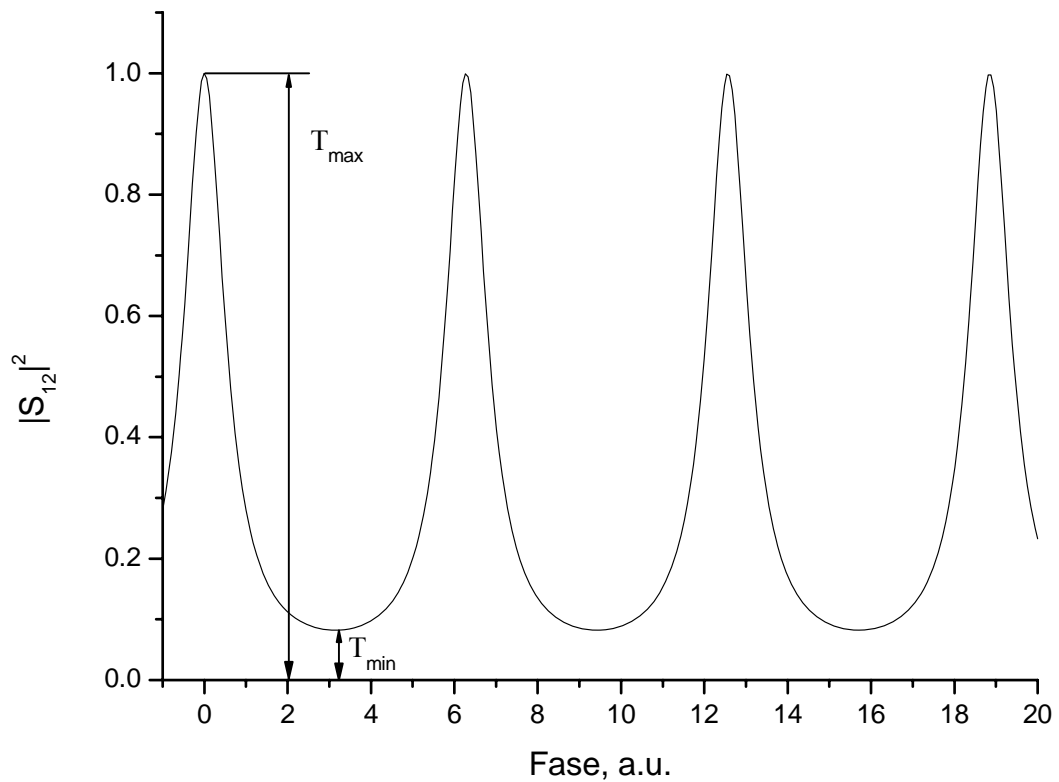
3.5 Fabri-Perot Resonator Model. Optical Approach

3.5.1 Fabri-Perot Interferometer with Losses

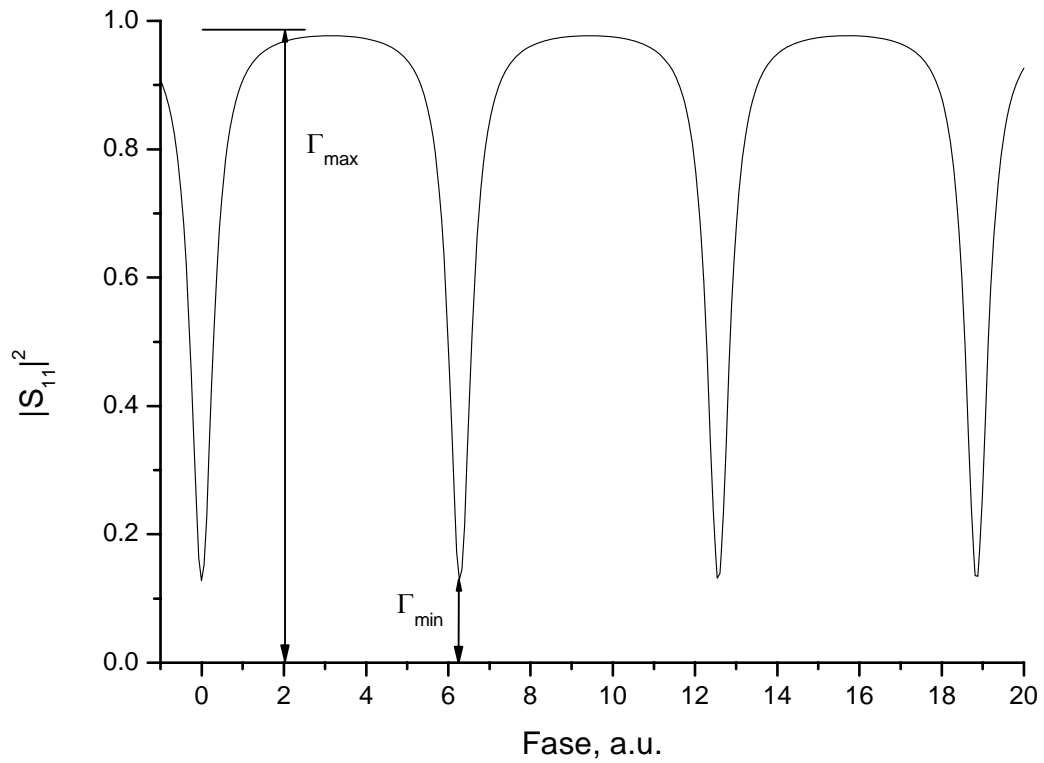
The multi-mode mm-wave resonator can also be described in terms of optical interferometry. In optics a multi-ray Fabri-Perot (FP) type interferometer is a resonator in which build up of electromagnetic energy can occur. This electromagnetic waves energy recirculates inside the interferometer of due to reflections from parallel interferometer mirrors at the end of the resonator (see Fig. 3.15) like in the FEL mm-wave resonator.

$$\delta = 2(\omega n / c)\cos(\theta)L \quad (3.13)$$

From (3.12) we can write explicitly the expressions for the power transmission and reflection coefficients $T = |S_{12}|^2$, $\Gamma = |S_{11}|^2$:



(a)



(b)

Fig. 3.16 Transmitted (a) and reflected (b) power pattern for a Fabry-Perot resonator.

$$T = |S_{12}|^2 = \frac{t_1^2 t_2^2}{(1 - r_1 r_2)^2 + 4r_1 r_2 \sin^2(\delta/2)} \quad (3.14)$$

$$\Gamma = |S_{11}|^2 = \frac{(r_1 - r_2)^2 + 4r_1 r_2 \sin^2(\delta/2)}{(1 - r_1 r_2)^2 + 4r_1 r_2 \sin^2(\delta/2)}$$

The dependence of these parameters on the phase δ for is shown in Fig.3.16. The transmission coefficient exhibits a periodic “comb” pattern of

peaks, spaced apart by $\Delta\delta=2\pi$. The reflection coefficient exhibits a complementary “comb” pattern of dips.

With the notation of the Fig. 3.16 we can define the maximal and minimal values of the reflected power:

$$\Gamma_{\max} = |S_{11}|_{\max}^2 = \frac{(r_1 + r_2)^2}{(1 + r_1 r_2)^2}, \quad \text{for } \delta = 2\pi p + \pi \quad (3.15)$$

$$\Gamma_{\min} = |S_{11}|_{\min}^2 = \frac{(r_1 - r_2)^2}{(1 - r_1 r_2)^2}, \quad \text{for } \delta = 2\pi p, \quad p = 0, 1, 2..$$

and for the transmitted power:

$$T_{\min} = |S_{12}|_{\max}^2 = \frac{t_1^2 t_2^2}{(1 + r_1 r_2)^2}, \quad \text{for } \delta = 2\pi p + \pi \quad (3.16)$$

$$T_{\max} = |S_{12}|_{\min}^2 = \frac{t_1^2 t_2^2}{(1 - r_1 r_2)^2}, \quad \text{for } \delta = 2\pi p, \quad p = 0, 1, 2..$$

Maximum transmission and minimum reflection power are observed simultaneously when the distance between the interferometer mirrors is an integral number p of half-wavelengths. This is a resonance condition. If the distance between mirrors is an odd integer of quarter-wavelengths (electrical length $k*l$ is an integer number of half-wavelengths plus a quarter-wavelength), the antiresonance condition is exist and a minimum of transmission power occurs with a maximum of reflection power.

In the context of this work, we shall extend the FP analytical model to include non symmetrical interferometers (with a lossy medium inside the resonator). The mathematical derivation of this case is given in **Appendix**. According to Eq.(A1.24), Eq.(3.14) can be rewritten as:

$$\Gamma = |S_{11}|^2 = \frac{[r_1 - \tau r_2]^2 + 4\tau r_1 r_2 \sin^2\left(\frac{\delta}{2}\right)}{(1 - \tau r_1 r_2)^2 + 4\tau r_1 r_2 \sin^2\left(\frac{\delta}{2}\right)}; \quad (3.17)$$

$$T = |S_{12}|^2 = \frac{\tau T_1 T_2}{(1 - \tau r_1 r_2)^2 + 4\tau r_1 r_2 \sin^2\left(\frac{\delta}{2}\right)}.$$

where $T_1=(t_1)^2$, $T_2=(t_2)^2$ are the power transmission coefficients. τ is the one way power transmission coefficient in the medium between mirrors (it is assumed that there are no internal reflections). If one assumes uniform losses, along the z -direction, then $\tau = e^{-2\alpha L}$, where α is the field amplitude decay coefficient of the medium. In the extended derivation (**Appendix**) the propagating wave is not necessarily a plane wave, but can be a single transverse mode propagating with wave number k_z . In this case $\delta=2k_z L$ instead of Eq.(3.13). In an overmoded waveguide (as is the case in the FEL CPP resonator), the fundamental mode is satisfies $k_z \approx \frac{\omega}{c} = \frac{2\pi}{\lambda}$. The expressions for maximum transmitted and minimum reflected power for the resonance condition $\delta = 2\pi p$ are then:

$$\Gamma_{\min} = |S_{11}|_{\min}^2 = \frac{[r_1 - \tau r_2]^2}{(1 - \tau r_1 r_2)^2}; \quad (3.18)$$

$$T_{\max} = |S_{12}|_{\max}^2 = \frac{\tau T_1 T_2}{(1 - \tau r_1 r_2)^2}.$$

The antiresonance phase condition $\delta = 2\pi(p+1/2)$ is obtained for minimum transmission and maximum reflection power:

$$\begin{aligned}\Gamma_{\max} &= |S_{11}|_{\max}^2 = \frac{[r_1 + \tau r_2]^2}{(1 + \tau r_1 r_2)^2}; \\ T_{\min} &= |S_{12}|_{\min}^2 = \frac{\tau T_1 T_2}{(1 + \tau r_1 r_2)^2}.\end{aligned}\quad (3.19)$$

The frequency range between transmission maxima (or reflection minima) Δf is called free spectral range (FSR) of an interferometer and is defined in the plane wave model as follows:

$$\Delta f_{FSR} = f_{p+1} - f_p = \frac{c}{2L \cos \Theta} \quad (3.20)$$

For a waveguide mode, the definition is derived from:

$$\begin{aligned}\left[k_z(f_{p+1}) - k_z(f_p) \right] 2L &= \frac{dk_z}{d\omega} (\omega_{p+1} - \omega_p) 2L = 2\pi \\ \Delta f_{FSR} = f_{p+1} - f_p &= \frac{v_g}{2L}\end{aligned}\quad (3.21)$$

For the fundamental mode of an overmoded waveguide $v_g \approx c$ and Eq.(3.20) applies with $\theta = 0$.

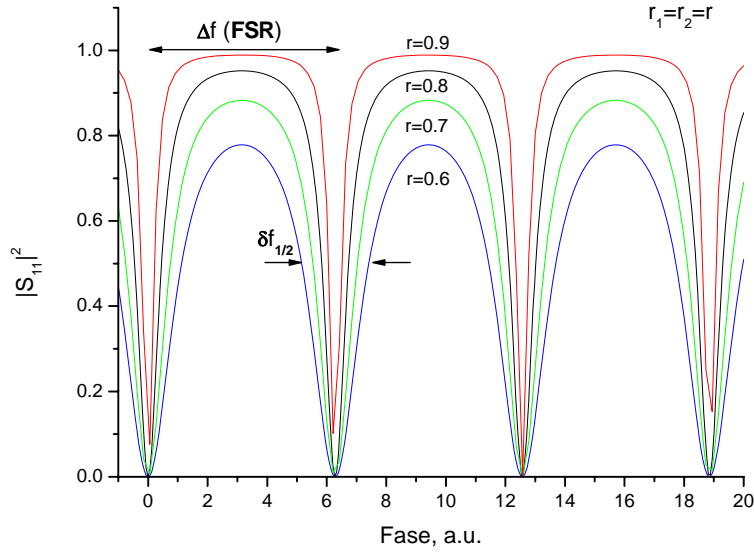


Fig. 3.17 Reflection of an ideal Fabri-Perot interferometer; $r_1 = r_2$.

The width $\delta f_{1/2}$ of the maxima of transmission power (or minima of reflection power) FWHM is defined at the half maximum power level (Fig.3.17)

$$2\pi p \pm \frac{\delta_{1/2}}{2} :$$

$$\sin\left(\frac{\delta_{1/2}}{4}\right) = \frac{1 - \tau r_1 r_2}{2\sqrt{\tau r_1 r_2}} = \frac{1 - \sqrt{R_{rt}}}{2\sqrt[4]{R_{rt}}} \quad (3.22)$$

where $R_{rt} = (\tau r_1 r_2)^2$ is the power round-trip reflectivity factor of the resonator.

By differentiation of δ (Eq.3.13), one obtains

$$\delta f_{1/2} = \frac{v_g}{2L} \frac{\delta_{1/2}}{2\pi}, \quad (3.23)$$

and consequently the FWHM frequency linewidth for transmission or reflection resonance is a function only of Δf_{FSR} and R_{rt} :

$$\delta f_{1/2} = \frac{v_g}{2L} \frac{2}{\pi} \arcsin\left(\frac{1-\sqrt{R_{rt}}}{2\sqrt[4]{R_{rt}}}\right) = \Delta f_{FSR} \frac{2}{\pi} \arcsin\left(\frac{1-\sqrt{R_{rt}}}{2\sqrt[4]{R_{rt}}}\right) \quad (3.24)$$

This expression is valid even if there are large round-trip losses. In most cases ($1 > R_{rt} > 0.5$) it is a good approximation: one can for these cases expand the *arcsin* function to first order in terms of its argument:

$$\delta f_{1/2} = \Delta f_{FSR} \left(\frac{1-\sqrt{R_{rt}}}{\pi\sqrt[4]{R_{rt}}} \right) \quad (3.25)$$

This can be expressed in terms of the "Finesse" parameter, which is the optical term for describing the sharpness of the interferometer:

$$\mathfrak{F} = \frac{\Delta f_{FSR}}{\delta f_{1/2}} = \pi \frac{\sqrt[4]{R_{rt}}}{1-\sqrt{R_{rt}}} \quad (3.26)$$

In a lossless symmetric resonator $(r_1)^2 = (r_2)^2 = R$ and $R_{rt} = R^2$. For this case only:

$$\mathfrak{F} = \pi \frac{\sqrt{R_{rt}}}{1-R_{rt}} \quad (3.27)$$

which is the expression given in [1].

3.5.2 The Q-factor of a Fabri-Perot cavity resonator

We now make the connection between the optical characterization and microwave parameters of resonators. As discussed in section 3.6, for isolated modes, the resonator can be characterized by the quality parameter Q. We choose here to define the Q-factor as the ratio between the frequency f_0 (resonant wavelength λ_0) and bandwidth of the resonator mode $\delta f_{1/2}$ (or $\delta \lambda_{1/2}$):

$$Q = \frac{f_0}{\delta f_{1/2}} = \frac{\delta \lambda_{1/2}}{\lambda_0} \quad (3.28)$$

Consequently,

$$Q = \frac{f_0}{\Delta f_{FSR}} \mathfrak{F} = \frac{f_0 L}{v_g} \frac{\pi}{\arcsin \left[\left(1 - \sqrt{R_{rt}} \right) / 2 \sqrt[4]{R_{rt}} \right]} \quad (3.29)$$

and, for small round-trip losses ($R_{rt} \sim 1$):

$$Q = \frac{f_0}{\Delta f_{FSR}} \mathfrak{F} = \frac{2\pi f_0 L}{v_g} \frac{\sqrt[4]{R_{rt}}}{1 - \sqrt{R_{rt}}}. \quad (3.30)$$

If $v_g = c$ then a simple relation appears:

$$Q = \frac{2\pi L}{\lambda} \frac{\sqrt[4]{R_{rt}}}{1 - \sqrt{R_{rt}}} = \frac{L}{\lambda/2} \mathfrak{F}. \quad (3.31)$$

It should be noted that in Eq.(3.31) above Q is **the loaded Q-factor** since both internal and external (coupling mirror) losses are included.

3.5.3 Determination of the round-trip reflectivity parameter from measured resonance linewidth

The round-trip resonator reflectivity is the significant resonator parameter affecting the laser performance, as it defines the needed threshold gain G_{th} (and in the case of FEL-threshold current) for the lasing condition: $G_{th}R_{rt} = 1$. A round-trip reflectivity parameter can be defined based on the spectral linewidth of the resonant curve of power obtained from the resonator.

Let us defined a new parameter

$$\bar{C} = \sin\left(\frac{\pi\delta f_{1/2}L}{v_g}\right) \approx \frac{\pi\delta f_{1/2}L}{v_g} \quad (3.32)$$

or, in terms of the parameter Q (defined as $Q = \frac{f_0}{\delta f_{1/2}}$):

$$\bar{C} = \sin\left(\frac{\pi f_0 L}{v_g Q}\right) \approx \frac{\pi f_0 L}{v_g Q} \quad (3.33)$$

The parameter \bar{C} (Eq.3.32) can always be evaluated from the measurable parameter $\delta f_{1/2}$. Substituting Eq.(3.31) results in an exact expression from which R_{rt} can be evaluated:

$$\bar{C} = \sin\left(\frac{1-\sqrt{R_{rt}}}{\sqrt[4]{R_{rt}}}\right) \approx \frac{1-\sqrt{R_{rt}}}{2\sqrt[4]{R_{rt}}} \quad (3.34)$$

For a given value of \bar{C} , this is a fourth order algebraic equation in terms of $x \equiv \sqrt[4]{R_{rt}}$. It can be readily solved; the only physically meaningful solution is

$x_1 = -\bar{C} + \sqrt{(\bar{C})^2 + 1}$. Thus, we have an explicit equation:

$$R_{rt} = x_1^4 = \left[-\bar{C} + \sqrt{(\bar{C})^2 + 1} \right]^4 \quad (3.35)$$

which together with (3.32) - (3.33) makes it possible to calculate R_{rt} in terms of Q or directly in terms of $\delta f_{1/2}$. In the approximation (3.33) ($R_{rt} > 0.5$; $v_g = c$), this can be rewritten:

$$R_{rt} = \left[-\frac{2\pi L}{\lambda_g Q_{loaded}} + \sqrt{\left(\frac{2\pi L}{\lambda_g Q_{loaded}} \right)^2 + 1} \right]^4 = \left[-\frac{2\pi L \delta f_{1/2}}{v_g} + \sqrt{\left(\frac{2\pi L \delta f_{1/2}}{v_g} \right)^2 + 1} \right]^4 \quad (3.36)$$

The total round-trip reflectivity R_{rt} of the FEL resonator was calculated in the present work based on Eq.(3.36) and direct measurement of the FWHM linewidth $\delta f_{1/2}$ of the resonant peaks. This linewidth was obtained from measurement of the power spectral reflection pattern.

3.5.4 Determination of the coupling transmission coefficient from measured spectral reflection pattern

As we have shown, a measurement of the resonator linewidth $\delta f_{1/2}$ (or $Q = f_0 / \delta f_{1/2}$) determines completely the round-trip parameter $R_{rt} = \tau^2 R_1 R_2$. However, it does not enable the determination of the three reflectivity factors separately, and in particular of R_1 . This parameter is of interest, because it can be used to calculate the coupling mirror transmission coefficient, which is given (assuming zero losses in the mirror) by:

$$T_1 = 1 - R_1 \quad (3.37)$$

A possible way to determine the parameter R_1 in addition to R_{rt} is to match the entire theoretical reflection pattern given by Eq.(3.14) and particularly the extreme points Eqs.(3.18)-(3.19) to the measured reflection comb pattern. The expressions for the reflection pattern and its extreme points are rewritten here in a revealing way in terms of only two parameters R_1 and R_{rt} :

$$\Gamma = 1 - \frac{(R_1 - R_{rt})(1 - R_1) / R_1}{(1 - \sqrt{R_{rt}})^2 + 4\sqrt{R_{rt}} \sin^2(\delta/2)} \quad (3.38)$$

$$\Gamma_{\min} = \frac{(R_1 - R_{rt})^2}{(1 - \sqrt{R_{rt}})^2} \frac{1}{R_1} \quad \text{for } \delta = 2m\pi$$

$$\Gamma_{\max} = \frac{(R_1 + R_{rt})^2}{(1 + \sqrt{R_{rt}})^2} \frac{1}{R_1} \quad \text{for } \delta = (1 + 2m)\pi \quad (3.39)$$

This technique was difficult to employ (in our case) because of the difficulty in measuring the reflection pattern (due to attenuation and parasitic reflections in the probing transmission line (Figs.3.5, 3.6), and because the dip of the function $\Gamma_{\min}/\Gamma_{\max}$ is quite shallow if one is far from the “critical coupling” condition $R_1 = \sqrt{R_{rt}}$).

If one could measure the coupling mirror reflection coefficient R_1 independently and vary it in a wide range, then one could determine the internal round-trip reflectivity (namely, the reflectivity when $R_1=1$):

$$R_{\text{int}} = R_2 \tau^2 \quad (3.40)$$

and, consequently, the internal loss factor:

$$L_{\text{int}} = 1 - R_{\text{int}} \quad (3.41)$$

This can be done by measuring R_{rt} for a large range of R_1 which would effect significantly $\delta f_{1/2}$, and then determine R_{int} by extrapolation of the data to $R_1 \rightarrow 1$.

If R_1 could be varied in a wide range, then one could independently determinate R_1 and R_{rt} (and consequently R_{int}). This can be done by successive measurements of Γ_{min} (3.15) for different R_1 . In particular, determination of R_{int} is attained at the critical coupling condition:

$$R_1 = \sqrt{R_{\text{rt}}} = R_{\text{int}} \quad (3.42)$$

for which the reflection coefficient is null: $\Gamma_{\text{min}} = 0$.

It is now proper to refer back to the lumped circuit model, and to check to what extent is the expression (3.2) valid in view of the more accurate optical model results:

$$\frac{1}{Q_{\text{loaded}}} = \frac{1}{Q_0} + \frac{1}{Q_{\text{ext}}} \quad (3.2)$$

In the limit of high Q (low losses), Eq.(3.36) can be expanded to first order in $\frac{\pi L}{\lambda Q}$,

resulting in a linear relation between $1/Q$ and $(1-R_{\text{rt}})$. In particular:

$$\frac{1}{Q_{\text{loaded}}} = \frac{1 - R_{\text{rt}}}{8\pi L / \lambda} \quad (3.43)$$

This expression is valid only if:

$$\bar{C} = \frac{2\pi L / \lambda}{Q_{\text{loaded}}} = \frac{1}{4}(1 - R_{\text{rt}}) \ll 1. \quad (3.44)$$

In this limit the multiplicative relation between $R_{\text{int}} = R_2\tau^2$ and $R_{\text{ex}} = R_1$ can be written as an additive relation:

$$\begin{aligned} 1 - R_{rt} &= 1 - R_{\text{int}} R_{\text{ext}} = 1 - [1 - (1 - R_{\text{int}})] [1 - (1 - R_{\text{ext}})] \\ &\approx (1 - R_{\text{int}}) + (1 - R_{\text{ext}}) \end{aligned} \quad (3.45)$$

and consequently

$$\frac{1}{Q_{\text{loaded}}} = \frac{1}{Q_{\text{int}}} + \frac{1}{Q_{\text{ext}}} \quad (3.46)$$

where

$$\frac{1}{Q_{\text{int}}} = \frac{1 - R_{\text{int}}}{8\pi L / \lambda}, \quad \frac{1}{Q_{\text{ext}}} = \frac{1 - R_{\text{ext}}}{8\pi L / \lambda} \quad (3.47)$$

For critical coupling condition the exact expression $R_{\text{int}} = R_{\text{ext}}$ reduces (see Eq.(3.47).) to the expression $Q_{\text{int}} = Q_{\text{ext}}$, which is correct only for low losses.

We therefore conclude that use of the lumped circuit model (Eq.(3.43)) for determination of the parameters R_{int} and R_{ext} (Eqs.(3.47)) is valid only if special care is taken to satisfy condition (3.44).

3.5.5 Adaptation of the Fabri-Perot model to the experimental setup

A definition of round-trip resonator reflectivity for a model of several Fabri-Perot resonators in series including attenuation due to internal surfaces imperfections and due to local losses at different points, is given by:

$$R_{rt} = R_1 \cdot R_2 \cdot T_1 \cdot T_2 \cdot T_3 \dots \quad (3.48)$$

Note that T_i is the one-way transmission attenuation factor of an electromagnetic (EM) field pattern corresponding to the TE_{01} mode only. Local reflections and excitation of EM fields in higher order waveguide modes are considered as losses. For the FEL resonator investigated, the local losses in the bend region, for instance, can be included in the total reflectivity as follows:

$$R_{rt} = R_1 R_2 e^{-4\alpha l} T_{bend}^2 \quad (3.49)$$

Here T_{bend} also corresponds only to attenuation of the field pattern that is used eventually to reconstruct the TE_{01} mode. Other field components generated by diffraction at the bend, as higher order modes, are considered as losses.

Due to impedance mismatches between the RF source and the feed line before the resonator, reflections in the section between R_1' and R_2' (Fig. 3.18) may be treated as occurring in a low-Q FP interferometer with almost transparent mirrors.

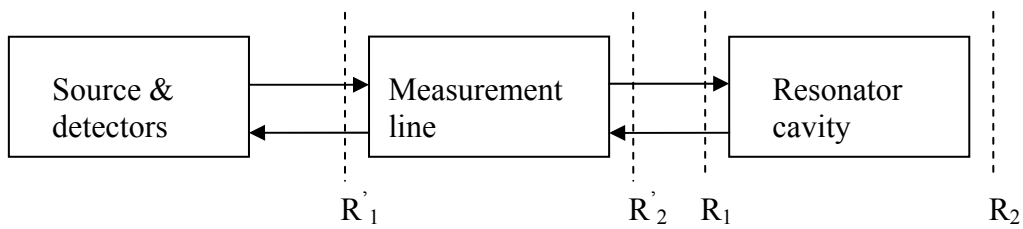


Fig. 3.18 Measurement transmission line terminated by a RF source and by resonator cavity at each end respectively.

We consider two Fabri-Perot interferometers in series assembled into a unified system with one common mirror between them (Fig. 3.19). This scheme describes the typical setup for reflection coefficient measurement.

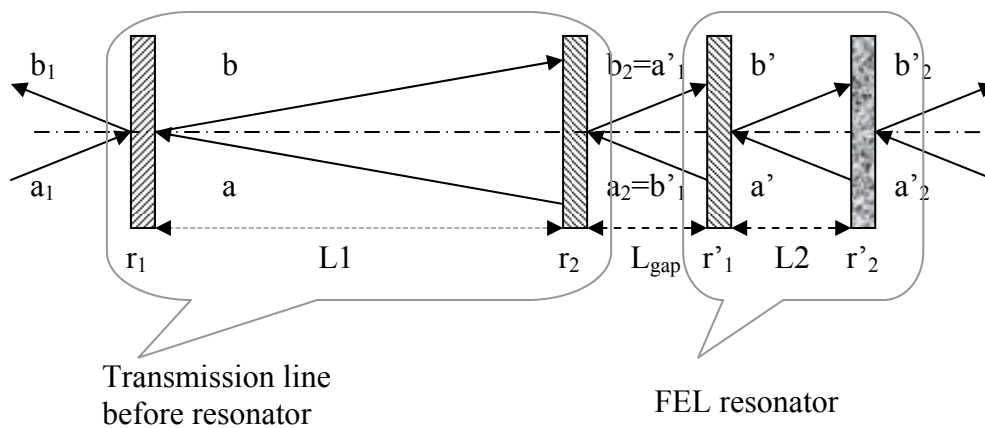


Fig. 3.19 Two Fabri-Perot interferometers in serial.

The first two mirrors r_1 and r_2 of Fig.3.19 are part of a complex transmission line from the RF generator to the reflecting grids before entrance to the resonator. This system includes two calibrated detectors, a mode exciter which transforms the TE_{10} mode of the rectangular waveguide to the desired mode of the corrugated cylindrical

waveguide; it also includes a parabolic mirror that provides matching between the output of the resonator and the transmission line separated from it by free space.

The second pair of mirrors are part of the FEL resonator. According to the definition above, the letters with apostrophe refers to the FP #2 (FEL resonator) and letters without apostrophe are related to FP #1 (entire transmission line). To combine these two FP resonators in an appropriate model, we assume that:

- The rear mirror of the FP#2 has a reflection coefficient $r'_2=1$ therefore the whole incident energy is reflected back.
- Two resonators can be joined by eliminating the gap between them: $L_{\text{gap}}=0$.
- We define $r_2=0$ opening the first resonator and we terminate it by the second resonator. Therefore we use actually three mirrors only: r_1 , r'_1 , and r'_2 . The mirror r'_1 is common to both FP resonators.
- For consistency of boundary conditions we also put $b_2=a'_1$ and $a_2=b'_1$.

We can measure directly the reflection coefficient $\Gamma = b_1/a_1$, experimentally and compare it with the theoretical curve. Taking into account the symmetry properties (duality) of the scattering matrix $s_{12}=s_{21}$, we get:

$$\Gamma = s_{11} + \frac{s_{12}^2 s'_{11}}{1 - s_{22} s'_{11}} \quad (3.50)$$

An additional verification of the approximation used for obtaining round-trip reflectivity was made by applying the model of several FP interferometers in series as described early above. The reflection pattern for two FP interferometers in series obtained from Eq.(3.50) was compared with the measured reflectivity pattern. For each waveguide section of the resonator and for its feed line differing appropriate propagation constants and actual values of mirrors reflectivity were used. The result is $R_{\text{rt}}=52\%$ of round-trip reflectivity calculated by Eq.(3.49). There is good agreement between the simulation and the Lorentzian approximation used above. Comparison of

theoretical curves for our parameters and the measured reflectivity data is shown in Fig.3.20:

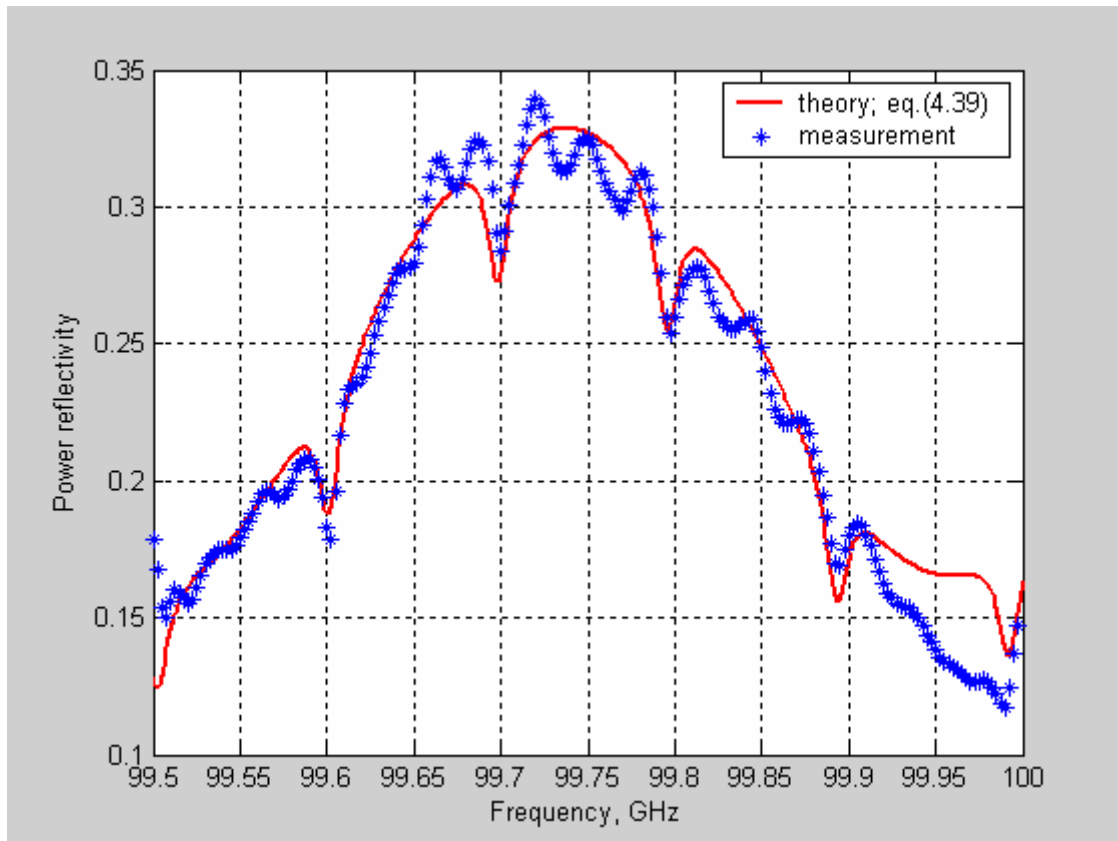


Fig.3.20 Reflectivity of two FP interferometers in series.

3.5.6 Operation of the Fabri-Perot resonator in the oscillation regime of the FEL

Inspection of Eq. (3.38) reveals that it is easy to generalize this expression so as to make it applicable for the case where we measure the reflection from the resonator in the presence of FEL gain G . This can be of interest in FEL development as a way for determine both the resonator losses (or round-trip reflectivity R_{rt}) and the FEL gain from the measured reflectivity pattern below lasing condition, namely $R_{rt}G < 1$.

The reflectivity expression in the presence of gain can be derived straightforwardly by substituting $R_{rt}G$ instead of R_{rt} in Eq. (3.38):

$$\Gamma = \frac{\left(r_1 - \frac{\sqrt{R_{rt} * G}}{r_1} \right)^2 + 4 * \sqrt{R_{rt} * G} * \sin^2(\delta/2)}{\left(1 - \sqrt{R_{rt} * G} \right)^2 + 4 * \sqrt{R_{rt} * G} * \sin^2(\delta/2)} \quad (3.51)$$

Accordingly to Eq.(3.39) the minimum reflection condition is:

$$\Gamma_{\min} = \frac{\left(R_1 - \sqrt{R_{rt}G} \right)^2}{\left(1 - \sqrt{R_{rt}G} \right)^2} \frac{1}{R_1} \quad \text{for } \delta = 2m\pi \quad (3.52)$$

For $R_{rt}G = 1$ power accumulates in the resonator without an input signal (the resonator becomes self-excited). This regime of operation is also called the oscillation regime. As the FEL gain parameter G is increased, internal losses of the resonator are “compensated” until the oscillation condition $G > 1/R_{rt}$ is satisfied. Several curves of reflected power at the resonant frequency for the various values of gain G are shown in Fig. 3.21 :

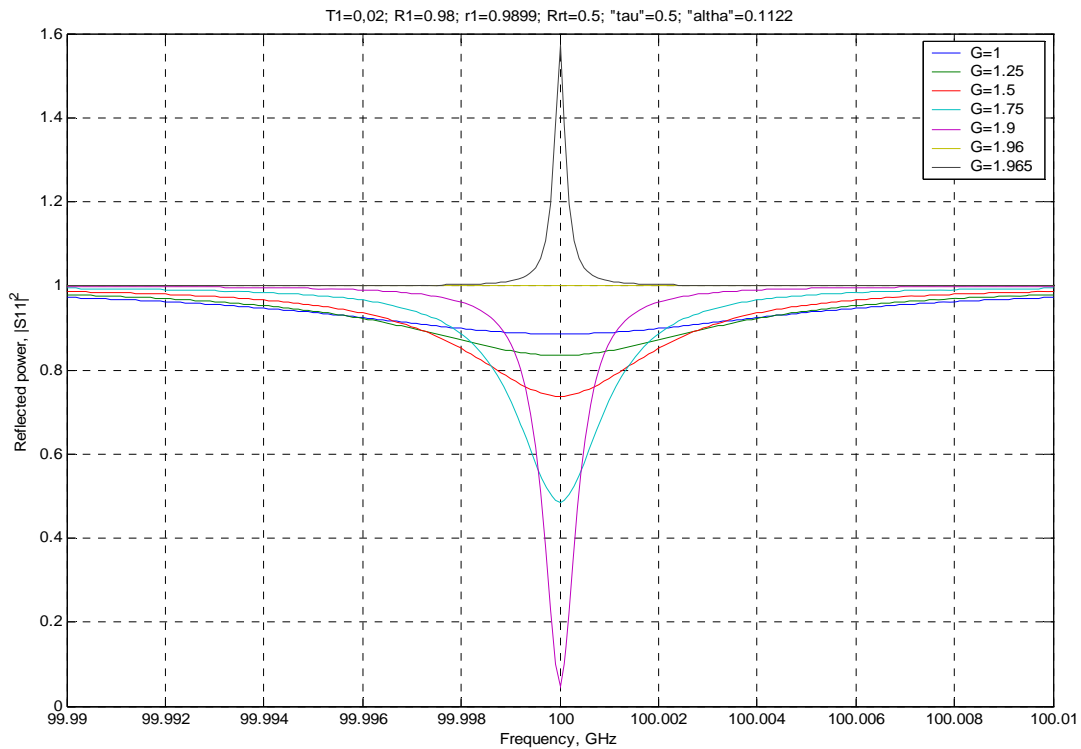


Fig. 3.21 Resonant peak of reflected power for several gain values for parameters $R_{rt}=0.5$, $R_1=0.98$.

It can be seen in this figure that a critical coupling condition near 100GHz is reached for $G = 1$. Up to the point of critical coupling the measured dip of the reflected power increases (!) as the gain is increased. When the gain increases beyond the critical coupling point the dip becomes smaller. It then turns into a peak ($G = 1.965$), and explodes when $G = 1/R_{rt} = 2$. Measurement of the power spectral reflection pattern while passing current through the FEL, can be a way for measuring the FEL gain before oscillation threshold. However, this requires being able to measure R_{rt} .

References

1. Yariv A., *Introduction to Optical Electronics*. Holt, Rinehart and Winston, New York, 1976.
2. Collin Robert E., *Foundations for microwave engineering*. 2nd ed. McGraw-Hill, 1992.
3. Ulrich R., Bridge T.J. and Pollack M.A., *A variable Output Coupler for Far Infrared Lasers*. Proc. Symp. On Submillimeter Waves, Polytechnic Inst., Brooklin, 605-614, 1970.
4. Saleh A.A.M., *An adjustable quasi-optical bandpass filter – part1: theory and design formulas*. IEEE Trans. MTT, vol. 22, no.7, pp.728-734, 1974.
5. Cornbleet S., *Microwave optics*. Academic press, 1976.
6. **Yulia&Yakover Internal report**
7. Haus H., *Waves and Fields in Optoelectronics*. Prentice-Hall, 1984.
8. Fox A.G. and Li T., *Resonant Modes in a Maser Interferometer*. The Bell System Technical Journal, March, 1961.
9. Culshaw W., *Reflectors for a Microwave Fabri-Perot Interferometer*. IRE Trans. On Microwave and Theory Techniques, vol.MTT-7, pp.182-189; April, 1959.
10. Culshaw W., *High Resolution Millimeter Wave Fabri-Perot Interferometer*. IRE Trans. On Microwave and Theory Techniques, vol.MTT-8, pp.182-189; March, 1960.
11. Faingersh A., Gover A., Eliran A., Kapilevich B. *Concluding report: Measurements and calculation of round-trip reflectivity in the FEL waveguide resonator before and after modification and estimate of threshold current improvement*. Internal report of FEL group, 9-Feb-06, Tel-Aviv University.

12. Yakover I., Pinhasi Y., Gover A. *Study of waveguide resonators for FEL operating at submillimeter wavelengths*. Nuclear Instr. And Methods in Physics Research, A 375, (1996), 260-263.
13. Nakahara T., Kurauchi N., *Guided beam waves between parallel concave reflectors*. IEEE Transactions of Microwave Theory and Techniques, v.MTT-15, no2 (1967), p.66.
14. Lurie Y., *Parallel Curved Plates (PCP) versus rectangular waveguide*. Internal report of FEL group, 14-March-02, Tel-Aviv University.
15. Papas ...
16. Kazantsev Yu.N., Sov. Radio Eng. Elec. Phys., 15 (1970), p.963
17. Vaganov
18. Anaton A., Markish O.,
19. Ginzton E. L., *Microwave Measurements*. New York: McGraw-Hill, 1957, Chap. 9.
20. Lebedev
21. Altman
22. A. Asija and A. Gundavajhala, *Quick measurement of unloaded Q using a network analyzer*, *Rf Design*, pp. 48-52, October 1994.
23. M. Sucher, and J. Fox (eds.), *Handbook of Microwave Measurements*. New York: Polytechnic Press, 1963, Chapter
24. G. L. Matthaei, L. Young and E. M. T. Jones, *Microwave Filters, Impedance-Matching Networks, And Coupling Structures*. New York: McGraw-Hill, 1964, Chapter 11.
25. D. Kajfez and E. J. Hwan, Q-factor measurement with network analyzer, *IEEE Trans. Microwave Theory Tech.*, vol. MTT-32, pp. 666-670, July 1984.
26. Abramovich A, Pinhasi Y, Yakover YM, Gover A, Sokolowski JS, Canter M. *Study of radiation build up and mode evolution in the Israeli electrostatic accelerator free-electron laser oscillator* [Journal Paper], IEEE Transactions on Plasma Science, vol.27, no.2, April 1999, pp.563-7. Publisher: IEEE, USA.
27. Sokolowski JS, Abramovich A, Arensburg A, Chairman D, Draznin M, Eichenbaum AL, Gover A, Kleinman H, Pinhasi Y, Yakover YM, Rosenberg A, Shiloh J, Cohen N, Levin LA, Shahal O. *First lasing of the Israeli tandem*

electrostatic accelerator free electron laser [Conference Paper], Proceedings of the 1997 Particle Accelerator Conference (Cat. No.97CH36167). IEEE. Part vol.1, 1998, pp.906-8 vol.1. Piscataway, NJ, USA.

Chapter 4

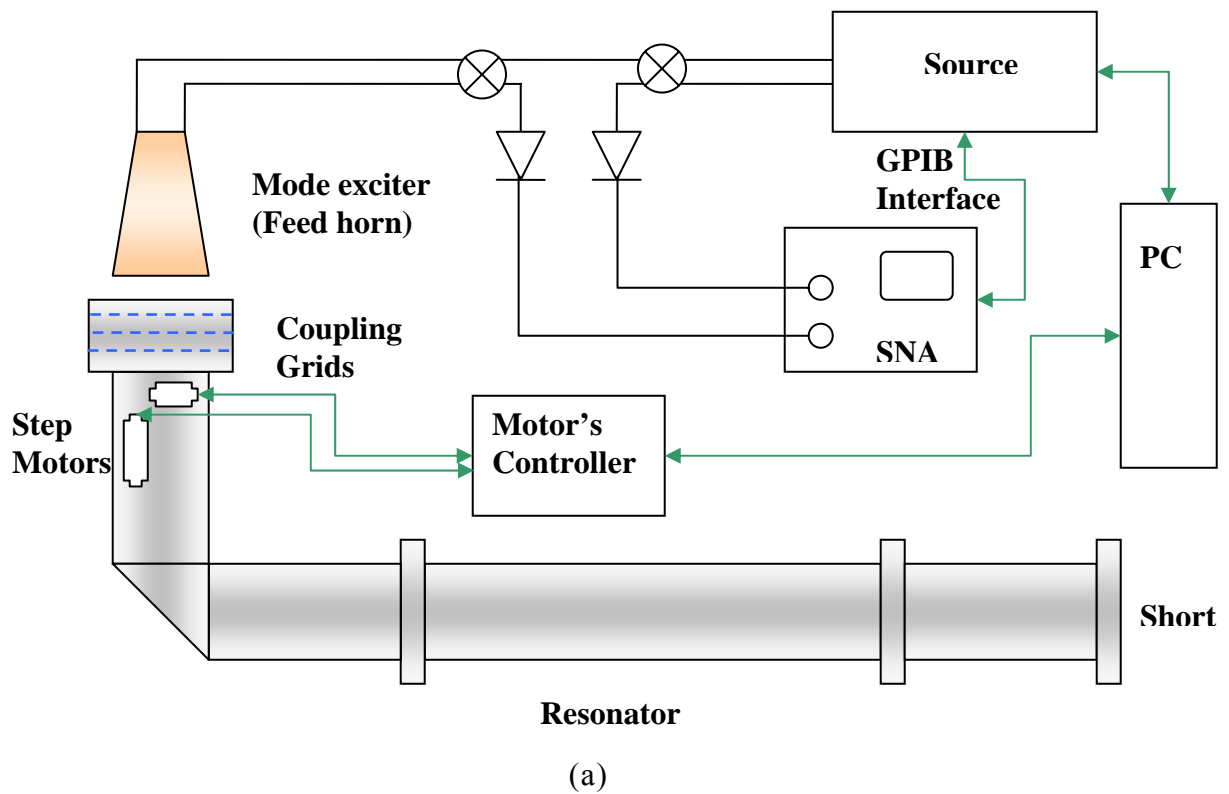
Measurement of round-trip reflectivity

4.1 Introduction

Two procedures which I used in the laboratory for measurement of the round-trip reflectivity of the resonator are described in this chapter. After installation of one resonator into the FEL system, a duplicate resonator was assembled in a separate laboratory in order to enable a concurrent experimental investigation of the resonator system outside the FEL tank. Firstly the round-trip reflectivity of this duplicate resonator was measured using the specially designed remote-controlled motorized 3-grid reflector described in the previous chapter. In a second experiment the round-trip reflectivity of the resonator installed in the laser tank was measured using excitation through a parabolic off-axis mirror. In both experiments, the reflected signal from the excited resonator cavity was measured directly and the round trip reflectivity was calculated according to the theory presented in the previous subchapter.

4.1.1 First experiment: measurements on the duplicate resonator system

The measurement setup is shown in Fig.4.1. It consists of two main parts. In the shorted resonator system, the bent reflector was equipped with two remote-controlled stepped motors, which can cause the reflector grids system to be moved in two planes. Motion of the grid system along the z-axis of the resonator changes the length of the resonator cavity and allows fine-tuning the resonator to a desired frequency. Rotation of the grid system in the x-y plane allows continuous fine variation of the coupling between the cavity and the excitation system so that the desired operation regime of the resonator is achieved (critical coupling for example). The RF excitation section was assembled from a feed horn mode exciter with an aperture that provides excitation of a mode, which is the operating mode.





(b)

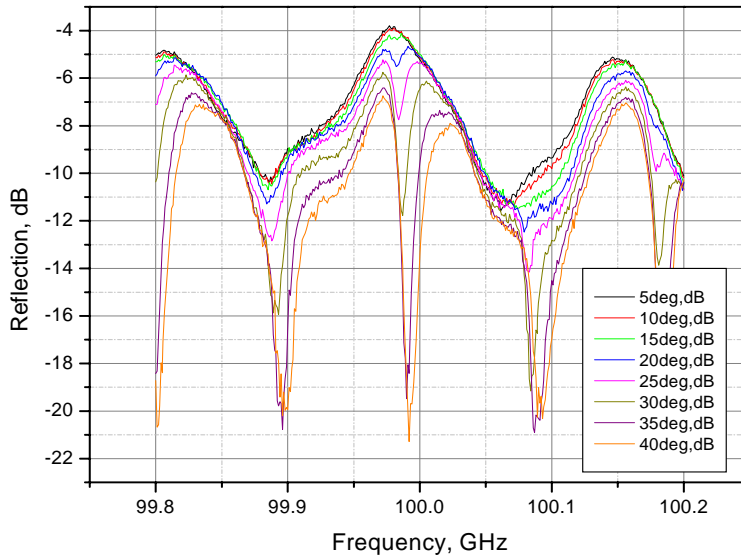
Fig.4.1 (a) Experimental setup for measurement of the resonator, excited by an appropriate aperture: setup diagram; (b) photograph of the experimental setup.

The measured reflected signal patterns for various coupling coefficients (different polarization angle θ of the central grid) are shown in Fig. 4.2 (a).

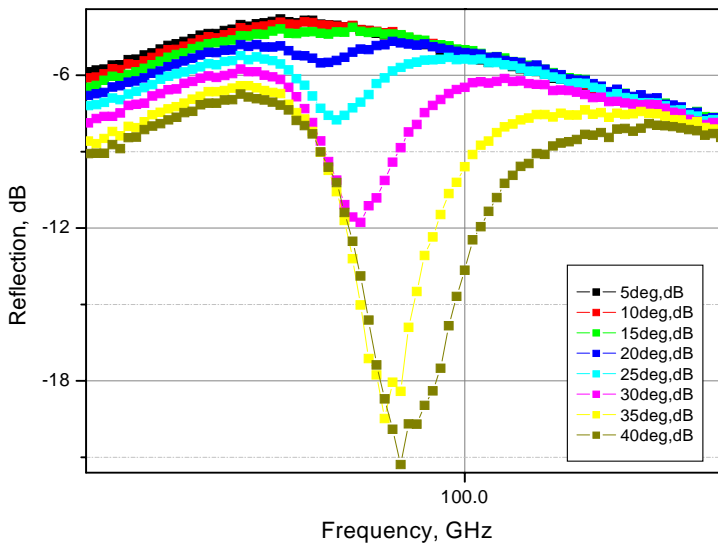
Stronger coupling deepens the absorption resonant peaks. The deepest peaks are obtained for the critical coupling condition; the condition for which the impedance of the cavity is fully matched to the external circuit impedance.

The effect of the longitudinal shift of the coupler mirror (change of the length of the cavity) is shown of Fig. 4.2 (c). It demonstrates the possibility of a frequency shift in a

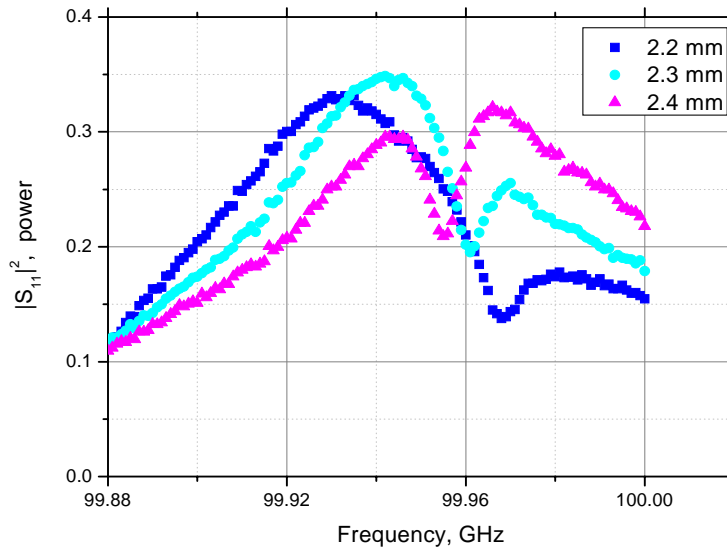
longitudinal mode (resonant peaks at different coupler positions along the z-axis of the resonator).



(a)



(b)



(c)

Fig.4.2 (a) Dependence of the reflection pattern of the resonator on the central grid angle in the coupler; (b) zoom on a single resonant peak; (c) frequency shift of the resonant peak for the different longitudinal coupler positions.

4.1.2 Second experiment: reflection measurements the resonator installed in the FEL system

In these experiments the resonator was excited through a 50 cm long section of a corrugated cylindrical waveguide (see Fig.3.5 (b)). A specially made mode exciter connects this waveguide to the standard W-band waveguide of the Scalar Network Analyzer (SNA). The mode exciter is designed so as to excite in the

corrugated waveguide only the fundamental linearly polarized EH_{11} "improper" mode. This mode has a profile which is very close to that of the free space TEM_{00} linearly polarized Gaussian mode. The Gaussian mode is excited at the waveguide end with an optical coupling efficiency of 97%. This Gaussian mode is then focused and injected into the resonator cavity through an off-axis parabolic mirror which was designed and positioned to generate a Gaussian beam waist onto the resonator 3-grid coupler as shown in Fig. 4.3:

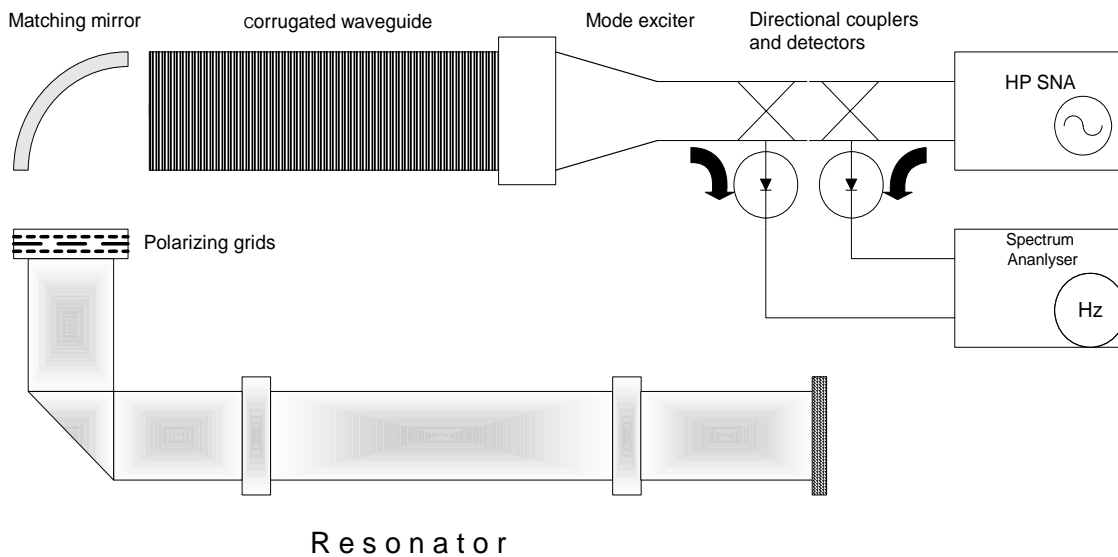
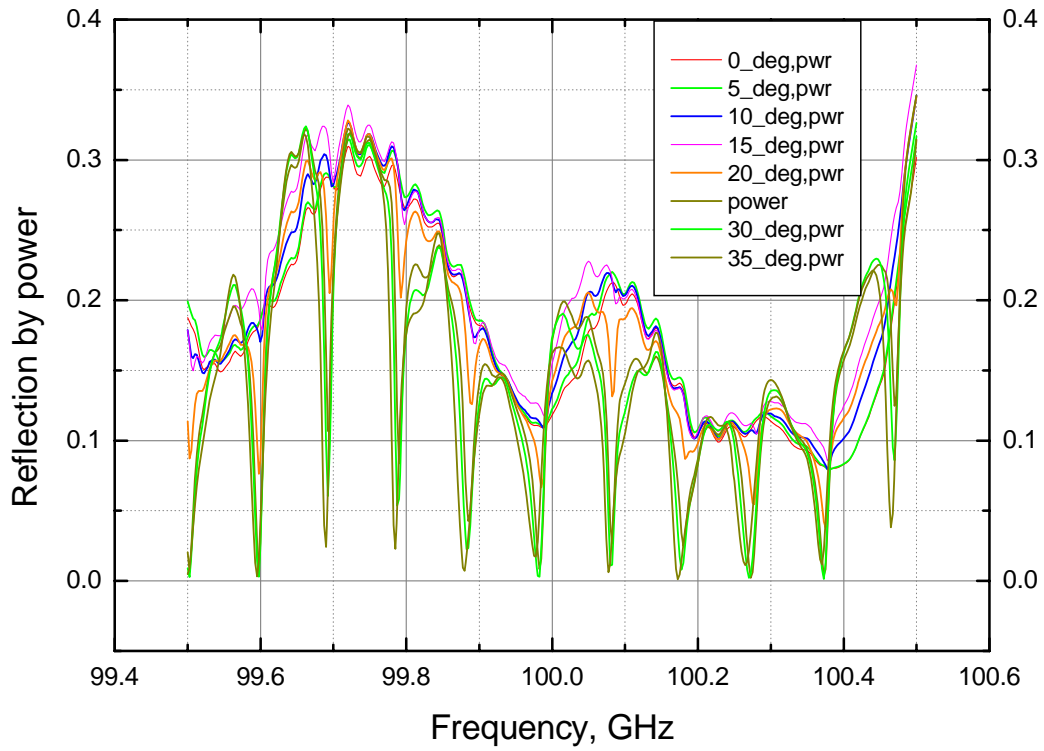


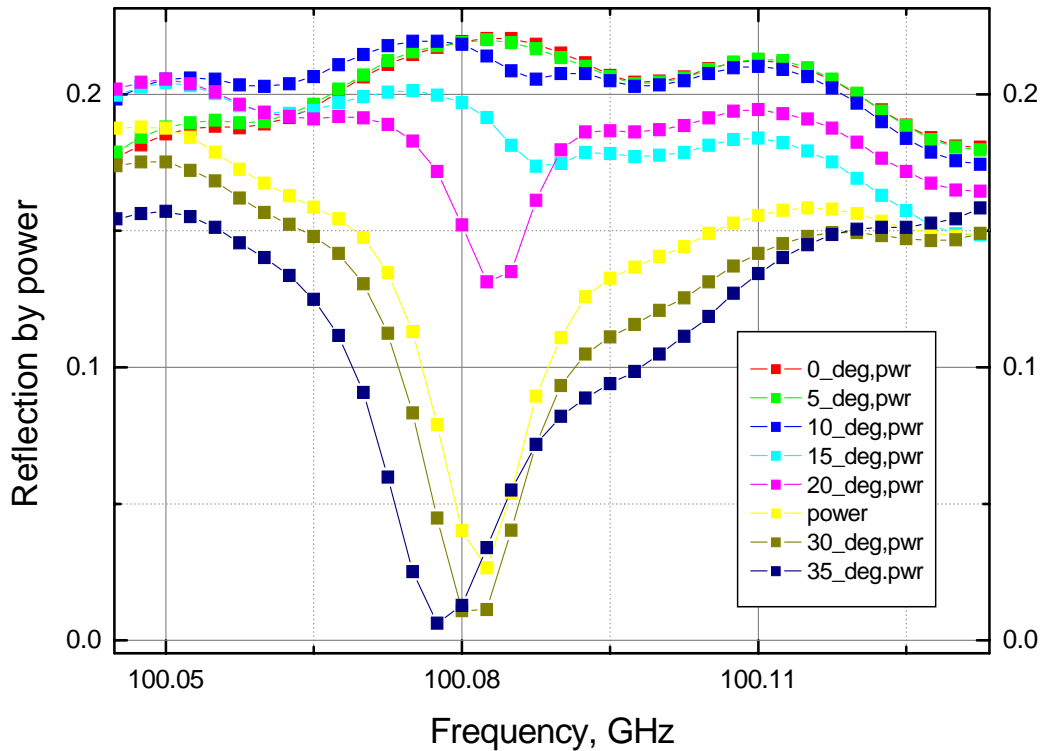
Fig. 4.3 Setup for resonator reflectivity measurement inside the FEL tank.

The coupling coefficient of the polarizing grids mirror was controlled by the angle of the middle polarizing grid (see sub-chapter 3.5) and could be varied within a wide range

by manually changing the angle in the range 0...to 50 degree in steps of 5 degrees. The measured reflection coefficient from the real resonator for several coupler grid angle values is shown in Fig. 4.4:



(a)



(b)

Fig. 4.4 Reflection from the resonator cavity measured for different coupling coefficients: (a) In a wide frequency range; (b) blow-up of a single resonant longitudinal mode dip of the resonator in Fig. 4.4(a).

As shown in Fig. 4.4, the resonant peaks ride on a “parasitic”, “low-frequency” envelope due to the high-loss transmission line section preceding the resonator.

The subsequent analysis of the measured data, obtained in both of the experiments described above, includes extraction of the deconvolved resonance dips from the reflection pattern and evaluation of the Q-factor and round-trip reflectivity parameter of the resonator in a wide frequency range around 100 GHz.

4.2 Analysis of measured data

According to the theory detailed in the **subchapter 3.6**, the algorithm of the round trip reflectivity is based on measurement of the reflection coefficient resonance curve and uses “optical” formulation. The reflection coefficient of the asymmetric Fabri-Perot resonator is (Eq.(3.60)):

$$\Gamma = 1 - \frac{(R_1 - R_r)(1 - R_1)/R_1}{(1 - \sqrt{R_r})^2 + 4\sqrt{R_r} \sin^2\left(\frac{\delta}{2}\right)} \quad (4.1)$$

According to Eqs.(3.36) - (3.37), R_r can be calculated from

$$R_r = X_1^4 = \left[-\bar{C} + \sqrt{(\bar{C})^2 + 1} \right]^4 \approx \left[-\frac{\pi d}{\lambda Q_L} + \sqrt{\left(\frac{\pi d}{\lambda Q_L} \right)^2 + 1} \right]^4 \quad (4.2)$$

or directly in terms of the parameter $\delta f_{1/2}$:

$$R_r = \left[-\frac{\pi d \delta f_{1/2}}{c} + \sqrt{\left(\frac{\pi d \delta f_{1/2}}{c} \right)^2 + 1} \right]^4 \quad (4.3)$$

Because of the presence of a “parasitic pattern” in the measured reflectivity data and because of its frequency dependence, the procedure for determination of FWHM ($\delta f_{1/2}$) described in section 3.6.1 is used. To reduce errors using that procedure, we match the measured resonant dip pattern to a Lorentzian curve:

$$y = y_0 + \frac{2A}{\pi} \frac{w}{4(x - x_c)^2 + w^2} \quad (4.4)$$

The notation used in Eq. (4.4) is described in Fig. 4.5:

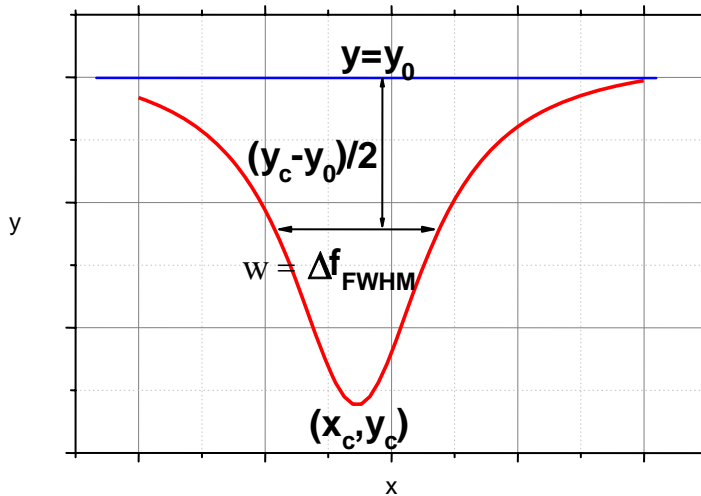


Fig. 4.5 The Lorentz curve approximation: y_0 – off-set of Lorentzian curve;
 x_c, y_c – coordinates of the resonant maxima; $\Delta f_{\text{FWHM}} = \delta f_{1/2} = w$ – width of the
 resonance peak at -3dB level $(y_c - y_0)/2$;

In order to match the dip patterns of the exact Fabry-Perot comb (Eq.(3.17)) to a Lorentzian curve (at least in the frequency range $|f - f_0| < \delta f_{1/2}$) it is necessary to satisfy:

$$\bar{C} = \sin\left(\frac{2\pi l}{c} \delta f_{1/2}\right) \approx \frac{2\pi l}{c} \delta f_{1/2} \ll 1 \quad (4.5)$$

or, in terms of Q_L ,

$$\bar{C} = \sin\left(\frac{2\pi l}{\lambda Q_L}\right) \approx \frac{2\pi l}{\lambda Q_L} \ll 1 \quad (4.6)$$

In terms of the optical parameter of the *Finess*, this inequality states $F \gg \pi$ which usually is easily satisfied for good quality resonators.

For the parameters of our resonator system and for a typical value $\delta f_{1/2} \approx 10$ MHz we get:

$$\bar{C} \approx \frac{2\pi l}{c} \delta f_{1/2} = 0.314 \ll 1 \quad (4.7)$$

which justifies the Lorentzian curve approximation.

In Fig.4.6 we plot the parameter \bar{C} vs. the exact dependence of the FWHM frequency with $\delta f_{1/2}$ of a FP interferometer resonant pattern (first equality in Eq.(4.6)). For comparison we plot also the approximate dependence (second equality in Eq.(4.6)). Evidently, the approximation is very good for $\delta f_{1/2} = 10$ MHz.

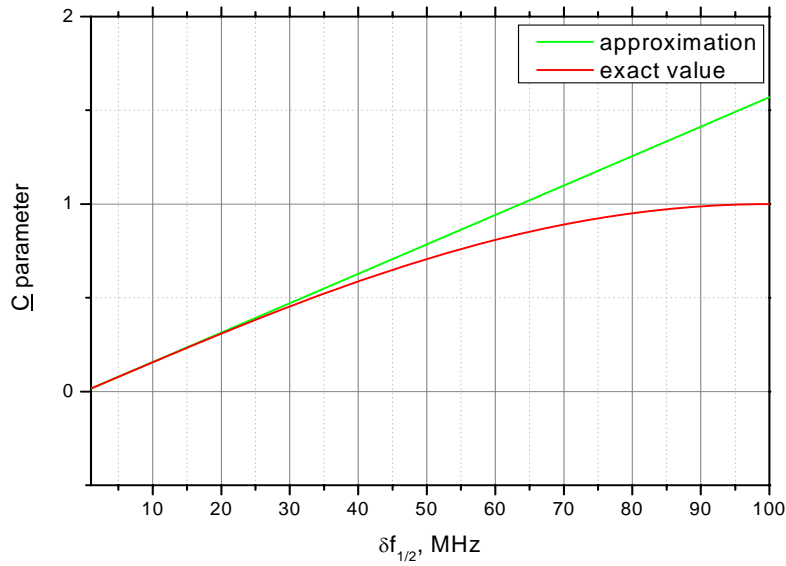


Fig.4.6 Exact dependence of the \bar{C} parameter (red) on the FWHM frequency width $\delta f_{1/2}$ of the FP resonator and the approximation of Eq.4.6 (green).

In both experiments we used the curve fitting procedure to evaluate the measured data. The typical outputs using this procedure are shown in the following figures:

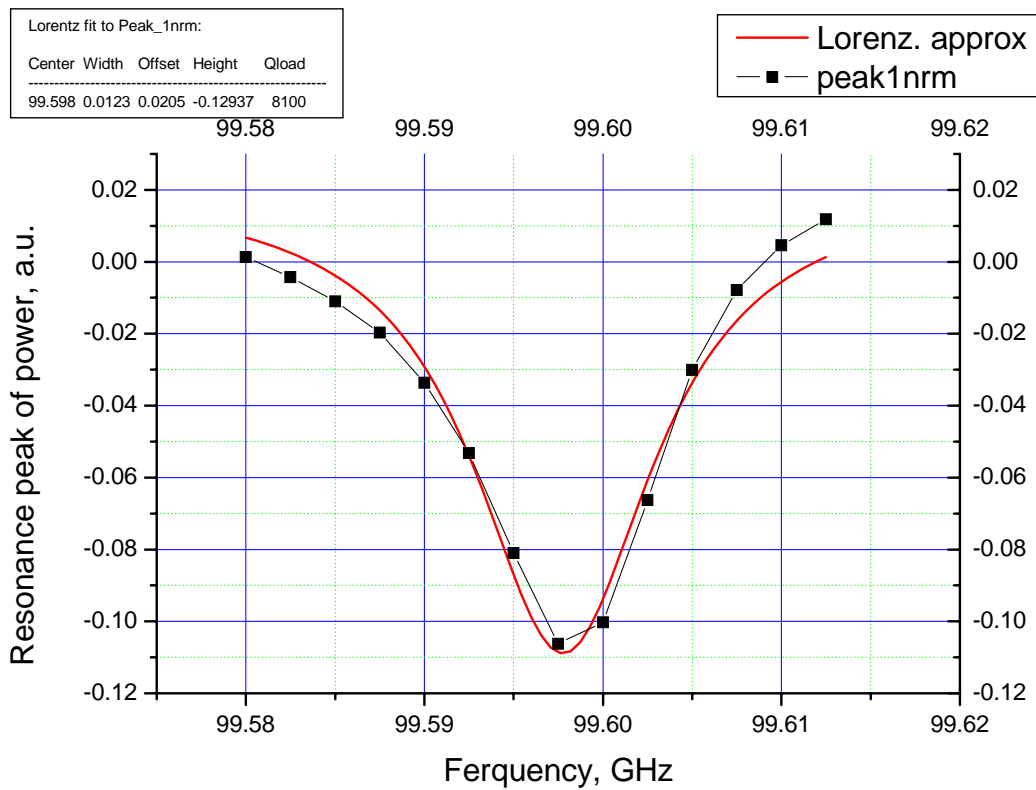


Fig. 4.7 An example of the Lorentz approximation curve-fitting procedure for particular resonance peak.

In Fig.4.8 the experimental results are indicated by the points for various angles of coupler grid as given in the legend in the lower left-hand corner. The solid curves were obtained by use of the curve-fitting computer procedure. An example of the results of the Lorentzian curve-fitting procedure for a 15 degrees grid angle is given in table 4.1.

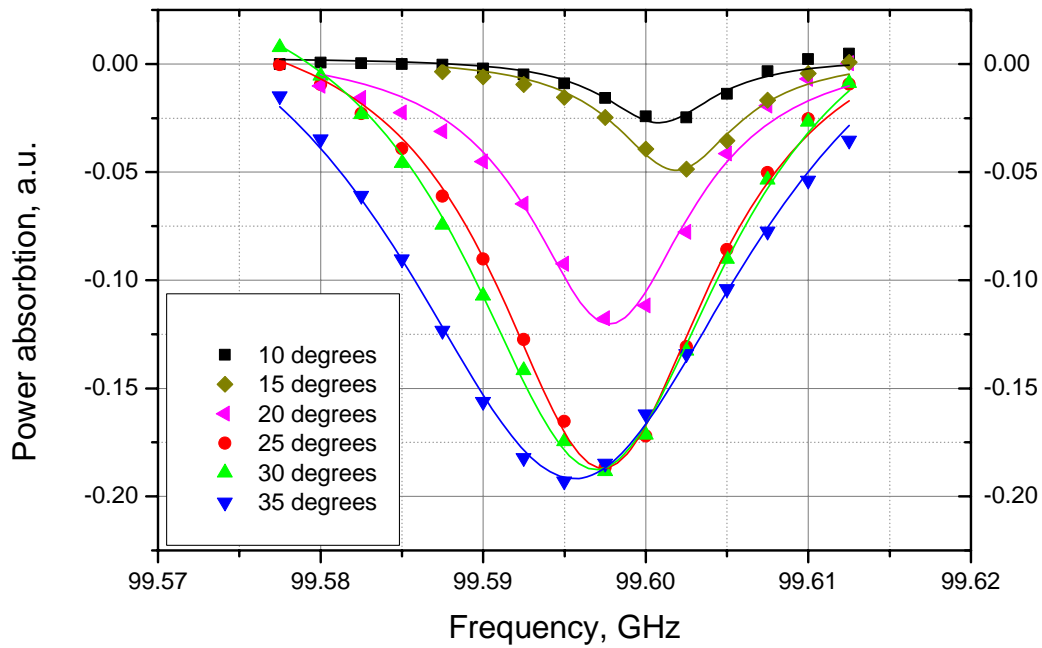


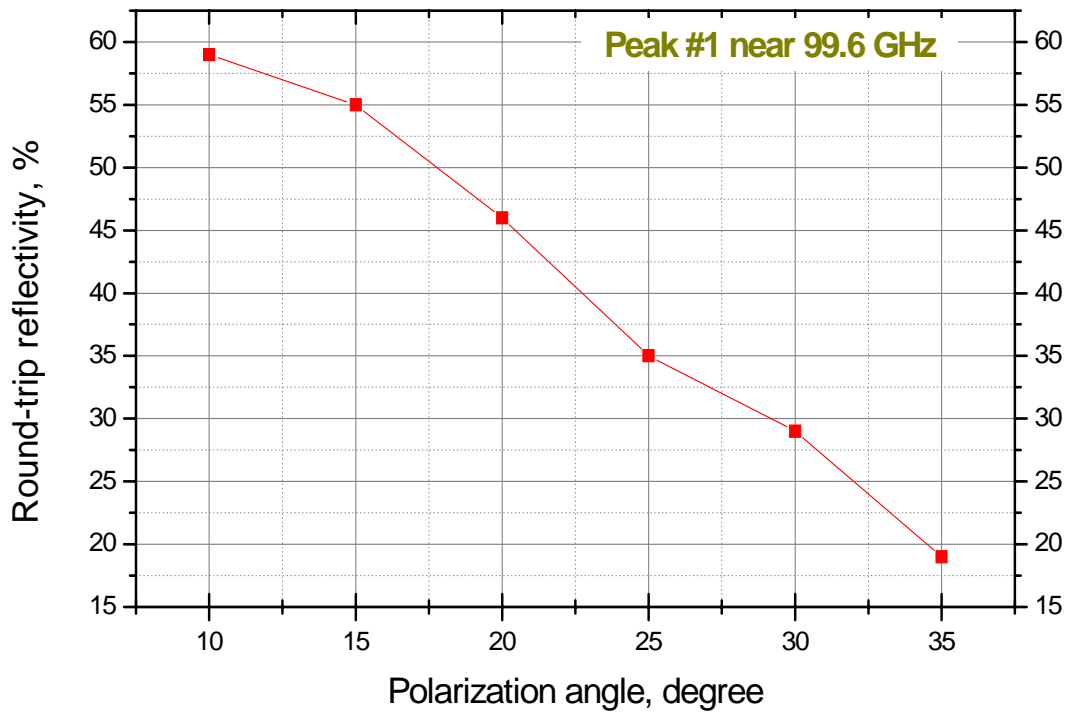
Fig. 4.8 Quality of Lorentzian fit approximation. The single measured resonance peak for the different coupling conditions (different coupler grid angles).

Lorentzian fit to 15 degree:				
Center, GHz	Width, GHz	Offset, a.u.	Height, a.u.	Q_{loaded}
99.602	0.0094	0.0038	-0.053	10600

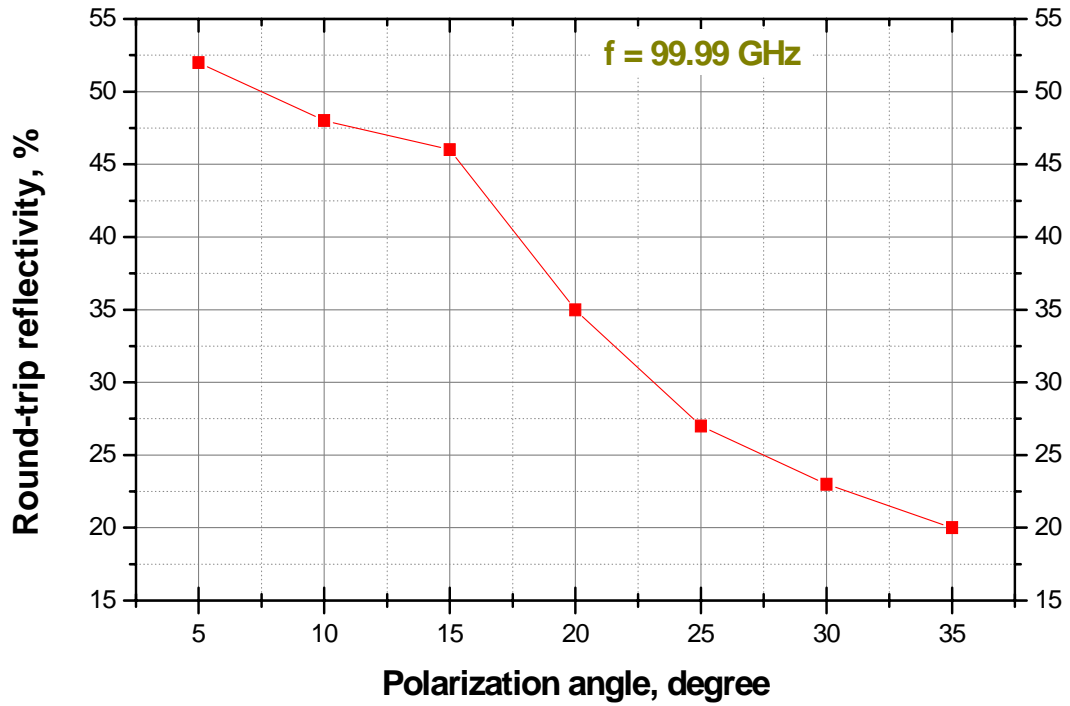
Tab. 4.1 An example of the Origin curve-fitting procedure output.

The loaded Q-factor was calculated for several resonant peaks near 100 GHz. The round trip reflectivity was calculated according to Eq.(4.8). Fig. 4.9

demonstrates that when the polarization grid angle is smaller, the transmission of the grids coupling mirror is decreased and, consequently, the loaded Q-factor (total round-trip reflectivity) tends to its limiting value – the unloaded Q factor Q_0 and the measured round-trip reflectivity R_{rt} ends to the internal reflectivity factor R_{int} (the round-trip reflectivity for a perfectly reflecting grids) :



(a)



(b)

Fig. 4.9 Total round-trip reflectivity of the resonator calculated for a typical resonant peak: (a) inside the FEL tank; (b) in the laboratory experiment.

References

- cc Yariv A., *Introduction to Optical Electronics*. Holt, Rinehart and Winston, New York, 1976.
1. Collin Robert E., *Foundations for microwave engineering*. 2nd ed. McGraw-Hill, 1992.
 2. Ulrich R., Bridge T.J. and Pollack M.A., *A variable Output Coupler for Far Infrared Lasers*. Proc. Symp. On Submillimeter Waves, Polytechnic Inst., Brooklin, 605-614, 1970.
 3. Saleh A.A.M., *An adjustable quasi-optical bandpass filter – part1: theory and design formulas*. IEEE Trans. MTT, vol. 22, no.7, pp.728-734, 1974.
 4. Cornbleet S., *Microwave optics*. Academic press, 1976.
 5. **Yulia&Yakover Internal report**
 6. Haus H., *Waves and Fields in Optoelectronics*. Prentice-Hall, 1984.
 7. Fox A.G. and Li T., *Resonant Modes in a Maser Interferometer*. The Bell System Technical Journal, March, 1961.
 8. Culshaw W., *Reflectors for a Microwave Fabry-Perot Interferometer*. IRE Trans. On Microwave and Theory Techniques, vol.MTT-7, pp.182-189; April, 1959.
 9. Culshaw W., *High Resolution Millimeter Wave Fabry-Perot Interferometer*. IRE Trans. On Microwave and Theory Techniques, vol.MTT-8, pp.182-189; March, 1960.
 10. Faingersh A., Gover A., Eliran A., Kapilevich B. *Concluding report: Measurements and calculation of round-trip reflectivity in the FEL waveguide resonator before*

- and after modification and estimate of threshold current improvement.* Internal report of FEL group, 13-Aug-08, Tel-Aviv University.
11. Yakover I., Pinhasi Y., Gover A. *Study of waveguide resonators for FEL operating at submillimeter wavelengths.* Nuclear Instr. And Methods in Physics Research, A 375, (1996), 260-263.
 12. Nakahara T., Kurauchi N., *Guided beam waves between parallel concave reflectors.* IEEE Transactions of Microwave Theory and Techniques, v.MTT-15, no2 (1967), p.66.
 13. Lurie Y., *Parallel Curved Plates (PCP) versus rectangular waveguide.* Internal report of FEL group, 14-March-02, Tel-Aviv University.
 14. Papas ...
 15. Kazantsev Yu.N., Sov. Radio Eng. Elec. Phys., 15 (1970), p.963
 16. Vaganov
 17. Anaton A., Markish O.,
 18. Ginzton E. L., *Microwave Measurements.* New York: McGraw-Hill, 1957, Chap. 9.
 19. Lebedev
 20. Altman
 21. A. Asija and A. Gundavajhala, "Quick measurement of unloaded Q using a network analyzer," *Rf Design*, pp. 48-52, October 1994.
 22. M. Sucher, and J. Fox (eds.), *Handbook of Microwave Measurements.* New York: Polytechnic Press, 1963, Chapter
 23. G. L. Matthaei, L. Young and E. M. T. Jones, *Microwave Filters, Impedance-Matching Networks, And Coupling Structures.* New York: McGraw-Hill, 1964, Chapter 11.
 24. D. Kajfez and E. J. Hwan, "Q-factor measurement with network analyzer," *IEEE Trans. Microwave Theory Tech.*, vol. MTT-32, pp. 666-670, July 1984.
 - 25.

Chapter 5

Conclusions

Estimation of FEL resonator losses using Matlab simulation predict about 50 % of internal resonator loss as described in Chapter 2. Since a parallel RLC resonant circuit model is applicable only for a single mode cavity, for the multimode FEL resonator it is essential to use a quasi-optical model of a FP interferometer. The results of the measured and calculated round trip reflectivity parameters of 3 longitudinal resonator modes near 100 GHz for the known coupling coefficient (grids mirror reflectivity R_1) are:

freq.,f0 GHz	(Δf)_{FWHM} MHz	Q_{loaded}	R_{rt} %	L_{tot} %	R₁ %	L_{internal} %
99.906	10.1	10194	54	46	98	45
100	10.0	10000	53	47	98	46
100.1	10.0	10010	53	47	98	46

Tab.5.1 Measured and calculated round trip reflectivity parameters.

The error in round-trip reflectivity calculations is about 5 % and consists mainly of errors in measurement of the FWHM, of the recorded Fabri-Perot resonator peaks and an error in the Lorentzian function curve-fitting procedure.

The obtained round-trip losses of the resonator are relatively high and correspond to operating the FEL near oscillator threshold. The losses are not

distributed uniformly over the resonator length. Their main contribution to the round-trip losses is in the bend region of the splitter.

As a consequence of this work, and the consistent results of measurement and calculation of the resonator parameters, the FEL group has concluded to modify the structure of the resonator in order to decrease the round-trip losses and assure attainment of the oscillation threshold condition. The modification consisted of insertion of a low-transmission grid mirror before the bend of the Talbot reflector, and so removes this lossy section from the resonator. This grid is shown in Fig.5.1 as a yellow block. A more detailed description of the resonator modification and of the grid characterization may be found in [11].

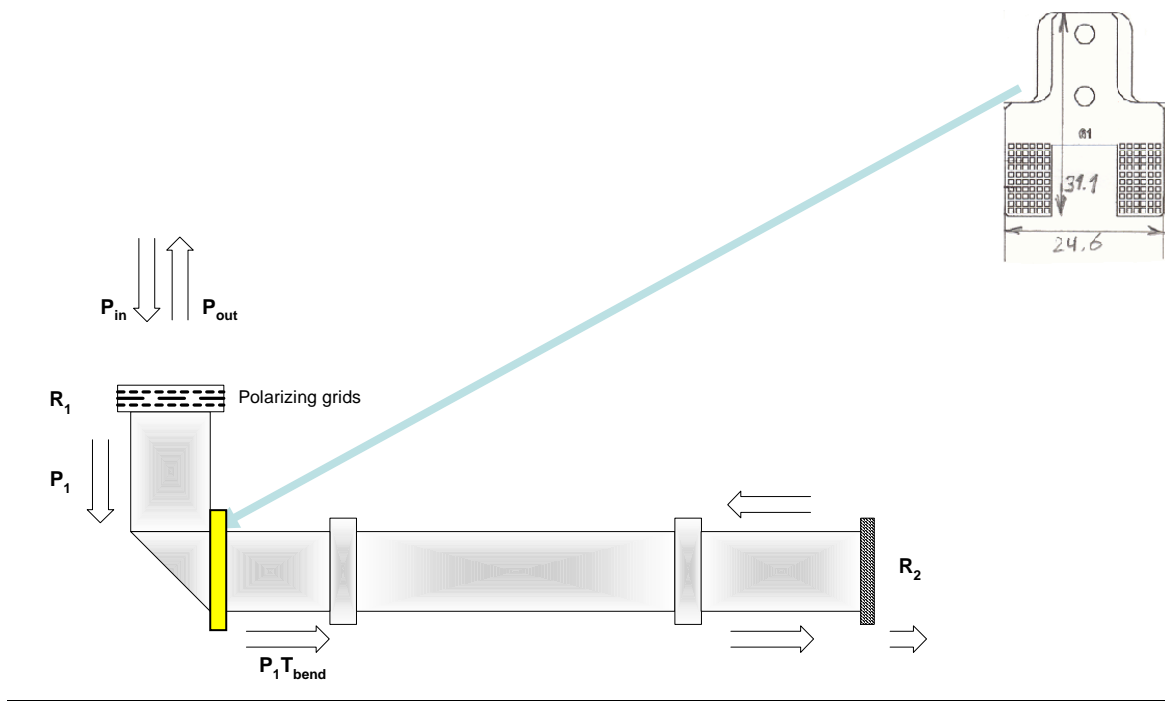


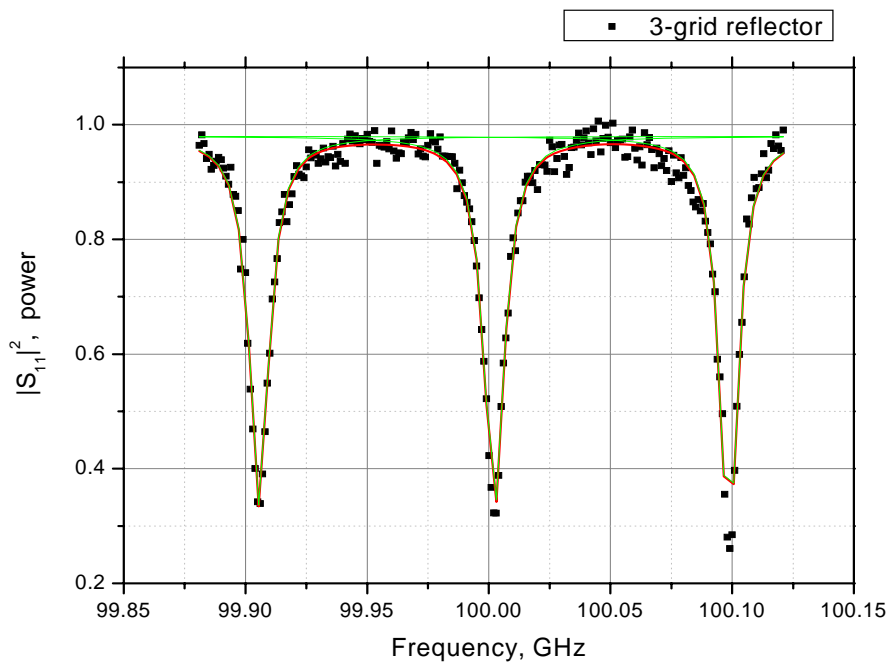
Fig. 5.1 Modified FEL resonator.

Using the above described procedure of Lorentzian multi-peak analysis, the following results were obtained for the modified resonator:

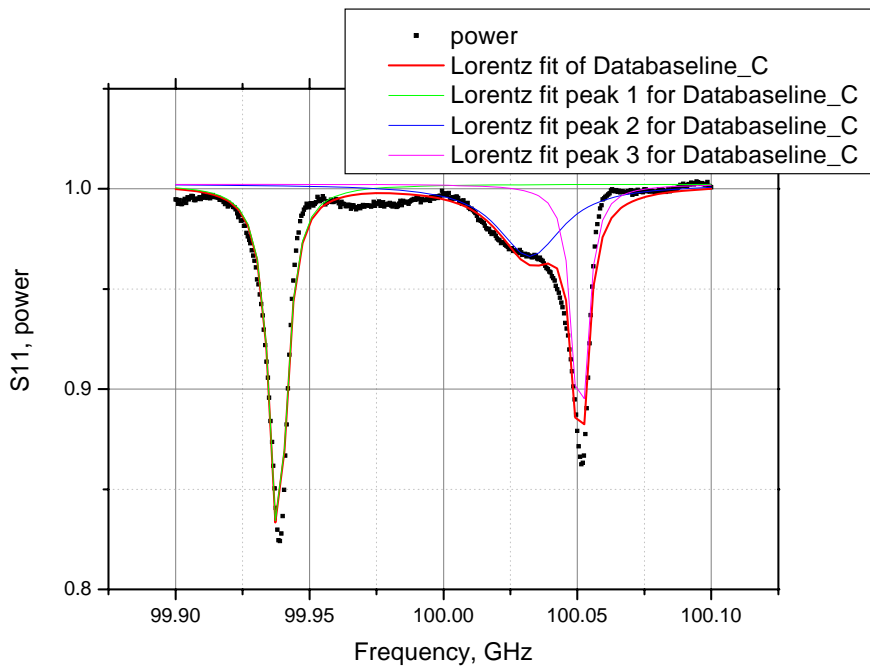
freq.,f0 GHz	(Δf) _{FWHM} MHz	Q _{loaded}	R _{rt} %	L _{tot} %	R ₁ %	L _{internal} %
99.938	7.9	12650	65	35	92	29
100.051	6.7	14933	69	31	92	25

Tab.5.2 Measured and calculated round trip reflectivity parameters after modification.

Curve-fitting using the multi-peak analysis procedure of the mentioned resonant peaks before and after resonator modification are shown in Fig.5.2:



(a)



(b)

Fig. 5.2 Multi-peak analysis of resonant peaks before (a) and after (b) resonator modification.

The oscillation threshold gain G_{th} relates to the round trip reflectivity R_{rt} by [11] :

$$G_{th} = \frac{1}{R_{rt}} \quad (5.1)$$

In the low-gain regime, according to FEL theory, the oscillation threshold current is related to R_{rt} by:

$$I_{th} \propto (G_{th} - 1) = \left(\frac{1}{R_{rt}} - 1 \right) \quad (5.2)$$

Thus the ratio of threshold currents before and after modification is:

$$\frac{I_{th1}}{I_{th2}} = \frac{\frac{1}{R_{rt1}} - 1}{\frac{1}{R_{rt2}} - 1} \approx 1.6 \quad (5.3)$$

for $R_{rt1} = 53\%$ (before) and $R_{rt2} = 65\%$ (after) values of the round-trip reflectivity.

The following table gives an estimate of the improvement in threshold gain and the corresponding reduction in the (unknown) threshold current in three possible examples of I_{th} :

	Before modification	After modification
Rrt	0.53	0.65
Gth	1.89	1.54
Gth-1	89 %	54 %
I_{th}, [A]	1.5	0.91
	2	1.21
	2.5	1.52

Tab.5.3 Threshold gain and the corresponding threshold current values.

Since the current available to the experimenters was below 2A, it seems likely that the modification of the resonator based on our measurements and calculation enabled the attainment of lasing in the Israel FEL [11].

References

1. Yariv A., *Introduction to Optical Electronics*. Holt, Rinehart and Winston, New York, 1976.
2. Collin Robert E., *Foundations for microwave engineering*. 2nd ed. McGraw-Hill, 1992.
3. Ulrich R., Bridge T.J. and Pollack M.A., *A variable Output Coupler for Far Infrared Lasers*. Proc. Symp. On Submillimeter Waves, Polytechnic Inst., Brooklyn, 605-614, 1970.
4. Saleh A.A.M., *An adjustable quasi-optical bandpass filter – part1: theory and design formulas*. IEEE Trans. MTT, vol. 22, no.7, pp.728-734, 1974.
5. Cornbleet S., *Microwave optics*. Academic press, 1976.
6. **Yulia&Yakover** *Internal report*
7. Haus H., *Waves and Fields in Optoelectronics*. Prentice-Hall, 1984.
8. Fox A.G. and Li T., *Resonant Modes in a Maser Interferometer*. The Bell System Technical Journal, March, 1961.
9. Culshaw W., *Reflectors for a Microwave Fabry-Perot Interferometer*. IRE Trans. On Microwave and Theory Techniques, vol.MTT-7, pp.182-189; April, 1959.
10. Culshaw W., *High Resolution Millimeter Wave Fabry-Perot Interferometer*. IRE Trans. On Microwave and Theory Techniques, vol.MTT-8, pp.182-189; March, 1960.
11. Faingersh A., Gover A., Eliran A., Kapilevich B. *Concluding report: Measurements and calculation of round-trip reflectivity in the FEL waveguide resonator before and after modification and estimate of threshold current improvement*. Internal report of FEL group, 13-Aug-08, Tel-Aviv University.
12. Yakover I., Pinhasi Y., Gover A. *Study of waveguide resonators for FEL operating at submillimeter wavelengths*. Nuclear Instr. And Methods in Physics Research, A 375, (1996), 260-263.

13. Nakahara T., Kurauchi N., *Guided beam waves between parallel concave reflectors*. IEEE Transactions of Microwave Theory and Techniques, v.MTT-15, no2 (1967), p.66.
14. Lurie Y., *Parallel Curved Plates (PCP) versus rectangular waveguide*. Internal report of FEL group, 14-March-02, Tel-Aviv University.
15. Papas ...
16. Kazantsev Yu.N., *Sov. Radio Eng. Elec. Phys.*, 15 (1970), p.963
17. Vaganov
18. Anaton A., Markish O.,
19. Ginzton E. L., *Microwave Measurements*. New York: McGraw-Hill, 1957, Chap. 9.
20. Lebedev
21. Altman
22. A. Asija and A. Gundavajhala, *Quick measurement of unloaded Q using a network analyzer*, *Rf Design*, pp. 48-52, October 1994.
23. M. Sucher, and J. Fox (eds.), *Handbook of Microwave Measurements*. New York: Polytechnic Press, 1963, Chapter
24. G. L. Matthaei, L. Young and E. M. T. Jones, *Microwave Filters, Impedance-Matching Networks, And Coupling Structures*. New York: McGraw-Hill, 1964, Chapter 11.
25. D. Kajfez and E. J. Hwan, Q-factor measurement with network analyzer, *IEEE Trans. Microwave Theory Tech.*, vol. MTT-32, pp. 666-670, July 1984.
26. Abramovich A, Pinhasi Y, Yakover YM, Gover A, Sokolowski JS, Canter M. *Study of radiation build up and mode evolution in the Israeli electrostatic accelerator free-electron laser oscillator* [Journal Paper], IEEE Transactions on Plasma Science, vol.27, no.2, April 1999, pp.563-7. Publisher: IEEE, USA.

27. Sokolowski JS, Abramovich A, Arensburg A, Chairman D, Draznin M, Eichenbaum AL, Gover A, Kleinman H, Pinhasi Y, Yakover YM, Rosenberg A, Shiloh J, Cohen N, Levin LA, Shahal O. *First lasing of the Israeli tandem electrostatic accelerator free electron laser* [Conference Paper], Proceedings of the 1997 Particle Accelerator Conference (Cat. No.97CH36167). IEEE. Part vol.1, 1998, pp.906-8 vol.1. Piscataway, NJ, USA.
28. Talbot H.F. *Facts relating to optical science*, no.4, Phil. Mag., 9, 1836, pp. 401-407.
29. Berry M.V., Klein S. *Integer, Fractional and Fractal Talbot effects*, J. Modern Optics, 43, 1996, pp.2139-2164.
30. Berry M.V., Bodenschatz E. *Caustic, multiply-reconstructed by Talbot effects*, J. Modern Optics, 46, 1999, pp.349-365.

תקציר

בעבודת תיזה זו פיתחנו וחקרנו את המאפיינים של מהוד ייחודי לתחום תדרים של 100GHz המיועד לשמש בהתקן לייזר האלקטרוניים החופשיים (Free Electron Laser - FEL) הישראלי. באופן כללי נדרש שהתקן מהוד הלייזר יהיה באיכות גבוהה (בעל הפסדים פנימיים נמוכים), כך שיושג סף הלזירה הדרוש לפעולה יעילה של התקן הלייזר. בכדי לאפשר התקדמות אלומת אלקטרוניים לאורך ציר המהוד (כולל כניסה ויציאה דרך חורים במהוד) ועל מנת להבטיח בו בזמן קבלת גורם איכות (Q) גבוה בתדרי ה-W-band (סביב 100GHz) המהוד כולל מספר מקטעים ייחודיים של מוליכי גלים. אפיון טיב המהוד (או ההפסדים למעבר שלם) חשובים לצורך השגת פעולת ה-FEL.

במסגרת עבודת המחקר מדדנו את מאפייני המהוד, והשווינו את תוצאות המדידות למודל אנליטי ולחישוב נומרי. פילוג השדות בתוך המרכיב העיקרי של המהוד, שבנוי משני לוחות עקמומיים מקבילים (Curved Parallel Plates - CPP) ובתוך מחזיר טלבוט (Talbot reflector), המאפשר להפריד בין אלומת האלקטרוניים וקרינת הלייזר, נותחו אנליטית.

תאום אופנים בין מוליכי גלים בעלי שטח חתך שונה, הפסדים אוהמיים והפסדי דיפרקציה נחקר, באמצעות תוכנית סימולציה ב-"Matlab". כמו-כן בעבודה זו מתואר מודל אופטי של מהוד FEL כאינטרפרומטר פברי-פרו אסימטרי עם הפסדים (כלל אפשרות להפסדים גדולים). טכניקת המדידה, שפותחה ויושמה לצורך מדידת מקדם ההחזרה במעבר שלם בתוך מהוד ה-FEL, התבססה על מדידה ישירה של רוחב פסי התהודה של ספקטרום ההחזרה של המהוד. התקן צימוד תלת-רשתי שתוכנן לשמש במהוד פותח, יוצר, נחקר ודווח [6].

עיקרי הישגי המחקר שמוצג להלן: הפסדי המעבר במסלול שלם בתוך המהוד (כולל התקני הצימוד) נמדדו, חושבו ונמצאו כ- 50%. בעקבות הבחנה זאת נעשה שינוי מבנה המהוד, לצורך הקטנת ההפסדים הגבוהים. השינוי הביא להורדת ההפסדים הפנימיים לכדי 35% ואפשר השגת לזירה ראשונה של ה-FEL הישראלי (בתצורת מהוד המאפשרת צימוד קרינה חיצוני) בספטמבר 2003 [11].